Optics at interfaces: ultra-thin color coatings, perfect absorbers, and metasurfaces

Optics at interfaces: ultra-thin color coatings, perfect absorbers, and metasurfaces

A dissertation presented
by
Mikhail A. Kats
to
The School of Engineering and Applied Sciences

in partial fulfillment of the requirements
for the degree of
Doctor of Philosophy
in the subject of
Applied Physics

Harvard University
Cambridge, Massachusetts

October 2013

Dissertation Advisor: Federico Capasso Mikhail A. Kats

Optics at interfaces: ultra-thin color coatings, perfect absorbers, and metasurfaces

Abstract

The vast majority of optical components and devices in use today can be grouped under the umbrella of "bulk optics"; i.e. they generally have a non-negligible thickness compared to the wavelength of light. This is true of components from lenses to wave plates to Fabry-Perot etalons, all of which need sufficient thickness such that light waves can accumulate an appropriate amount of phase upon propagation through the structure. In this thesis, we develop and explore a variety of optical components that are thin compared to the wavelength of light and lie at the interface between two materials (i.e. a substrate and air). We explore approaches to filter, absorb, redirect, and re-shape light with flat, ultra-thin structures which are easy to fabricate with modern micro- and nanofabrication techniques.

In the first section of this entitled *Lossy optical coatings and perfect absorbers*, we show that thin film interference effects can be observed in appropriately-designed films even if the films are significantly thinner than a quarter of the wavelength of light in the material. We use these films to demonstrate color coatings and multi-color images in

the visible, tunable perfect absorbers and anomalous thermal emitters in the infrared, and propose a variety of applications ranging from ultra-thin photodetectors and solar cells to modulators and microbolometers.

In the second section entitled *Controlling light propagation with optical antenna metasurfaces*, we develop a class of metasurfaces comprising resonant plasmonic antennas, which can imprint nearly-arbitrary distributions of amplitude, phase, and polarization on a light beam. These metasurfaces, which can are thinner than 1% of the wavelength of light, enable the design flat optical components including lenses, axicons, spiral phase plates, blazed gratings, and wave plates, which we demonstrate in the near- and mid-infrared spectral ranges.

Contents

List of Figures

Acknowledgements

I begin by acknowledging Federico Capasso. Frankly, I could not have asked for a better PhD advisor. In addition to the qualities that one would expect in a distinguished senior scientist, he has several that initially surprised me: unbridled, nearly-limitless enthusiasm for all areas of science and technology, a drive to work harder than even first year graduate students and postdocs (and I used to spend nights sleeping under my desk, so I know what I'm talking about), and a lack of fear of being wrong. This last one I value in particular, because if your advisor is unafraid to throw out half-baked ideas and sometimes be wrong in the spirit of learning and discovery and invention, then you can't help but do so yourself; in fact I think this trait is the essence of science.

I would like to acknowledge Marko Loncar and Joanna Aizenberg, who round out my thesis committee and were also on my qualifying committee together with Peter Pershan. Though we never had a well-defined scientific collaboration, Marko always made me feel that I could always go to him or anyone in his group for insight, advice, or guidance. Joanna has always opened her laboratory to us whenever we needed, and was a wonderful collaborator in several occasions, including my first collaboration at Harvard.

Next I would like to thank all friends and colleagues from the Capasso group. First Romain Blanchard: we came into the group together as first years during a period of a lot of turnover, with no students the year before us and no students the year after. In many ways it was just the two of us trying to understand a new field, exploring potential research projects, learning how to navigate the resources and opportunities at Harvard, and trying to establish ourselves in the group. I think at the end of the day it worked out pretty well! Crime is tough without a partner, and I was fortunate to have a good one.

Next I need to thank Nanfang Yu for always being available whenever I had any questions, and also for giving me the opportunity to work with him on projects even before I demonstrated any ability to be effective. Nanfang's work ethic was contagious, and his uncommon physical insight helped me develop my own intuition. Nanfang's quiet intuition was great, but all things must have balance. For many years, that balance was provided by Patrice Genevet with whom we went round after round on scientific discussions, debating topics from details of plasmonics to the fundamental nature of quantum mechanics. These debates and discussions are very important: without them, we often take what is written in the literature for granted, and cease to examine the underlying assumptions and assertions. I would like to thank Francesco Aieta, who has always been a great collaborator on several projects, always willing to put in long hours to bring an idea to fruition. In addition, I thank him for always being down for a game of basketball, even though it is not his sport. I would also like to recognize Zeno Gaburro, whose keen insights spawned a series of interesting and productive research projects in the group.

Next I would like to acknowledge Yu Yao and Toby Mansuripur, two scientists who possess great physical insight and are always willing to share it. Both of them also have the rare drive to always investigate scientific and engineering questions in great depth and detail, even when most others would have given up or taken the easy way out. Thank you for always being generous with your time and energy: without you two my graduate experience would be less interesting and less fruitful.

Many thanks go to David Woolf and Jonathan Fan who have both enriched my time here. Both of you worked on relatively non-overlapping projects with my own, but you gave me a chance to learn and occasionally participate in your research, which I appreciate greatly. Let's play more poker in the future.

I also want to thank the many young researchers with whom I have had the pleasure of working, especially Herman Gudjonson, Deepika Sharma, Bernhard Bohn, and Shuyan Zhang. Thank you for giving me the opportunity to be your mentor, it has been fun, rewarding, and productive. Shuyan and Berhnard: it has been great (and totally unsurprising!) to see you guys quickly become independent scientists this past year.

Thank you to Christian Pflugl and Laurent Diehl for taking care of the group in the first few years after I started, and to Fatih Degirmenci, Pietro Malara, Patrick Rauter, Alex Woolf, Steve Byrnes, Sun Li, Mael de Naurois, Lulu Liu, Jiao Lin, Markus Geiser, Meinrad Sidler, Jenny Smythe, Alejandro Rodriguez, Antoine Moulet, Cecile Grezes, Jean-Philippe Tetienne, Guillaume Aoust, and the rest of Capasso group past and present.

Next I would like to acknowledge some collaborators. First Darren Lipomi, Sung Kang, and Ramses Martinez; work with you guys was my first meaningful collaboration, and the great experience made me comfortable to seek out collaborations in the future. Thank you also to Mathias Kolle, who was always generous with his time and his instruments. Next I would like to acknowledge Shriram Ramanathan and his students and postdocs, including You Zhou, Zheng Yang, Changhyun Ko, and Yanjie Cui; our collaboration on vanadium oxide started out as a curiosity, and has spawned a nice new area of research. Anther thank you goes out to Mumtaz Qazilbash and Dmitri Basov for being generous with their unpublished data, which led to improved understanding of my experiments. Thanks to Martin Schnell and Rainer Hillenbrand for being both dilligent and patient with our ongoing collaboration. I also want to acknowledge many helpful discussions at various points throughout the past five years with Rashid Zia, Alexey Belyanin, Ken Crozier, Svetlana Boriskina, and Carsten Ronning.

I would like to acknowledge the staff of the Center of Nanoscale Systems (CNS) at Harvard, where most of the fabrication and some of the measurements took place. A special thanks to Jiangdong Deng, Ed Macomber, Yuan Lu, Ling Xie, Noah Clay, Philippe de Rouffignac, Steve Paolini, and Steve Hickman. Also a big thank you to the assistants and administrators who made sure things always got done: Chris Mullaney, Xio Forbez, and Kathleen Kelley. Here I also want to thank the agencies and groups that funded my PhD work: the National Science Foundation (NSF), the Harvard Graduate Society, the School of Engineering and Applied Sciences (SEAS), the Defense Advanced Research Projects Agency (DARPA), the Air Force Office of Scientific Research (AFOSR), and the Nanoscale Science and Engineering Center (NSEC).

I would like to thank Tarek Anous for years (8 and counting?) of friendship and science discussions; your work ethic is inspiring. I would like to also thank many other friends at Harvard for the dinners, conversations, table tennis and basketball games, the help and advice: Birgit Hausmann, Raji Shankar, Yinan Zhang, Wallace Hui, Qimin Quan, Ian Frank, Ian Burgess, Anna Shneidman, Jon Lee, John Joo, Mike Burek, Haig Aktikian, Yuting Lin, Jing Yang, Sally Kang, Jonah Waissman, Greg Kestin, Nan Niu, Shanying Cui, Antony Orth, Hyunsung Park, Igor Lovchinsky, Megan O'Grady, Renee Sher, Eric Diebold, Roger Diebold, Tsung-Li Liu, Wenqi Zhu, Nick Stone, and Sarah Rugheimer. A special thank you goes out to my non-scientist friends for keeping me (barely) grounded, especially Edgar Barroso, Bethany Kibler, and Julia Marinescu.

Now I need to acknowledge my colleagues and mentors at Cornell, in the group of Farhan Rana, where I first got an opportunity to do optics research. Thank you to Farhan, to my mentor Faisal Ahmad, and to Paul George and Jahan Dawlaty for their, patience, trust, and generosity. I also want to acknowledge a few friends from before grad school, who despite not being scientists themselves have consistently followed up on my research:

thank you to Kirill Nadtochiy, Jon Ying, and Julius Erukhimov I hope your interest in science never fades.

Short story time: one time when I was borrowing some optical fiber I met Jen "JC" Choy, which turned out to be a pretty good day for me. I think more than anyone I have met, Jen is the model of someone who makes everyone around her better, both in the research and outside of it. I thank JC for the joy she has brought me, for her kindness and generocity, and for her unconditional support.

Finally and most importantly thank you to my parents and grandparents, for planting the seeds early, and for their care and support ever since. Thank you for teaching me math early on (I suspect it helped), and getting me books (little known fact: as a child, I used to read encyclopedias for fun. go figure.), for moving to a place where I would be able to receive a good education, and for putting me through college where I had my first opportunity to do research. In recent years, I especially thank you for remaining interested and involved in my work, even it has become more esoteric.

Chapter 1

Introduction

1.1 Overview

The field of optics has a long history, starting as early as about 1900 BCE with the ancient Egyptians, with discoveries by the ancient Greeks 400-300 BCE, the Arabs around 1000 CE, and eventually the western world beginning with the 1200s CE [1]. In rough order of discovery and development, optical devices that emerged from these times include mirrors, lenses (sometimes called burning glasses because they could be used to focus sunlight and start a fire), and curved focusing mirrors, which eventually led to the design and implementation of spectacles for vision correction, and telescopes and microscopes for vision enhancement. These inventions paralleled (and sometimes preceded) the conceptual understanding of optics, which included the laws of refraction and reflection and somewhat later the concepts of polarization and interference. As the classical optical components were being further developed and improved (e.g. the correction of chromatic aberrations in lenses), the wave theory of light became developed, and when it was unified with electromagnetism it became the field of physical optics.

Physical (or electromagnetic wave) optics has been tremendously successful over the last decade and a half. It is able to describe the vast majority of observable light phenomena including refraction, diffraction, birefringence, and thin film interference, and strongly connects optics in the visible with equivalent phenomena at other frequency ranges from gamma rays and X-rays to microwaves and radio waves. In this thesis we will rely on physical optics exclusively, eschewing any quantum mechanical treatment of light.

Other than mirrors, the vast majority of simple optical elements fall under the umbrella of "bulk optics"; i.e. they generally have a non-zero thickness which is larger than (or at least on the order of) the wavelength of light. A canonical example of a bulk optical element is a convex glass lens (Fig. 1.1), which is able to transform a plane wave into a convergent spherical wavefront because light propagating through different lengths of glass acquires a different optical phase shift (more phase accumulation in the middle of the lens). Another standard example of a bulk optical element is a waveplate comprising a slab of birefringent material which manipulates the polarization state of light, or a prism which is able to separate different wavelengths of light via refraction through a dispersive material. A Fabry-Perot etalon, used to filter or measure the wavelength of light, is another example, as are layered high-reflective (HR) and anti-reflective (AR) optical coatings which also rely on Fabry-Perot-type interference. All of these devices rely on phase accumulation through a material, and thus must not be thin compared to the wavelength of light. Diffractive optical elements such as Fresnel zone plates which consist of alternating opaque and transparent rings may be structurally thin compared to the wavelength of light, but their function relies on light interference after the element, and this volume of space between the element and a region considered to be the far field zone is still significantly greater than the wavelength of light.

In this thesis we will explore the *flat optics*, or *optics at interfaces* which lie outside

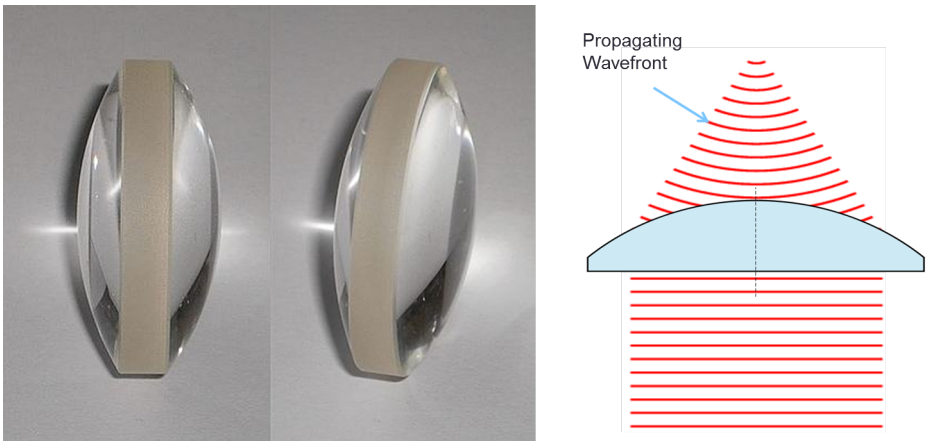

FIGURE 1.1: Left: a conventional convex glass lens [from Wikimedia Commons]. Right: diagram showing that a plane wave incident on a convex lens becomes a convergent spherical wave.

of the category of bulk optics. We will explore approaches to filter, absorb, redirect, and re-shape light with flat structures that are significantly thinner than the wavelength of light, and which can be easily fabricated with modern micro- and nanofabrication techniques.

In the first section of this thesis entitled *Lossy optical coatings and perfect absorbers* we focus on thin film interference, which is normally a phenomenon that is observed in single layers or stacks of transparent thin films with thicknesses of at least a quarter of the wavelength of light in the material. Highly absorbing dielectrics are typically not used because usually light propagation through such media minimizes interference effects.

We show that under appropriate conditions strong interference can instead persist in ultrathin, highly absorbing films, and demonstrate a new type of optical coating comprising such a film on a reflective substrate, which selectively absorbs various frequency ranges of the incident light. These coatings rely on nontrivial phase shifts at interfaces between highly-absorbing materials, and as a result have a low sensitivity to the angle of incidence and can be as thin as a twentieth of the wavelength of light in the thin

film. We utilize different material systems to observe this effect in the visible and mid-infrared spectral ranges. In the visible, we demonstrate absorbing color coatings with potential applications to labeling, photodetection, and solar energy harvesting, while in the infrared we demonstrate absorbers that are widely tunable with temperature and thermal emitters which display anomalous emittance behavior.

In the second section entitled *Controlling light propagation with optical antenna metasurfaces*, we describe a dramatically different approach to creating optical components such as lenses, wave plates, etc. compared to the aforementioned bulk optics approach. Instead of relying on gradual phase accumulation to achieve desired wavefront molding, we design resonant metallic structures which introduce phase, amplitude, and polarization changes into a light field over a scale much smaller than the wavelength of light. Using this approach, we demonstrate a wide variety of flat optical components that are only 40-60 nanometers thick, including lenses, axicons, blazed gratings, spiral phase plates, and wave plates in the near-infrared and mid-infrared spectral ranges. Furthermore, we demonstrate that light at interfaces decorated with these optical antenna metasurfaces obeys a generalized set of reflection and refraction laws, which are derived and experimentally verified.

1.2 Previously published work

Much of the material in this thesis has been published in peer-reviewed journals with a number of co-authors. In particular:

Chapter 2: *Lossy optical coatings and perfect absorbers* contains material published as:

M. A. Kats, R. Blanchard, P. Genevet and F. Capasso, "Nanometre optical coatings based on strong interference effects in highly absorbing media", **Nature Materials** 12, 20 (2013); published online in 2012.

M. A. Kats, D. Sharma, J. Lin, P. Genevet, R. Blanchard, Z. Yang, M. M. Qazilbash, D. Basov, S. Ramanathan, and F. Capasso, "Ultra-thin perfect absorber using a tunable phase change material", **Applied Physics Letters** 101, 221101 (2012).

M. A. Kats, S. Byrnes, R. Blanchard, M. Kolle, P. Genevet, J. Aizenberg, and F. Capasso, "Enhancement of the color contrast in ultra-thin highly-absorbing optical coatings", **Applied Physics Letters** 103, 101104 (2013)

M. A. Kats, R. Blanchard, S. Zhang, P. Genevet, C. Ko, S. Ramanathan, and F. Capasso, "Vanadium dioxide as a natural disordered metamaterial: perfect thermal emission and large broadband negative differential thermal emittance", in press in **Physical Review X**, arXiv:1305.0033

M. A. Kats, R. Blanchard, S. Ramanathan, and F. Capasso, "Thin-Film Interference in Lossy, Ultra-Thin Layers", in press in **Optics and Photonics News**

Chapter 3: *Controlling light propagation with optical antenna metasurfaces* contains material published as

N. Yu, P. Genevet, M. A. Kats, F. Aieta, Jean-Philippe Tetienne, F. Capasso, Z. Gaburro, "Light propagation with phase discontinuities: Generalized laws of reflection and refraction", **Science** 334, 333 (2011)

M. A. Kats, N. Yu, P. Genevet, Z. Gaburro, F. Capasso, "Effect of radiation damping on the spectral response of plasmonic components", **Optics Express** 19, 21749 (2011)

P. Genevet, N. Yu, F. Aieta, J. Lin, M. A. Kats, R. Blanchard, M. O. Scully, Z. Gaburro, F. Capasso, "Ultra-thin plasmonic optical vortex plate based on phase discontinuities", **Applied Physics Letters** 100, 13101 (2012)

F. Aieta, P. Genevet, N. Yu, M. A. Kats, Z. Gaburro, F. Capasso, "Out-of-plane reflection and refraction of light by anisotropic optical antenna metasurfaces with phase discontinuities", **Nano Letters** 12, 1702 (2012)

R. Blanchard, G. Aoust, P. Genevet, N. Yu, M. A. Kats, Z. Gaburro, F. Capasso, "Modeling nanoscale V-shaped antennas for the design of optical phased arrays", **Physical Review B** 85, 155457 (2012)

M. A. Kats, P. Genevet, G. Aoust, N. Yu, R. Blanchard, F. Aieta, Z. Gaburro, and F. Capasso, "Giant birefringence in optical antenna arrays with widely tailorable optical anisotropy", **Proceedings of the National Academy of Sciences** 109, 12364 (2012)

F. Aieta, P. Genevet, M. A. Kats, N. Yu, R. Blanchard, Z. Gaburro, F. Capasso, "Aberration-free ultrathin flat lenses and axicons at telecom wavelengths based on plasmonic metasurfaces", **Nano Letters** 12, 4932 (2012)

N. Yu, F. Aieta, P. Genevet, M. A. Kats, Z. Gaburro, F. Capasso, "A broadband, background-free quarter-wave plate based on plasmonic metasurfaces", **Nano Letters** 12, 6328 (2012).

M. A. Kats, R. Blanchard, P. Genevet, J. Lin, D. Sharma, Z. Yang, M. M. Qazilbash, D. Basov, S. Ramanathan, and F. Capasso, "Thermal tuning of mid-infrared plasmonic antenna arrays using a phase change material", **Optics Letters** 38, 368 (2013)

N. Yu, M. A. Kats, P. Genevet, F. Aieta, R. Blanchard, G. Aoust, Z. Gaburro, and F. Capasso, "Controlling light propagation with interfacial phase discontinuities", in **Active Plasmonics and Tuneable Metamaterials**, edited by A. Zayats and S. Maier, Wiley 2013

N. Yu, P. Genevet, F. Aieta, M. A. Kats, R. Blanchard, G. Aoust, J.-P. Tetienne, Z. Gaburro, and F. Capasso, "Flat optics: controlling wavefronts with optical antenna metasurfaces", **IEEE Selected Topics in Quantum Electronics** (2013)

Y. Yao, M. A. Kats, P. Genevet, N. Yu, Y. Song, J. Kong, and F. Capasso, "Broad electrical tuning of graphene-loaded plasmonic antennas", **Nano Letters** 13, 1257 (2013)

Chapter 2

Lossy optical coatings and perfect absorbers

2.1 Introduction: thin film interference and basic optical coatings

Thin film interference is a ubiquitous and well-understood optical phenomenon responsible for the colorful, iridescent reflections that we observe from oil films on water (Fig. 2.1), soap bubbles (Fig. 2.2), and peacock feathers. This effect occurs in structures which are composed of one or more transparent thin films, whose typical thickness is similar to the wavelength of light [1][2].

Light incident on a single transparent thin film will both reflect and refract at the top interface. The light that is transmitted into the film propagates until the bottom interface, where a portion is reflected and a portion is transmitted. This process repeats

FIGURE 2.1: Photograph of an diesel film of varying thickness on water demonstrating thin film interference. From ref. [3]

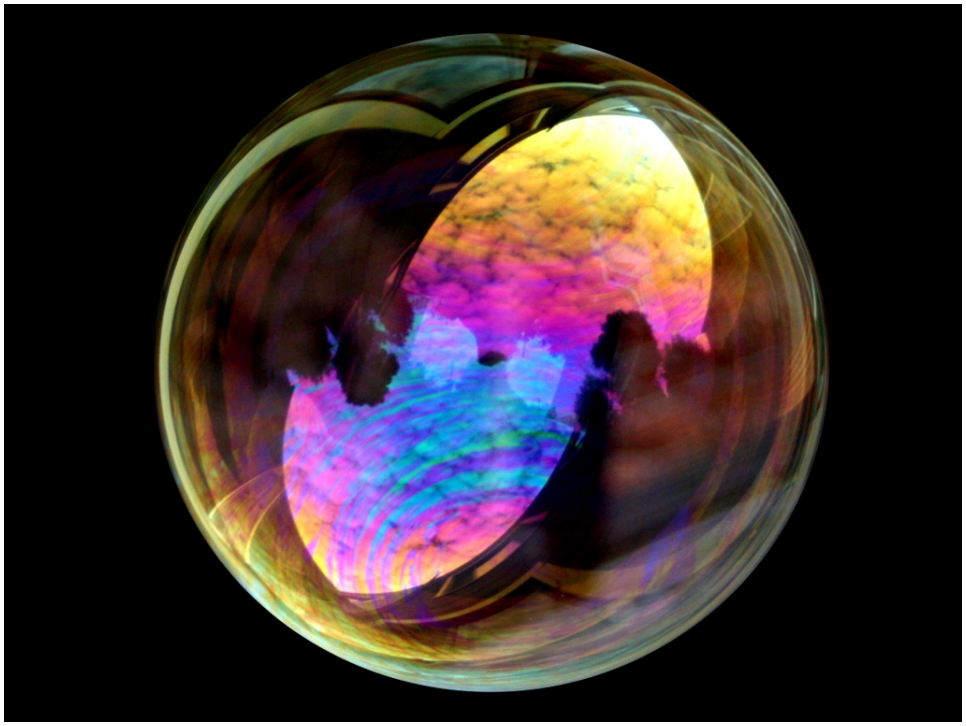

FIGURE 2.2: Photograph of a soap bubble colored by thin film interference effects and reflecting a portion of the sky. From ref. [4]

multiple times light bounces back and forth between the two interfaces, with some of the light leaking out at every bounce.

Because of the wave nature of light, we can imagine each portion of light as a partial wave, each with its own wavelength, amplitude, and phase. The way these partial waves interfere constructively, destructively, or neither ultimately determines which wavelengths of light are transmitted and which are reflected. The amount of optical phase that a partial wave accumulates as it makes a trip through the film depends on the so-called optical thickness, which is a function of the layer thickness, the incidence angle, and the refractive index. As a result, the destructive and constructive interference conditions and hence the colors we see depend on the refractive indices of the film and the surrounding regions, the film thickness, and the viewing angle.

Thin film interference is prominently featured in all areas of optical science and engineering. For example in the early 1900s Jean-Baptiste Perrin, a French Nobel-prize winning physicist, carefully observed interference fringes from soap films, deduced their thickness, and found that this thickness varied by increments of 4.5 nanometers. Thus Perrin calculated the length of the soap molecules along their longest axis and directly demonstrated the discontinuous (molecular) structure of matter [5].

Optical interference coatings comprising multiple layers of transparent materials are cornerstone of modern optical technology [2]. These coatings utilize the principle of thin film interference to enable applications such as anti-reflection (AR) and high-reflection (HR), the former being especially ubiquitous in imaging equipment such as microscope objectives, telephoto lenses, and prescription glasses. Conventional coatings comprise some combination of thin metallic films serving as partial and full reflectors, and wavelength-scale thick dielectric films which rely on Fabry-Perot-type interference.

The simplest and most well-known conventional optical coating is the quarter-wave AR coating, in which the reflectivity between two dielectric media with refractive indices n_1 and n_3 is minimized by inserting a dielectric film with refractive index n_2 and thickness $\lambda/4n_2$ where $n_3 > n_2 > n_1$ in between (λ is the free-space wavelength). There is a wire array of more advanced optical coatings in use today; these sophisticated optical coatings design strategies often utilize many films of varying materials and thicknesses to achieve particular performance benchmarks, with architectures that are created and optimized using computer software. A variety of commercial software for thin film calculation and optimization is available, including Essential Macleod, FilmStar, Film Wizard and OptiLayer.

The vast majority of both simple and complex optical coatings use purely dielectric materials, often with thicknesses corresponding to a quarter-wave; in fact the index of Hecht's classic book *Optics* immediately redirects "Thin films" to "See Dielectric films" [1] and the first section of Macleod's *Thin-film Optical Filters* following the introductory theory chapter is called "Quarter- and Half-Wave Optical Thicknesses". It turns out that by relaxing this constraint that the materials comprising the substrate and the thin films be purely dielectric (i.e. transparent and lossless), coatings that minimize reflectivity of a surface can be made thinner than the standard quarter-wave dimension. One example is anodized titanium: by electrochemically forming thin layers of transparent titanium oxide on a titanium substrate, a variety of colors can be generated which are a result of wavelength-selective absorption [6]. Since the oxide is transparent, the optical absorption occurs upon repeated reflections from the oxide/titanium interface. In anodized titanium, light can be efficiently absorbed given layers that are approximately between $\lambda/(6n_{TiO2})$ and $\lambda/(5n_{TiO2})$, where n_{TiO2} is the refractive index of the oxide; the reason that the thickness can be smaller than the standard quarter-wavelength dimension

is that unlike for lossless dielectrics the phase shift upon reflection at the oxide/titanium interface differs from π due to the complex refractive index of titanium (e.g. at $\lambda = 600$ nm, $n_{Ti} \simeq 2.6 + 3.7i$).

In this chapter, we are going to demonstrate that strong optical thin-film interference effects can be observed even for highly-lossy dielectric films [7] [8] [9] [10].

2.2 New optical coatings with large losses

2.2.1 Basic understanding and formalism

The Fabry-Perot-type effect of conventional optical thin films utilizes constructive and destructive interference, with the optical phase controlled by gradual accumulation within the nearly transparent dielectric layers. The material losses in the dielectrics are usually assumed to be small such that light is gradually absorbed, and the interface reflection and transmission phase changes at the interfaces between the dielectric films can therefore be assumed to be either 0 or π, depending on the index contrast. Our approach instead utilizes highly-absorbing dielectrics (semiconductors at photon energies above the band gap in the first example) in which light is rapidly attenuated, together with metals which have finite optical conductivity. Combining these materials gives access to a range of interface reflection and transmission phase shifts which can be engineered by modification of the material properties (Fig. 2.3). The large optical attenuation within the highly-absorbing dielectrics and the concomitant nontrivial interface phase shifts lead to strong resonant behavior in films that are much thinner than the wavelength of light. We demonstrate these ultra-thin coatings on the surfaces of noble metals in the visible regime and show that deposition of nanometers of a lossy

dielectric on a metal results in dramatic modification of the reflectivity spectrum (and therefore color).

The equations describing the behavior of light incident from air ($n_1 = 1$) onto a lossy film with thickness h and complex refractive index $\tilde{n}_2 = n_2 + ik_2$, deposited on a metallic substrate with complex index $\tilde{n}_3$ (Fig. 2.4) can be found in optics textbooks [6]). The reflection coefficient for TE (s-polarized) light incident at an angleθ_1 is

$$\tilde{r} = \frac{\tilde{r}_{12} + \tilde{r}_{23} e^{2i\tilde{\beta}}}{1 + \tilde{r}_{12}\tilde{r}_{23} e^{2i\tilde{\beta}}} \tag{2.1}$$

where $\tilde{r}_{mn} = (\tilde{p}_m - \tilde{p}_n)/(\tilde{p}_m + \tilde{p}_n)$, $\tilde{p}_m = \tilde{n}_m \cos(\tilde{\theta}_m)$, $\tilde{\beta} = (2\pi/\lambda)\tilde{n}_2 h \cos(\tilde{\theta}_2)$, and $\tilde{\theta}_m = \sin^{-1}(\sin(\theta_1)/\tilde{n}_m)$ which is the complex-valued form of Snell's law (pp. 740-741 of [6]). For TM (p-polarized) light, $\tilde{p}_m$ is replaced by $\tilde{q}_m = \cos(\tilde{\theta}_m)/\tilde{n}_m$. The total reflectivity is given by $R = |\tilde{r}|^2$, and since we assume that the substrate is metallic such that there is no transmission, the absorption of the structure can be written as $A = 1 - R$. One noteworthy example is an asymmetric Fabry-Perot structure comprising a quarter-wave film (or odd multiples thereof, such that $h \simeq m\lambda/4n_2$, where m is an odd integer) on a perfect reflector (Fig. 2.4(a)). This resonator in the presense of moderate losses serves as an absorbing optical cavity in which the loss can be considered as a perturbation. In the absence of loss, this type of cavity functions as a phase-shifting element called a Gires-Tournois etalon [11]. Asymmetric Fabry-Perot cavities have been used for reflection modulation [12], resonant cavity enhanced (RCE) photodetection and emission [13][14], ferroelectric infrared detection [15], and other applications.

For a metal substrate in the perfect electric conductor (PEC) limit, $k_3 \to \infty$, so $\tilde{r}_{2,3} = -1$,corresponding to complete reflection with a phase shift of π in the reflected electric field (Fig. 2.4(a, b)), which makes $h \simeq \lambda/4n_2$ the lower limit on the thickness

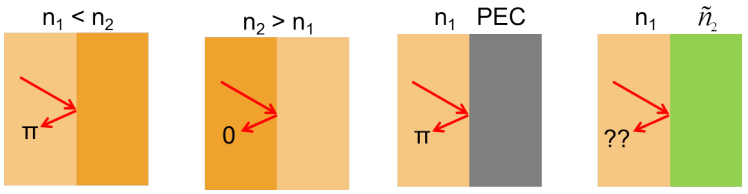

FIGURE 2.3: Phase shifts experienced by the electric field upon reflection from different materials. When light is incident from a lower index medium onto a higher index one (a), the reflection phase shift is π. Conversely, light incident from a higher index medium to a lower index one (b) experiences a phase shift of 0 in reflection. In the case of light incident from any material onto a perfect electric conductor (PEC), the reflection phase shift is always π. Unlike all of the previous cases, light reflection from a material with a complex refractive index creates phase shifts that are neither 0 nor π.

of a resonant cavity because a round trip inside such a cavity should accumulate approximately 0 phase (modulo 2π). At optical frequencies, however, metals have finite conductivity and therefore their complex index is finite [16] (similar metal-like complex indices can also be found in a variety of non-metallic materials at longer wavelengths such as, e.g., indium-tin-oxide in the near-IR [17], sapphire in the mid-IR [18] which we will get to in later sections, etc), so the reflection phase shift at the metal interface can vary (Figs. 2.3 and 2.4(c)). Likewise, if a dielectric film has large optical losses (k_2 on the order of n_2), the reflection and transmission phase shifts at the boundary between it and air are not limited to 0 or π as in the case for lossless dielectrics (Figs. 2.3 and 2.4(b, d)). These nontrivial interface phase shifts allow the total phase accumulation, which includes both the interface and propagation phase shifts, to reach approximately 0 (modulo 2π) for certain films with thicknesses significantly below $\lambda/4n_2$, creating an absorption resonance (note that the phase accumulation is close to but not precisely zero at this resonance condition when the system has high losses, which we will explain in sections 2.2.4 and 2.6). Since there is very little light propagation in such a thin structure, the material optical losses must be very high in order for the round-trip absorption to be significant. By combining these non-trivial interface phase shifts, the phase accumulated through propagation, and the attenuation of the wave as it propagates through

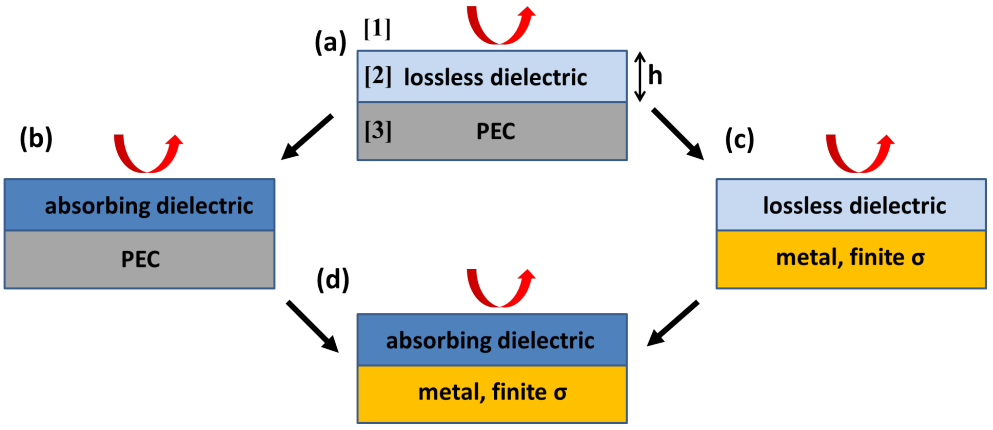

FIGURE 2.4: Schematic of incident light from medium 1 (air) being reflected from a structure comprising dielectric medium 2 with thickness h and metallic medium 3. (a) The case of the perfect electric conductor (PEC) metal, and a lossless dielectric. Since there is no absorption and no penetration into the metal, the reflectivity equals unity at all wavelengths. Resonators approaching this limit behave as phase shifting elements, known as Gilles-Tournois etalons . (b) An absorbing dielectric on a PEC substrate supports an absorption resonance for $h \approx m\lambda/4n_2$ assuming that the losses (k_2) are relatively small and m is an odd integer. No resonance exists for h smaller than $\lambda/4n_2$. (c) A lossless dielectric on a substrate with finite optical conductivity (e.g. gold at visible frequencies) can support a resonance for $h << \lambda/4n_2$ due to the nontrivial phase shifts at the interface between medium 2 and medium 3, but the total absorption is small since the only loss mechanism is one associated with the finite reflectivity of the metal. (d) An ultra-thin ($h << \lambda/4n_2$) absorbing dielectric on gold at visible frequencies can support a strong and widely tailorable absorption resonance.

the highly-lossy medium, a new type of optical coating can be designed (Fig. 2.4(d)) where losses are no longer considered as a perturbation but are an integral part of the design.

2.2.2 Implementation of gold/germanium optical coatings in the visible

We demonstrated these concepts at visible frequencies by modifying the reflectivity of a gold (Au) surface by coating it with evaporated germanium (Ge) films of a few nanometers in thickness, which creates broadband absorption resonances with the spectral position determined by the film thickness. The wide optical absorption band influences the color by suppressing the reflectivity in a portion of the visible spectrum. Ge was selected

because it is highly absorbing at visible frequencies (see Fig. 2.5(a)) due to direct electronic transitions which appear at energies higher than that of the L-absorption edge [19]. We coated an optically-thick (150 nm) Au film with Ge of thickness h between 7 nm and 25 nm by using electron-beam evaporation, which resulted in drastic changes in the reflectivity. The films were deposited by electron-beam evaporation using a Denton evaporator. Au was deposited at a rate of approximately 2 Å/s under a pressure of 10^{-6} torr without substrate heating, with the rate measured by a crystal monitor. Ge was deposited at a rate of 1 Å/s at a pressure of approximately 2 x 10^{-6} torr.

The complex refractive indices given in Fig. 2.5(a) and used in the calculation of the spectra in Fig. 2.5(c) and Fig. 2.6(c, d) were obtained by variable-angle spectroscopic ellipsometry (VASE) of optically-thick evaporated films (150 nm for Au and 1000 nm for Ge in the 400 - 850 nm range). In ellipsometry literature this sort of measurement is referred to as measuring the "pseudo dielectric function"; "pseudo" is in the name because of the assumption that a single reflection comes from a sharp interface between the material and the air [20]. We preferred this method to ellipsometry on thin absorbing films (e.g. about 10 nm Ge on a known substrate) because it decreases the number of unknowns from (n, k, h) to (n, k), which helps avoid over-fitting errors and non-unique solutions. It should be emphasized here that the complex index for Ge shown in Fig. 2.5(a) is different from what is often found in online databases for Ge. This is because most databases cite the complex index for crystalline Ge, whereas our evaporated films are most likely amorphous. In general amorphous and crystalline semiconductors are expected to have very different properties; as an example, crystalline Ge is an indirect bandgap material, whereas in amorphous Ge the bandgap is not as well defined.

We performed near-normal incidence measurements (7° incidence angle with unpolarized light) between 400 nm and 850 nm using a spectrophotometer with a photomultiplier

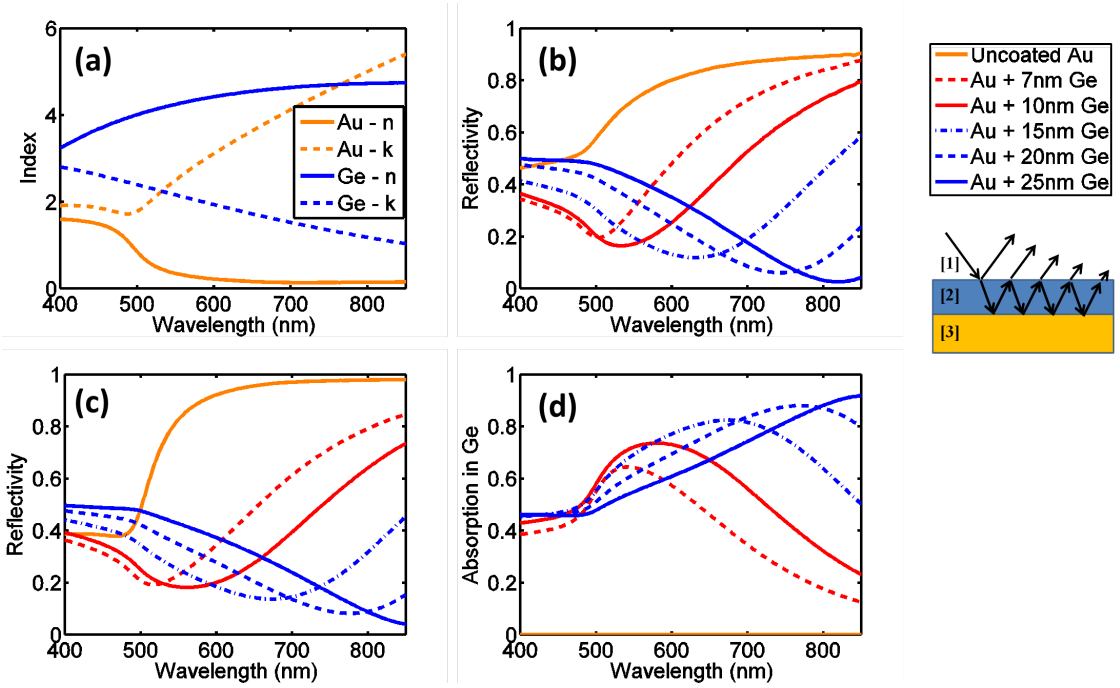

FIGURE 2.5: (a) Real and imaginary parts of the complex refractive indices of gold (Au) and germanium (Ge), obtained by variable angle spectroscopic ellipsometry. (b) Near-normal incidence (7°) reflection spectra of thick Au coated with 7, 10, 15, 20, and 25 nm of Ge. Inset: schematic of the Ge film on an Au substrate, showing a partial wave decomposition. (c) Calculated reflection spectra using Eqn. (2.1) and the optical constants in (a) corresponding to the measurement in (b). (d) Calculated fraction of the total incident light which is absorbed within the Ge layer.

tube (PMT). The near-normal incidence reflectivity spectra were taken using a Hitachi 4100 spectrophotometer with a tungsten lamp source and a photomultiplier tube in the 400 - 850 nm range. The angle-dependent, polarization-dependent spectra were taken using a Woollam WVASE32 spectroscopic ellipsometer using reflection/transmission (R/T) mode. The stability of the optical properties over extended periods of time is discussed in section 2.2.5. The experimental reflectivity spectra for Ge films of thickness between 7 nm and 25 nm coated on Au are given in Fig. 2.5(b).

The calculated reflectivity spectra corresponding to the measurements in Fig. 2.5(b) are obtained by using Eqn. (2.1), and are shown in Fig. 2.5(c). In the case of Fig. 2.5(c), we simulated unpolarized incident light by calculating the reflectivity for both s- and p-polarizations, and taking an average of the two to simulate unpolarized light. Excellent

agreement is obtained between the experimental data and the calculations which used the complex indices from the VASE measurements. We also computed the total fraction of the incident light that is absorbed within the Ge film only (Fig. 2.5(d)), showing that the majority of the absorption occurs in this layer as opposed to the underlying Au. For example in the case of the 15 nm Ge sample at a wavelength of approximately 670 nm, over 80% of the incident light is absorbed in the Ge layer while only about 4% of the light is absorbed in the Au, with the remaining 15% of the light reflected. The spectral position of the absorption band, which corresponds to the reflectivity minimum, depends on h, with a shift of approximately 20 nm in wavelength for every 1 nm change in h across the visible spectral range. This strong absorption resonance occurs in a film that is much thinner than the wavelength of light (e.g. $\approx \lambda/(13n_2)$ at $\lambda \approx 560nm$, with $n_2 \approx 4.3$ for the 10 nm Ge film in the calculation) – a result of the interplay between the complex reflection coefficient at the Ge/Au substrate and the large but finite attenuation of light within the Ge film [see section 2.2.4 for a detailed explanation based on decomposition into partial waves]. Note that in our material system, the absorption coefficient of Ge decreases with increasing wavelength and the properties of Au slowly approach those of a PEC, so the resonant absorption thickness will slowly converge to $h \approx \lambda/(4n_2)$ at long wavelengths and films of large thickness.

Because these coatings are much thinner than the wavelength of light, there is little phase accumulation due to the propagation throught the film compared to the reflection phase change upon reflection. As a result, the optical properties of these coatings are robust with respect to the angle of incidence. We demonstrated this by measuring the s- and p-polarized reflectivity of the sample with 15 nm of Ge, which shows that the absorption feature remains prominent for angles of incidence from 0° and ≈ 60° in both polarizations (Fig. 2.6(a, b)). The corresponding calculated spectra are shown in in Fig.

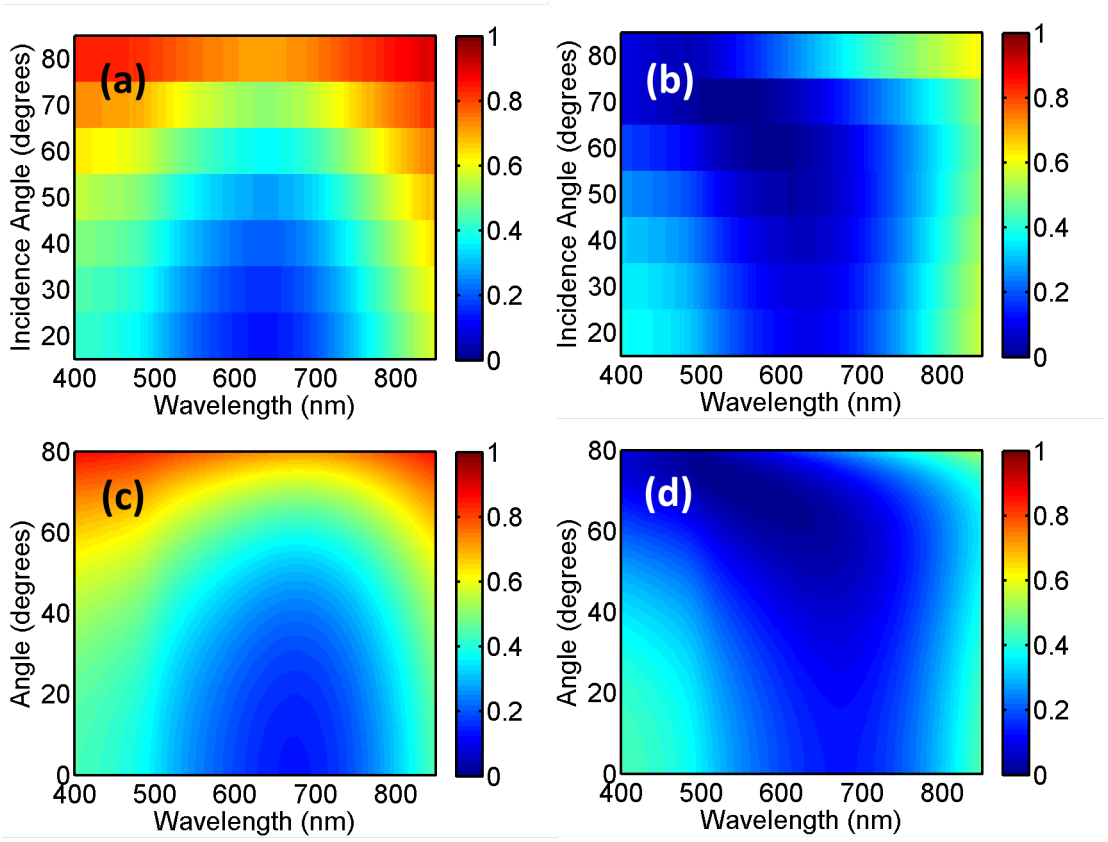

FIGURE 2.6: (a, b) Experimental reflectivity spectra for s- and p-polarization, respectively, for angles of incidence from 20° to 80° for an Au film coated with 15 nm of Ge. (c, d) The calculated spectra corresponding to those in (a, b) using Eqn (2.1).

2.6(c, d).

The large change in reflectivity allows for the coloring of metals using these films of subwavelength thickness. In Fig. 2.7, we show a photograph of samples of Au coated with Ge from 0 nm to 25 nm in thickness, creating an array of colors including pink, blue, and violet. The photograph was taken with a Canon PowerShot ELPH 310 HS digital camera under illumination from regular white ceiling fluorescent lights. Another photo of the same samples is shown in Fig. 2.8, this time on a black background with diffuse light illumination.

In samples (a) - (i), the substrate material for Au deposition was a polished silicon wafer. In samples (j) - (l), however, the rough, unpolished back-side of the wafer was used, and the various colors are still clearly visible, indicating that the present effect is relatively

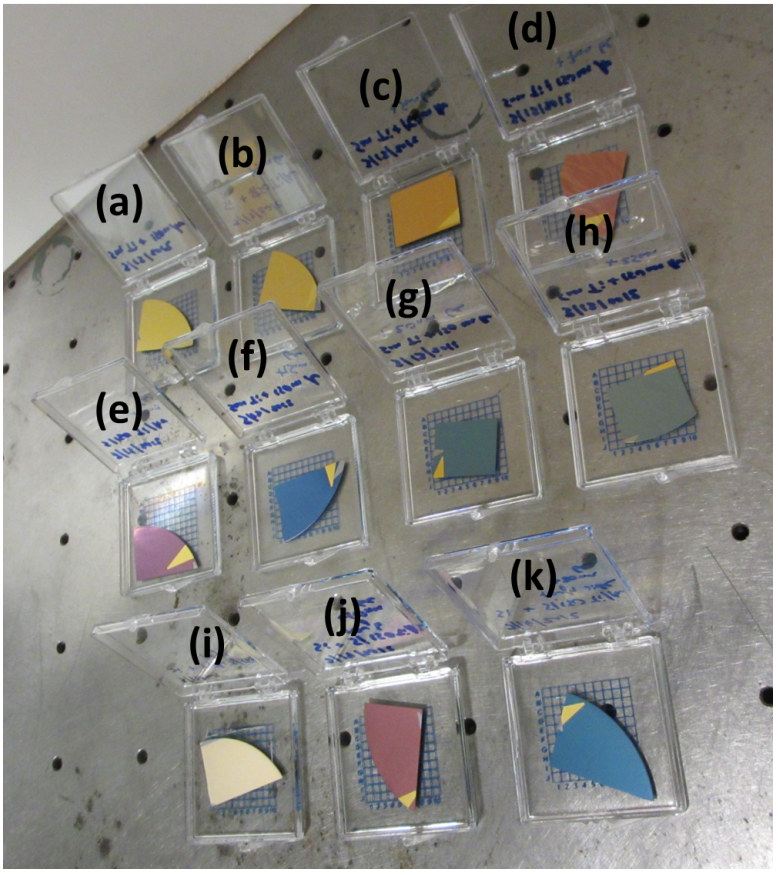

FIGURE 2.7: Wide variety of colors formed by coating Au with nanometer films of Ge. (a - h) 0 nm, 3 nm, 5 nm, 7 nm, 10 nm, 15 nm, 20 nm, and 25 nm of Ge deposited on optically-thick Au, which was deposited on polished silicon. The clip marks from mounting in the e-beam evaporator are visible. (i - k) 0 nm, 10 nm, and 20 nm of Ge deposited over 150 nm of Au, on a rough (unpolished) silicon substrate.

insensitive to surface roughness. This is to be expected given the small dependence of the reflectivity on the incidence angle shown in Fig. 2.6 and the fact that the length scale of the roughness (microns) is very different from the film thickness (nanometers), but nonetheless runs against intuition given our every-day experience with thin film interference effects. We also show several samples of silver (Ag) colored via the same principle; in particular a color similar to that of gold is induced in Ag samples by coating them with approximately 7 nm of Ge (Fig. 2.9).

We note that the modification of the absorption and color of metals has recently been

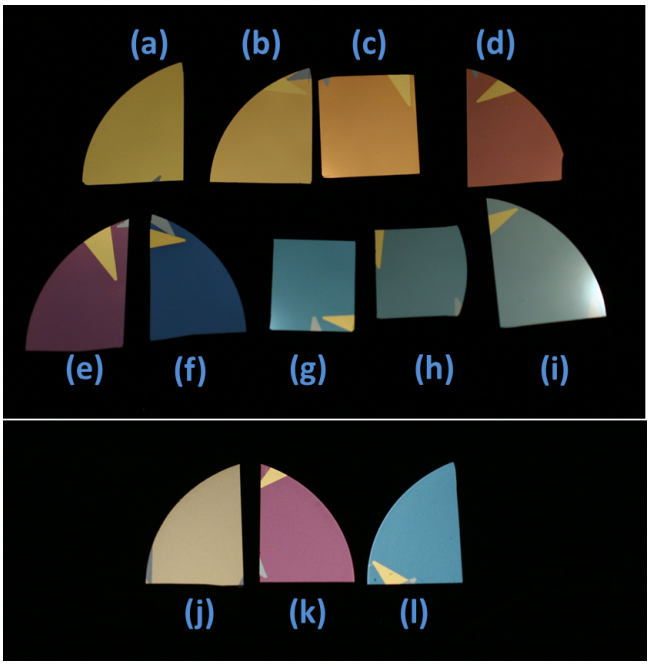

FIGURE 2.8: Another photograph of the samples shown in Fig. 2.7.

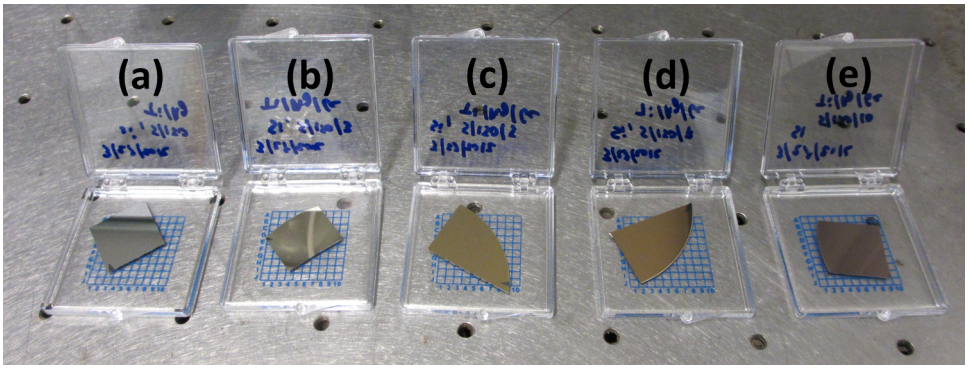

FIGURE 2.9: (a-f) Thick silver (Ag) films coated with 0, 3, 5, 7, 10, and 15 nm of evaporated Ge, respectively

demonstrated via nano-, micro-, and macro-structuring of the metal surface by lithography and etching, femtosecond laser ablation, or other methods [21][22][23][24][25]. By comparison, our technique is non-damaging to the metal surface, can be reversed by chemical etching of the absorbing dielectric layer, does not require any serial fabrication steps, and involves only smooth surfaces which may be advantageous for integration into devices. Furthermore, the presently demonstrated approach does not involve multiple scattering, metallic nano-cavity resonances, or surface plasmons, as in Refs.

[21][22][23][24][25] but is instead a result of simple albeit counterintuitive thin film interference; this simplicity allows for the prediction and design of new coatings via simple analytical expressions such as Eqn. (2.1).

2.2.3 Making multi-color images with patterned ultra-thin films

In addition to continuous coatings, single- and multi-color images can be created by combining the deposition of ultra-thin absorptive films with conventional lithographic techniques. As an example, we generated several color images on a glass slide with feature sizes ranging from microns to millimeters by using multi-step contact photolithography with alignment. Photoresist was spun onto a glass slide (Shipley S1813, 4000 rpm), was exposed through chrome-coated glass photomasks using a Karl Suss MJB4 mask aligner, and was then developed in CD-26 for 60 seconds. The Au and Ge films were then deposited through the resulting mask, with the excess material removed via liftoff in acetone with ultrasonic agitation (Fig. 2.10). The deposition thicknesses were 65 nm Au (preceded by a 5 nm Ti adhesion layer) to create an optically-thick layer, followed by 7 nm, 4 nm, 4 nm, and 10 nm of Ge, creating overall Ge layers of thickness 7 nm, 11 nm, 15 nm, and 25 nm, respectively. Five colors are demonstrated: gold (0 nm of Ge), light pink ($\approx$ 7 nm), purple ($\approx$ 11 nm), dark blue ($\approx$ 15 nm), and light blue ($\approx$ 25 nm). (Fig. 2.11)

2.2.4 Partial-wave explanation

In this section, we focus on the physical mechanism of the ultra-thin film resonance and explain the conditions in which it can occur. We begin by analyzing the total reflectivity from a structure like that in Fig. 2.4(b), where medium 2 has complex refractive index

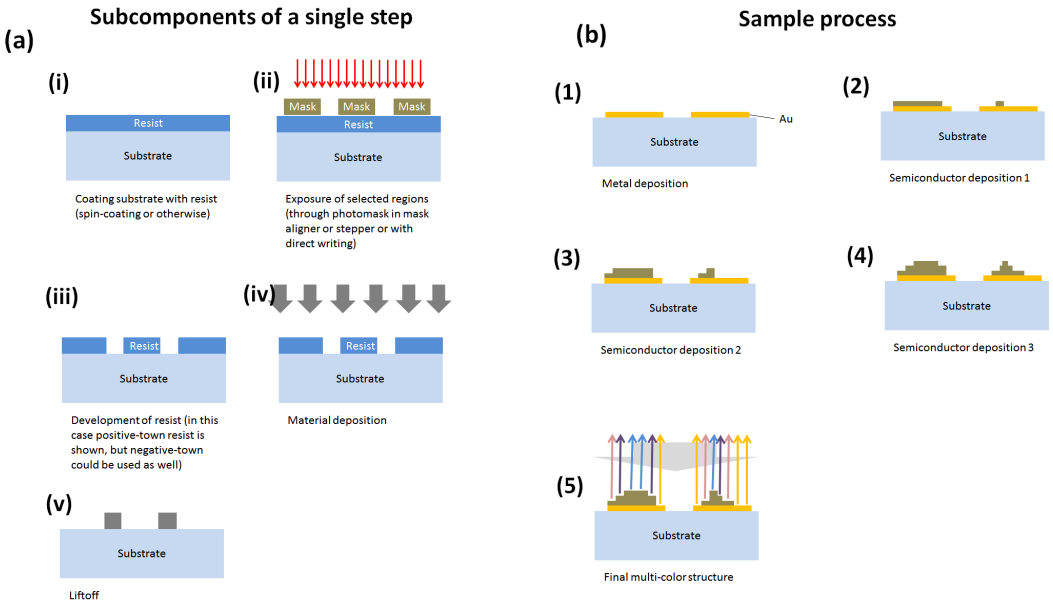

FIGURE 2.10: Explanation of the photolithography process used to generate the patterns in Fig. 2.11. In (a), a single sub-step of lithography, deposition, and liftoff is shown. This process is repeated many times with alignment in between steps as shown in (b) to finally create the multi-color images.

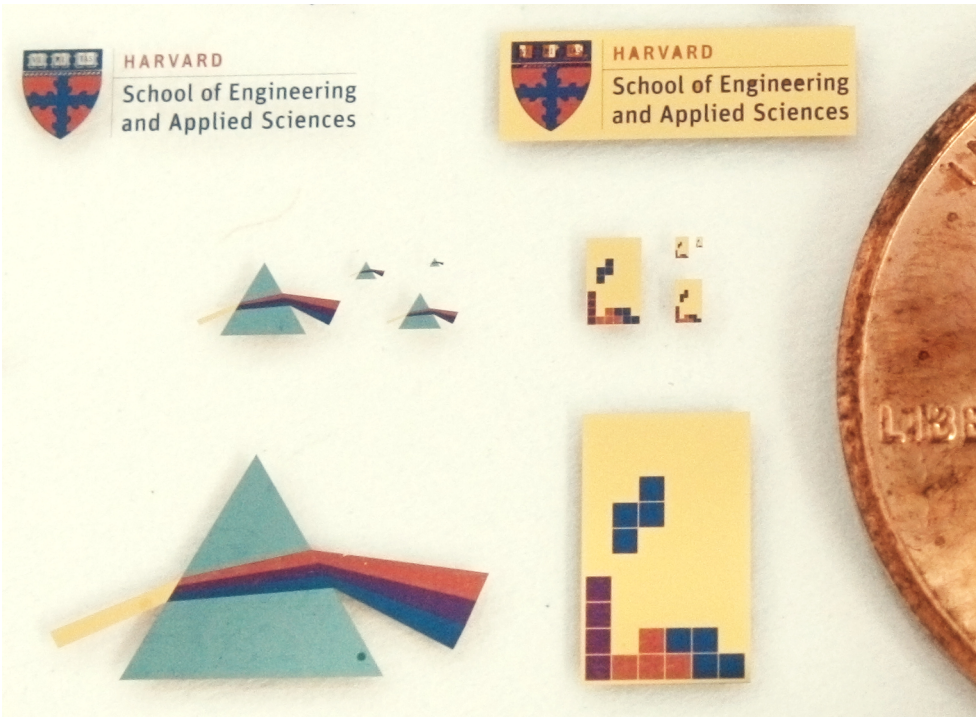

FIGURE 2.11: Photograph of color images generated via multi-step patterning of ultra-thin Ge films, with the edge of a United States penny included for size comparison. Five steps of photolithography with alignment are used to selectively deposit an optically-thick layer of Au on a glass slide, followed by Ge layers of either 7 nm, 11 nm, 15 nm, or 25 nm. This yields light pink, purple, dark blue and light blue colors, respectively. Among the demonstrated patterns are the logo and shield of the School of Engineering and Applied Sciences; these are a trademark of Harvard University, and are protected by copyright; they are used in this research with permission.

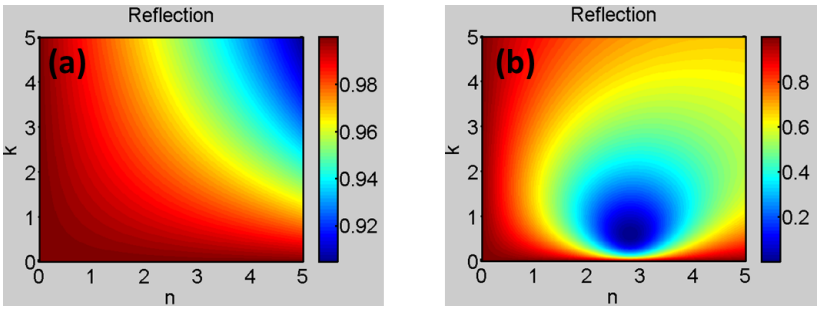

FIGURE 2.12: (a, b) Reflectivity for a film with complex index n + ik and h = 10 nm and 50 nm, respectively, on a perfect electric conductor (PEC) substrate, at $\lambda = 532$ nm.

$n + ik$ and medium 3 is a perfect electric conductor (PEC). We plot the reflectivity at $\lambda = 532$ nm as a function of n and k, and find that for a film with $h = 10$ nm the reflectivity stays close to 1 for all values of (n, k) from 0 to 5, but for $h = 50$ nm a zero in reflectivity occurs at $2.81 + 0.61i$, which corresponds roughly to a $\lambda/4n$ (quarter-wave) film (Fig. 2.12). This can be understood as a critical coupling condition to the lossy asymmetric Fabry-Perot cavity formed inside the film [26] [27] (for further discussion see section 2.4.1). No absorption resonance exists for a film thinner than this with a PEC substrate.

When the conductivity of the substrate becomes finite, however (as is the case for metals at visible frequencies (Fig. 2.4(d)), the situation changes significantly. For example, in Fig. 2.12 we plot the reflectivity vs (n, k) of the films given that the substrate is Au at $\lambda = 532$ nm ($n_3 = .44 + 2.24i$). We observe that when the index of the film is $4.3 + 0.71i$, the reflectivity drops to zero even though the film thickness is only 10 nm, corresponding to $\approx \lambda/12n$.

To better understand the mechanism leading to the reflectivity minimum at $4.3 + 0.71i$, we expand Eqn. 2.1 into partial waves to get $r = \sum_{m=0}^{\infty} r_m$ where $r_m = t_{12} r_{23}{}^m r_{21}{}^{(m-1)} t_{21} e^{2mi\beta}$ for $m > 0$ and $r_{pq} = (\tilde{n}_p - \tilde{n}_q)/(\tilde{n}_p + \tilde{n}_q)$, $t_{pq} = 2\tilde{n}_p/(\tilde{n}_p + \tilde{n}_q)$, and $r_0 = r_{21}$. With this formulation, we can plot the reflectivity taking into account only the first $m + 1$

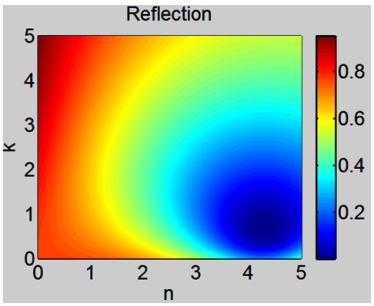

FIGURE 2.13: Reflectivity for a film with complex index $n + ik$ and $h = 10$ nm on a gold substrate at $\lambda = 532$ nm.

partial waves (the +1 is because m begins at 0) to see how the reflectivity evolves as more and more partial waves are included. We do this in Fig. 2.14 (a) and (c), where we assume that the substrate is a PEC or Au at 532 nm, respectively, $h = 10$ nm, and $n_2 = 4.3 + ik$ where k can vary from 0 to 2.1 (see legend). We see that in the PEC case the final reflectivity is close to 1 for all values of k. The partial reflectivity goes above 1 when only the first 1-2 secondary waves are taken into account, but the value drops back down below 1 when the other partial waves are included, preserving energy conservation. In the case of Au, however, the reflectivity changes significantly with changing k, even reaching precisely 0 at approximately $k = 0.7$. Note that for all cases with significant loss ($k >> 0$) the partial reflectivity reaches its final value of after only 3-4 partial waves are accounted for (corresponding to 3-4 passes through the lossy film).

Since the partial wave amplitudes are all complex quantities, we can plot them in the complex plane, where they are represented as vectors (referred to as "phasors") (Fig. 2.14 (b, d)). The first phasor r_0 begins at the origin, r_1 begins at the end of r_0, etc. The total reflectivity R is the magnitude-squared of the final value of the phasor trajectory in the complex plane (R is identically zero if the trajectory returns to the origin). In the case of the PEC substrate, the first few partial waves all move away from the origin, indicating constructive interference and therefore a large final value of R (Fig. 2.14(b)). With the Au substrate, however, the phasor trajectory makes a sharp turn after the first

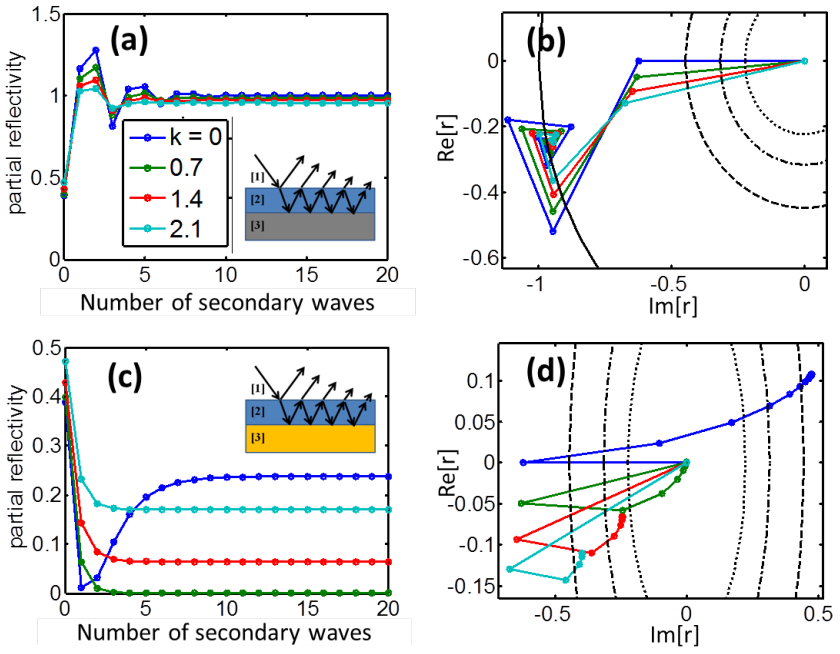

FIGURE 2.14: (a) Partial reflectivity from the sample taking into account the initial reflection between mediums 1 and 2, and also 0, 1, ... secondary partial waves where the first partial wave comes from a single round trip through medium 2, the second from two round trips, etc. The substrate is a perfect electric conductor (PEC), with $n_3 = \infty + i\infty$. Medium 2 has index $4.3 + ik$, where k is given in the legend of (b), $\lambda = 532$ nm, and $h = 10$ nm. (b) Phasor diagram corresponding to (a), showing graphically how all values of k within the range of 0 - 2.1 lead to roughly the same overall reflection coefficient R (close to 1). The circles each represent a particular reflectivity ($R = 1$: solid line, $R = 0.2$: dashed line, $R = 0.1$: dot-dashed line, $R = 0.05$: dotted line), which is reached if the phasor trajectory terminates on a particular circle. (c) Partial reflectivities as in (a), but with $n_3 = 0.44 + 2.24i$, the complex index of Au at 532 nm. (d) Phasor diagram corresponding to (c). The resulting values of R can be read off by using the circles as a reference. In particular, the $k = 0.7$ trajectory ends up at the origin, yielding $R = 0$.

partial wave, a result of the near-zero phase shift that the light experiences reflecting from a lossy dielectric into a low-optical-conductivity metal (such as Au at 532 nm), opening the possibility that the complex sum of the secondary partial waves could partially or totally cancel r_0.

In the phasor diagrams in Fig. 2.14(b, d), we drew circles centered on the origin corresponding to reflectivities $R = 1$, 0.2, 0.1, and 0.05 (solid line, dashed line, dot-dashed line, dotted line, respectively). This allows us to visually identify the reflectivity by using the circles as references; for example, since the $k = 1.4$ (red) trajectory terminates

between the dotted and dot-dashed circles, we know that R is between 0.05 and 0.1. We see that varying k results in a wide range of reflectivities. In particular, the $k = 0.7$ trajectory terminates precisely at the origin, resulting in $R = 0$ (corresponding to 100% absorption). The reflectivity minimum in n-k space is very broad (Fig. 2.13), so even when the values do not precisely match those of the minimum-reflectivity condition, a significant absorption resonance can still be observed. This is what happens for evaporated Ge films in our experiments (Fig. 2.5(b, c)), which at 532 nm correspond to the cyan curve in Fig. 2.14(a). We note that while the $R = 0$ condition cannot be achieved with the Ge/Au material system in the visible at normal incidence due to the limited degrees of freedom (k_2 and n_2 can be tuned by controlling the incident wavelength, but not independently of each other), such a condition can be found for some incident angles. For example, the reflectivity in Fig. 2.6(b) drops to 0 for $\theta \approx 70^\circ$ and $\lambda \approx 535$ nm.

2.2.5 Material characterization of gold/germanium optical coatings

We performed atomic force microscopy (AFM) measurements on some of the bare and coated substrates to obtain an estimate of the surface roughness post-deposition. For the films deposited on polished Si wafers (Figs. 2.5, 2.6, and 2.7(a-h) in the main text), we found that the root-mean-square (RMS) roughness was approximately 1.24 nm for the uncoated Au sample, 0.47 nm for the sample coated with 7 nm of Ge, and 0.37 nm for the sample coated with 20 nm of Ge (Fig. 2.15). We also performed contact profilometer measurements on the samples deposited on the rough back-sides of Si wafers (Fig. 2.7(k-m) in main text), and found that the RMS roughness was approximately 680 nm, with the lateral feature size of approximately 5-10μm.

Long-term stability of the highly-absorbing films may be a concern for some applications. In the case of our experiments, the measurements were within 1-2 days of the deposition,

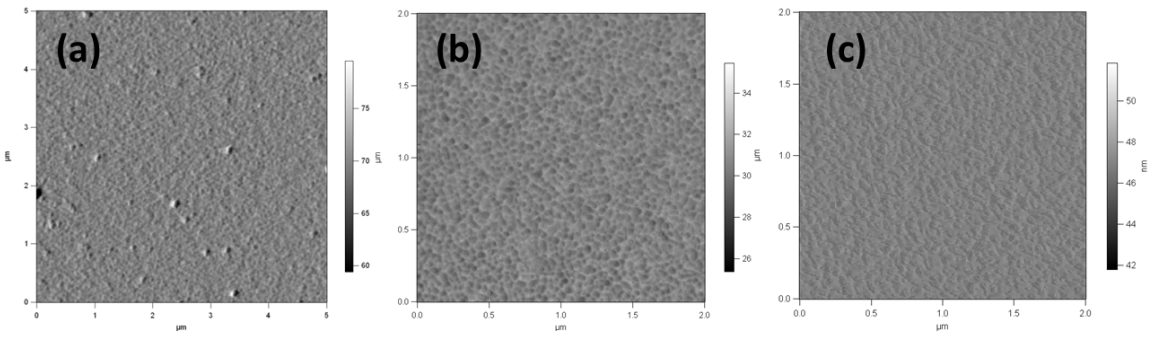

FIGURE 2.15: AFM images of 5 m x 5 m patches of the uncoated Au sample (a), the Au sample with 7nm of Ge (b), and the Au sample with 20nm of Ge (c), all deposited on a polished Si substrate.

and the samples were then stored in gel-boxes outside of any cleanroom environment. No special care was taken to protect the samples, which were also periodically completely exposed to ambient conditions. We observed no perceptible change in the colors of the samples over a four month period, indicating that they are relatively stable. We also performed another set of reflectivity measurements corresponding to that of Fig. 2.6 on the same sample, and observed very little change over these four months (Fig. 2.16). However we observed that even a 30 minute dip in water removed nearly all of the Ge. Also in one instance all of the Ge seems to have dissolved when samples were sent to collaborators by mail via the US Postal Service (USPS); we still do not know precisely what caused the Ge to dissolve in transit.

For long-term stability, a variety of methods may be required to passivate and protect the semiconductor surface. If Ge is used as in the present work, then this can be achieved by chemical passivation methods (e.g. sulfide functionalization) [28], which should not significantly affect the optical properties of the films. Alternatively, a capping layer may be deposited on top of the semiconductor to protect against chemical or mechanical damage. One possibility is sputtered hydrogenated amorphous germanium (a-Ge:H), which has been used to protect, for example, Ge-based nuclear radiation detectors and can be tens of nanometers thick [29]. Another is the hard carbon coating, also known

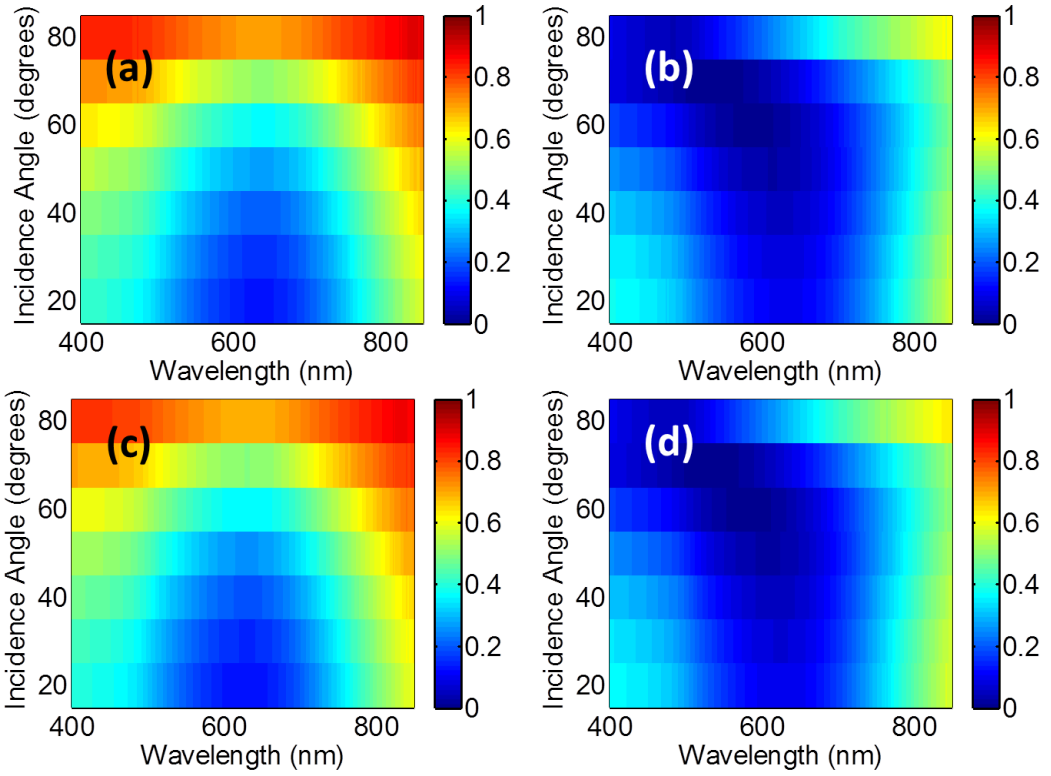

FIGURE 2.16: (a, b) Experimental reflectivity spectra for s- and p-polarization, respectively, for angles of incidence from 20 to 80 for an Au film coated with 15 nm of Ge, as taken one day after the deposition of Ge. This is the same data as presented in Fig. 2.6(a, b). (c, d) Experimental reflectivity spectra corresponding to those in (a, b), taken approximately 4 months after the deposition.

as the diamond-like coating (DLC), which adheres well to germanium and silicon, and is extremely resistant to both chemical and abrasive environments [30] [31].

A capping layer with a thickness of tens of nanometers or more may significantly affect the observed optical properties, depending on the optical properties of the material and its thickness. To test this, we performed 4-layer transfer matrix calculations, including a 10 nm DLC layer on top of the Ge. This thickness was chosen because it was the thinnest DLC layer that was analyzed as a protective coating in ref. [31], and the complex refractive index was interpolated from the data provided in ref. [30]. The resulting reflection spectrum was nearly unaltered (Fig. 2.17). A thicker layer may change the reflectivity properties significantly; however based on our calculations the ultra-thin absorption resonances can still be successfully designed. In fact, the capping

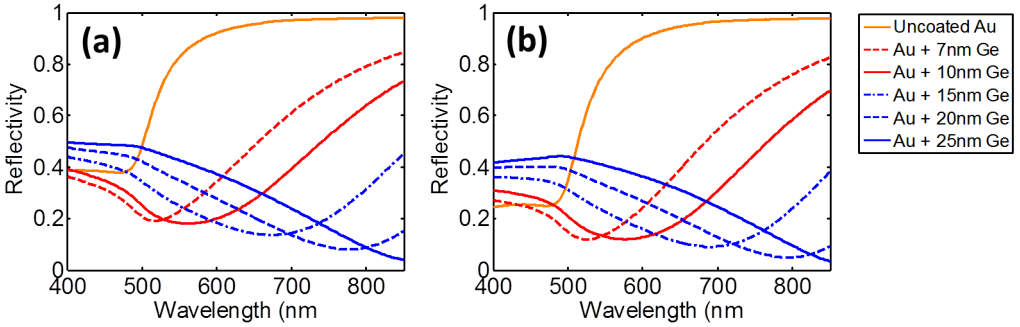

FIGURE 2.17: Normal incidence reflectivity calculations of a Au/Ge system for Ge thicknesses between 0 nm and 25 nm as in Fig. 2(c) in the main text with (a) no protective coating and (b) a 10 nm diamond-like coating (DLC)

layer can be seen as an additional degree of freedom in the design of these thin optical coatings, as is seen in Section 2.3.

2.2.6 Equivalent reflecting material: distinguishing pigments and interference colors

Suppose that one desired to color an object such as a flat piece of metal. Two common processes come to mind: painting and thin film interference (or other structural coloring). With the application of paint, the metal acquires the color of the pigment in the paint because all of the light is reflected, scattered, or absorbed before it ever reaches the metal surface. In this way, paint is a method of coloring which is substrate-agnostic: whether the metal was silver, gold, or copper, it will appear blue when covered with blue paint. The situation is different for objects colored by thin film interference. Oil films on water can appear to be any color of the rainbow, despite that fact that small quantities both oil and water are mostly transparent. In this case, the optical properties of the substrate underlying the film matter a lot, because light bounces back and forth in the film multiple times.

Most of the time one can easily visually determine if an object is painted or colored by thin film interference: a painted surface looks more or less the same from every viewing angle, whereas the reflection from optical thin films changes color and intensity depending on the angle at which you hold it. This is because the optical path length through the film depends on the viewing angle, and it is this length that determines the interference condition [16]. However this effect becomes less significant as the films become thinner, until it is nearly impossible to visually tell the difference between a painted surface and one colored with ultra-thin interference coatings. Transparent films at such tiny thicknesses do not significantly affect the color of the substrate but, as we have now seen, highly-absorbing films do.

We decided to explore whether it was possible to use optical techniques to determine if an unknown sample is a solid block of material, is coated with a smooth paint, or is made up of an ultra-thin film coating on a substrate. In otherwirds, can an equivalent semi-infinite medium can be defined which has the same reflectivity spectra as the combined substrate/film structure for various angles of incidence?

To explore this, we used the concept of "input optical admittance or "surface optical admittance", which is sometimes used to analyze optical thin film assemblies (e.g. ref. [2]). For any arbitrary collection of films given a particular incidence angle and polarization, one can define a single surface admittance at an interface between medium 1 and medium 2, which takes into account the effect of all of the layers underneath (2, 3, 4, etc..). This is analogous to defining a single electrical admittance (or, equivalently, impedance) for a circuit comprising many elements. For materials without a magnetic response (permeability $\mu = 1$, which is usually small at optical frequencies (ref. [2])), the surface optical admittance is directly proportional to a surface refractive index, and we will limit ourselves to this case.

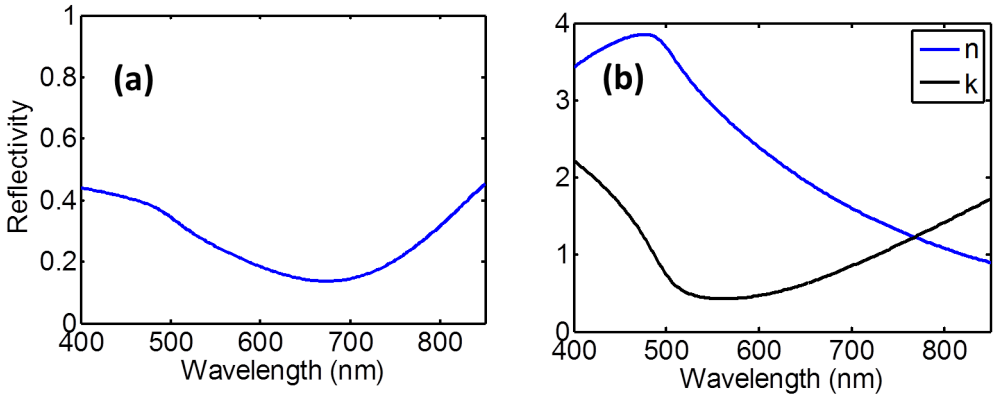

FIGURE 2.18: Calculated reflectivity for normal incidence from a gold surface coated with 15 nm of Ge (a) and extracted surface refractive index (b)

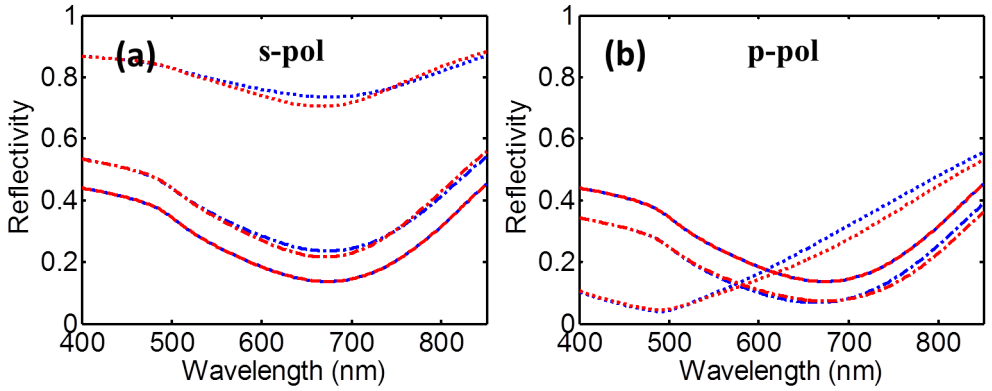

FIGURE 2.19: Calculated reflectivity spectra for oblique incidence ((a) s-polarization and (b) p-polarization) from the layered geometry (blue) and from a flat infinite half-space with complex refractive indices (n, k) given in Fig. 2.18(b) (red). The reflectivity data for $\theta = 0°$ is shown with the dashed curves, for $\theta = 40°$ with the dot-dashed curves, and the $\theta = 80°$ with the dotted curves.

For example, we analyzed the structure comprising an Au substrate with 15 nm of Ge (blue dot-dashed curve in Fig. 2.5(b, c, d), and the data of Fig. 2.6) and calculated the normal incidence reflectivity (Fig. 2.18(a)) as well as the surface refractive index (Fig. 2.18(b)). The extracted values for the surface refractive index (n and k) are such that one could reasonably imagine a real material (or a metamaterial) with these parameters. We used these values of n and k to calculate the reflectivity at several oblique angles for both s- and p-polarization, and compared them to the actual calculated reflectivities from the layered system (Fig. 2.19).

The match is not perfect, which means that strictly speaking one cannot define a homogeneous semi-infinite medium which is completely equivalent to the layered system when looking at the reflection properties. However, the reflectivity curves actually match reasonably for both p- and s- polarization for all incident angles, indicating that it is possible to define a semi-infinite medium which *nearly* reproduces the optical properties of the layered system. This means that, to an approximation, one can also define quantities such as the pseudo-Brewster angle [32] for our layered surface.

This is related to a common problem in spectroscopic ellipsometry, which is a sophisticated technique used to determine both complex refractive indices of solids and thin films and film thicknesses. While modern ellipsometers are sensitive to the presence of films down to a monolayer in thickness, they are unable to simultaneously determine the thickness and refractive index of an ultra-thin film if both are unknown [33].

2.2.7 Potential applications of highly-absorbing coatings in the visible

The approach of using ultra-thin, absorptive dielectric films as optical coatings is very general and can be applied to applications across a range of frequencies, starting with simple absorbers and color filters. The large change in optical properties given relatively small changes in material thickness can be used for sub-nanometer optical thickness monitoring of the deposition of semiconductor films. The coloring of metals with nanometer-thick films of inexpensive material may prove useful in various aspects of design and the visual arts. Additionally, creating patterned structures comprising ultra-thin absorbing coatings using conventional fabrication techniques introduces new capabilities for labeling, printing, and displaying information.

As with all instances of destructive interference, conservation of energy maintains that light cannot just disappear: it has to go somewhere or be absorbed. For the case of lossless thin films (such as soap bubbles), any destructive interference in reflection must correspond to constructive interference in transmission, and vice versa. When light shines on a sample with an opaque substrate, such as gold in our experiments, any light that is not reflected must be absorbed by the structure.

While light absorption is often considered to be undesirable in optical systems like microscopes and telescopes, there is a wide range of optical and optoelectronic devices for which absorption is a key feature. Most systems which require spectral filtering utilize wavelength-dependent optical absorption. Perhaps more importantly, the efficiency of light-harvesting devices such as solar cells and photodetectors can benefit greatly from enhancement of the total amount of light that is absorbed in their active layers.

Various approaches have been pursued to enhance light absorption in thin film solar cells including roughened surfaces, gratings, photonic crystals, plasmonic nanoparticles and dielectric nano- and microspheres with whispering gallery and Mie resonances, to name a few [34]. Many of these have promise, but significant concerns over the cost remain. While high costs may be tolerated for ultra-high-efficiency photovoltaics for specialized applications, one may question the practicality of spending hundreds or thousands of dollars on high resolution lithography to improve the efficiency of cheap, commodity solar cells.

From this perspective, our thin film structures which are able to absorb large fractions (e.g. 70 - 80%) of incident light in ultra-thin semiconductor films appear to be prime candidates for integration into light harvesting devices. Since there are no nanofabrication steps required beyond thin film deposition, large area absorbing films can be created

cheaply and efficiently.

The high degree of absorption in semiconductors makes them excellent candidate materials for these ultra-thin coatings, potentially enabling new types of photodetectors with enhanced quantum efficiency that require orders of magnitude less semiconductor material, significantly decreasing the material cost and growth time (compared to, e.g., resonant-cavity enhanced photodetectors which have an absorbing layer inside a wavelength-scale Fabry-Perot cavity [14]). Solar cell applications could also benefit from the large spectral bandwidth of the absorption resonances. Furthermore, in solar cells there is a tradeoff between thickness and material purity which is related to charge carrier lifetimes in materials with defects [35]; making ultra-thin highly-absorbing layers could relax this purity constraint, further reducing costs.

In fact, one such device has already been demonstrated. Last fall Dotan et alpublished a study parallel to our own work which came out only three weeks after our initial report, featuring 10 to 50 nanometer thick iron oxide films deposited on metallic back-reflectors and used as a water splitting cells which generate hydrogen from sunlight [36]. Conventional iron oxide water splitting cells suffer from the poor electronic properties of iron oxide, significantly limiting performance. By utilizing the ultra-thin-film interference phenomenon, the authors were able to significantly enhance the efficiency of these cells without utilizing costly nanoscale fabrication techniques. We believe that many more light-harvesting devices using ultra-thin-film interference are on the horizon.

2.3 Multi-layer ultra-thin film optical coatings

As previously mentioned, modern designs of optical coatings often involves many-layer optical stacks of films with different refractive indices and different thicknesses [2]. Often

times these designs become so complex that designing them demands computer software [37]. In principle, these stacks can be arbitrarily large as long as the materials remain lossless, and correspondingly the reflectance and transmittance spectra can become arbitrarily complex. In the case of very lossy coatings like the ones we describe in this chapter, there is a limit to the complexity and overall thickness of a stack of optical coatings due to the large optical absorption losses: if the film stack is too thick, light will never make it to the bottom and hence the bottom of the stack will have no effect on the reflectivity (in this case the transmittance is trivially 0).

Nethertheless it is worth exploring if relatively thin multi-layer coatings can bring added functionalities. In this section, we show that the functionality of deeply subwavelength optical interference coatings and absorbers can be augmented by integration of transparent layers on top of the lossy layers. These can be used as protective coatings for harsh environments, as transparent electrodes for optoelectronic devices, or to modify the optical interference conditions. Here, we show that an additional sub-quarter-wave layer of a transparent dielectric can be used as another degree of freedom in tailoring the absorption within ultra-thin lossy layers.

In the previous section, we used uniform evaporated films of amorphous Ge of thickness between 5 nm and 25 nm on an optically-thick gold substrate to obtain colors including various shades of pink, violet, and blue (Fig. 2.20(a)). In the work described in this section we used sputtering to deposit an additional sub-quarter-wave layer of aluminum oxide (Al_2O_3) on top of the Ge coatings to both protect the coatings and alter the reflectivity (Fig. 2.20(b)).

To limit the number of depositions as well as to demonstrate the full range of possible thicknesses of the Au/Ge system, we developed a deposition method which forms a

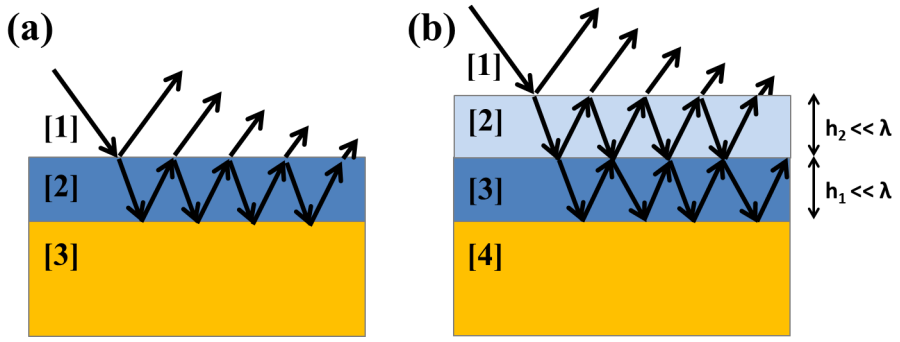

FIGURE 2.20: (a). Schematic of the thin film geometry used in ref. [8] as well as the previous section, which is the basis of the work presented in this section. A continuous film of amorphous germanium (Ge, shown as dark blue) of subwavelength thickness is deposited over a gold (Au) substrate, and the reflectivity is probed from the top. (b). A subwavelength layer of transparent alumina (Al_2O_3) is deposited over the structure in (a).

thickness gradient of the Ge film on an Au substrate. This allows us to have access to all thicknesses of Ge on a single sample. After coating a section of silicon wafer with an optically-thick ($\approx$ 150 nm) layer of Au, we inserted the sample Au-side-down into an electron beam evaporator for deposition of amorphous Ge. We modified the path between the crucible and the sample by introducing a slit aperture into the chamber (Fig. 2.21). The aperture changes the line-of-sight between the crucible and the sample so that the middle of the sample "sees" a large portion of the crucible, while points farther away from the middle of the sample see progressively less of the crucible. As a result, the deposition rate varies across the sample, and a gradient of thickness can be generated. The distances between the crucible and the aperture and between the aperture and the sample were 16 cm and 15.2 cm, respectively, the width of the slit aperture was 8 mm wide, and the melted Ge in the crucible is approximately circular with a diameter of 2 cm. While the dynamics of the deposition are beyond the scope of this work, back of the envelope calculations indicate that the thickness profile is expected to be roughly linear.

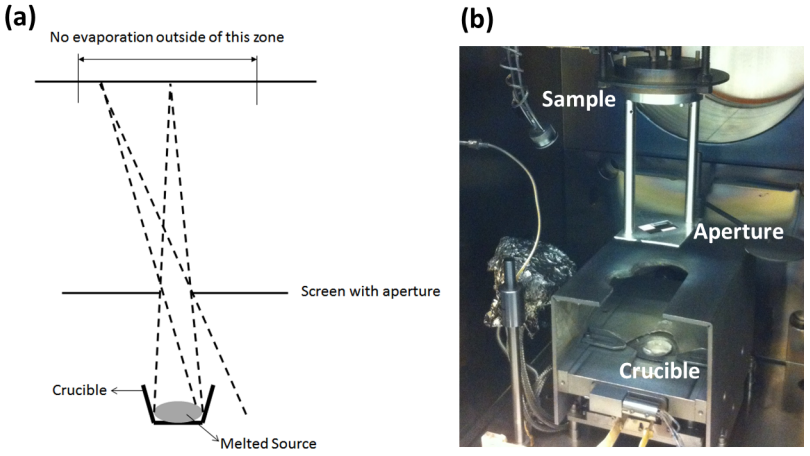

FIGURE 2.21: Schematic (a) and photograph (b) of our evaporator. A rectangular aperture (8 mm) is placed in the evaporation path between the crucible and sample. Ge was deposited onto a gold substrate, creating an amorphous Ge film with a thickness gradient.

We performed three depositions of Al_2O_3 over the top of this sample, each time masking off a portion of it, to create a sample which comprises a continuum of thickness of Ge and several different thicknesses of Al_2O_3. The depositions were performed using a magnetron sputterer with an Al_2O_3 target. A photo of the resulting sample is shown in Fig. 2.22(a), using standard fluorescent ceiling lights for illumination and no additional postprocessing. The thickness of Al_2O_3 was determined using a scanning ellipsometer, assuming $n_{Al2O3} = 1.7$. Note that even the thickest of the Al_2O_3 films is still significantly thinner than a quarter-wavelength across the entire visible spectrum. Fig. 2.22(a) immediately shows all how the deposition of the Al_2O_3 layers affects the optical properties of the Au/Ge coatings. The interference colors in region (i) match those obtained in the previous section, though here the entire gradient of colors possible with this particular configuration is visible. This color gradient persists in all four sections, but the color contrast across the gradient increases significantly for regions (iii) and (iv) compared to region (i) which has no Al_2O_3 coating.

We performed a set of analytical calculations to obtain the theoretical reflectivity and color values corresponding to our fabricated sample. We again utilized the transfer

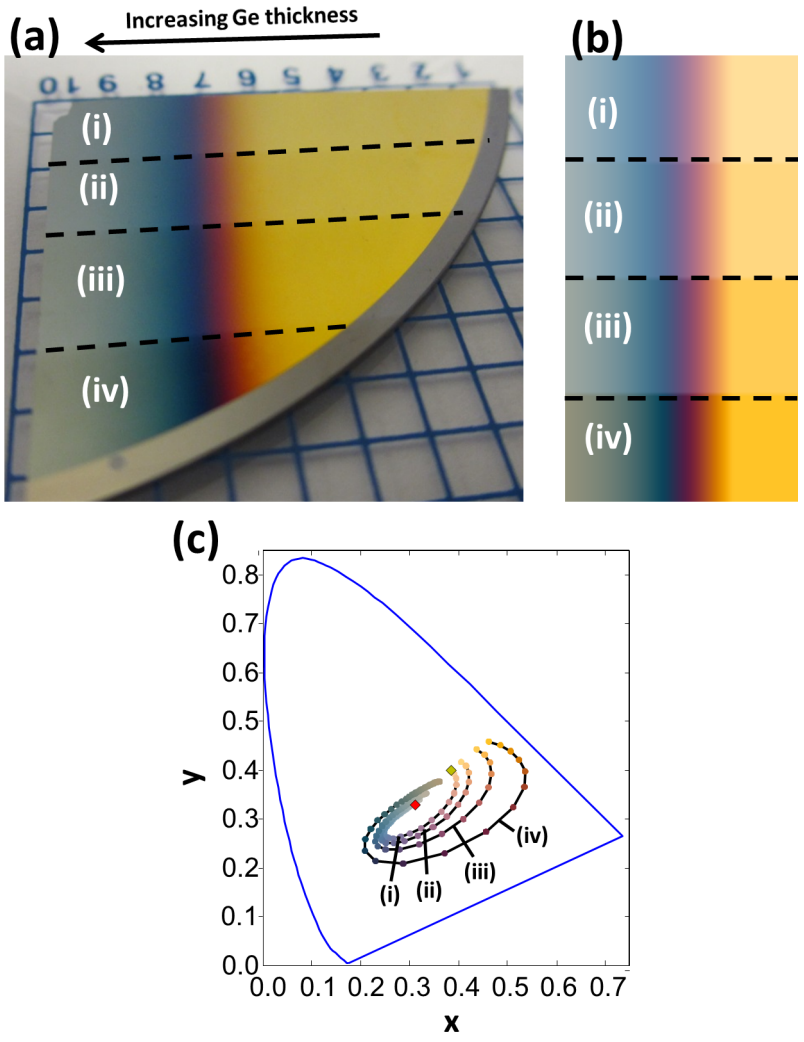

FIGURE 2.22: (a) Photo of the sample comprising optically-thick Au deposited on a silicon wafer, with a film of Ge of gradually varying thickness, overcoated with different layers of Al_2O_3. The four sections (i) - (iv) indicate areas where no Al_2O_3 was deposited, or areas with 14 nm, 28 nm, and 44 nm of Al_2O_3, respectively. (b) Simulated image corresponding to the photo in (a), with the calculated reflectivities of each section obtained using complex refractive index values of Au and Ge obtained by ellipsometry in the previous section and assuming $n_{Al2O3} = 1.7$, and then converted into RGB colors. The calculation was done for unpolarized light at a 30° angle of incidence to match the photograph. (c) Chromaticity diagram corresponding to the image in (b), showing that for increasing Al_2O_3 thickness, the Ge gradient sweeps out a bigger area in the x-y chromaticity space. The four trajectories (i)-(iv) correspond to the four Al_2O_3 thicknesses, and each point corresponds to a certain thickness of Ge. The blue "shark fin" denotes the set of the most "saturated" or "pure" colors that can be defined.

matrix formalism [38] to obtain the angle- and wavelength-dependent reflectivities of the multi-layer geometries, using the complex refractive index values of evaporated Ge and Au as shown in Fig. 2.5. Note that the thicknesses of the Ge and Al_2O_3 films are varying across our sample (Fig. 2.22(a)), so every point on the sample has its own reflectivity spectrum. Following these calculations, we rendered an image that corresponds to the photograph in Fig. 2.22(a).

We used the ColorPy package [39] to convert each reflectivity spectrum into the corresponding standard red-green-blue (RGB) color values. The process involves integrating the reflectivity spectrum with three standard "matching functions" as defined by the International Commission on Illumination in 1931 (CIE 1931), which accounts to the response of the three different photoreceptors in the eye. Using the "D65" standard illuminant, which approximates normal daylight, RGB values for a particular reflectivity spectrum are generated. The generated image is shown in Fig. 2.22(b), oriented so that it corresponds to the photograph in Fig. 2.22(a). This image was generated for a 30° angle of incidence which roughly corresponds to the angle at which the photo in Fig. 2.22(a) was taken, and prior to color rendering the s- and p-polarized spectra were averaged to simulate unpolarized light.

The values obtained from integrating a spectrum with the three CIE 1931 matching functions can be converted into two parameters: "brightness" (or "luminance"), and a two-dimensional "chromaticity" value usually written as (x, y) [40]. The chromaticity value can also be converted into "hue" and "saturation" values. We plotted the generated colors on a chromaticity map shown (Fig. 2.22(c)), where the four curves correspond to the four sections in Fig. 2.22(a, b), and moving along the curve clockwise corresponds to increasing Ge thickness. For increasing Al_2O_3 thickness, the curves cover a larger portion

of the x-y chromaticity space compared to no Al_2O_3, demonstrating quantitatively the increase in color contrast which is apparent from Fig. 2.22(a, b).

To perform a more careful comparison between our experimental and theoretical results, we measured the reflectivity spectrum at various points on the sample. We used an optical microscope with a 5X, 0.15 NA objective and a halogen light illuminate the sample, and used an additional port to confocally collect a portion of the reflected light into a multimode optical fiber (400 μm core), which was then sent to a grating spectrometer (Ocean Optics). The collection spot was 80 μm in diameter, which is much smaller than the spatial extent of our Ge thickness gradient, and therefore we assumed that the thickness change was negligible over the spot. We performed background subtraction and normalization to a flat silver mirror (reflectance $\geq$ 0.95). Given our 0.15 NA objective, the incoming and collected light had a variation of incidence angles from 0° to 8.6°, which we assume to be negligible because of the relatively weak dependence of the reflectivity of ultra-thin films to the angle of incidence (e.g. see Fig. 2.6). The spectra were recorded with a wavelength resolution of approximately 0.35 nm, and the data was smoothed to reduce spectrometer noise. We used an automated, two-axis translation stage to scan across the sample, acquiring spectra at 22 x 40 = 880 points with a spacing of 500 μm along the direction of the gradient and 600 μm along the perpendicular direction.

The experimental spectra are summarized in Fig. 2.23(a-d). Four reflectivity curves are shown per panel, corresponding to no Al_2O_3 film (solid line), and Al_2O_3 films of 14 nm (dashed), 28 nm (dash-dotted), and 44 nm (dotted). Panels (a)-(d) correspond to Ge film thicknesses of approximately 3 nm, 7.5 nm, 12 nm, and 15 nm respectively. These thickness values were determined by comparison to the transfer matrix calculations (Fig. 2.23(e-h)) which are in good agreement with the experiment. The differences between

the regions with different Al_2O_3 films are clear from both the experimental and calculated spectra: the Al_2O_3 layer serves to increase the absorption in the Ge layer, reducing the reflectivity (note that the Al_2O_3 layer itself has negligible optical losses), and this effect becomes stronger with increasing Al_2O_3 thickness. Very thin Al_2O_3 layers do not substantially perturb the reflectivity, and it is likely that sub-10 nm layers will be nearly imperceptible. As the thickness increases, the Al_2O_3 layer begins to operate more and more like an AR coating, even though the thicknesses that we have studied here do not reach a quarter wavelength anywhere in the visible spectrum (at the shortest wavelengths ($\lambda = 450$ nm), the 44 nm Al_2O_3 film corresponds to approximately $\lambda/(6n_{Al2O3})$). Note that because the optical phase shift upon reflection from the Al_2O_3/Ge interface is not π as it would have been if the Ge were lossless, the Al_2O_3 thickness that minimizes reflection is not necessarily $\lambda/(4n_{Al2O3})$, and varies significantly as a function of wavelength because of the large dispersion of Ge and the underlying Au. Our calculations show that a thickness of roughly $\lambda/(5n_{Al2O3})$ to $\lambda/(7n_{Al2O3})$ is needed to minimize the reflectivity at various wavelengths within the visible range.

In summary, understanding the effect of additional transparent layers deposited over these coatings is important, because such layers can be used as protection against chemical or physical erosion or as transparent electrical contacts for optoelectronic devices. In this section, we showed that depositing transparent layers of alumina on top of ultrathin coatings comprising gold and germanium can enhance the optical absorption as well as the color range that can be attained.

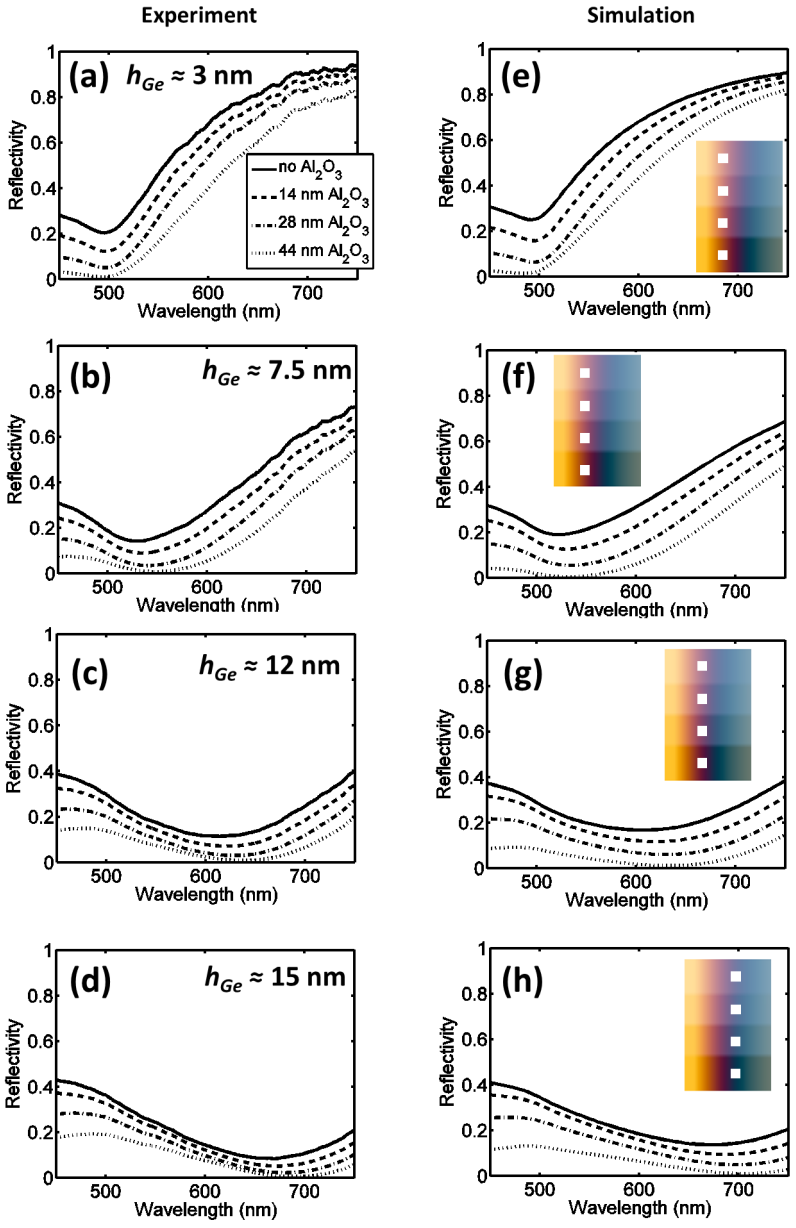

FIGURE 2.23: Measured (a-d) and calculated (e-h) reflectivity spectra for normal incidence at positions on the sample corresponding to four different values of Ge thickness (approximately 3 nm, 7.5 nm, 12 nm, and 15 nm, respectively) and four different values of Al_2O_3 thickness (0, solid line; 14 nm, dashed; 28 nm, dash-dotted; 44 nm, dotted). The insets of (e-h) are a calculated image of the sample corresponding to the image in Fig. 2.22(b), except calculated for normal incidence instead of a 30° incidence angle (as in Fig. 2.22(b)). The white squares in the insets indicate the positions where the four reflectivity curves are calculated. The approximate thickness of the Ge film at these locations are shown in the insets of (a-d). Note that because the gold films are opaque, the reflectivity $R = 1 - A$, where A is the absorptivity.

2.4 Tunable ultra-thin perfect absorber

One particularly convenient attribute of classical electromagnetism is that Maxwell's equations are scale invariant; that is, any structure will have the same optical properties when illuminated by light with wavelength λ as the same structure scaled up or down by a factor N when illuminated by light with wavelength $N\lambda$, assuming that the complex refractive indices of the constituent materials remain the same. As a result, concepts developed for one frequency range are frequently applicable to another. In fact, one fruitful area of research over the last decade involves implementing existing concepts from radio and microwave frequencies (or at least using them as an inspiration) to develop new optical and optoelectronic devices at optical frequencies (e.g. see the next chapter for optical frequency devices based on antennas, a concept that has been primarily explored for much lower frequencies).

In the previous sections we focused on ultra-thin, highly-absorbing optical coatings in the visible regime. In the following, we will apply the same optical principles to the mid-infrared spectral range, which requires new materials (unlike Maxwell's equations, material properties are not frequency-invariant) but opens up new opportunities. In particular, we will focus on obtaining a thin film absorber which can be switched from a high reflectance (and low absorbance state), to a low reflectance (high absorbance) state.

2.4.1 Resonant cavity enhanced processes and critical coupling

In optics, resonant optical cavity configurations have been used for detectors and modulators to achieve enhanced absorption at selected wavelengths and a high on-off ratio, respectively. The design of such devices benefits from critical coupling, a phenomenon

which facilitates efficient power transfer to a resonator, which occurs when the internal losses of a resonant cavity are equal to the mirror losses, i.e. due to light escaping from the device facets [26]. One implementation of this concept is the asymmetric Fabry-Perot (FP) cavity in which the dielectric forming the cavity is typically at least a quarter-wave in thickness and is surrounded by mirrors with unequal reflectivities, in which the back reflector is often a Bragg mirror [12][41][13][27][42][43]. This geometry has been used for reflection modulators [12][27][42], for resonant-cavity enhanced (RCE) photodetectors [41][13] and for enabling strong coupling between light and matter [43]. More recently, the concept of critical coupling has been reformulated in terms of the time reversal of lasing at threshold or "coherent perfect absorption" [44][45][46]. Another example of critically-coupled resonators is the class of perfect absorbers comprising plasmonic nanostructures, which have been demonstrated over a wide range of frequencies, with typical experimental absorption values of approximately 90% [47][48][49][50] and reaching as high as 99% [51]. Unlike the asymmetric FPs, these nanostructured devices are very thin compared to the wavelength of light, but have complex nanofabrication requirements which may limit practical device applications. It is sometimes assumed that perfect absorbers based on dielectric cavities cannot be made much thinner than the operating wavelength, and that plasmonic nanostructures are required to overcome this limitation [46].

2.4.2 VO_2/sapphire perfect absorber concept

In this section, we demonstrate a perfect absorber comprising an unpatterned, ultra-thin (approximately $\lambda/65$) film of vanadium dioxide (VO_2) on an sapphire substrate. By utilizing an intermediate state of the insulator-metal phase transition (IMT) in VO_2 which exhibits multiple co-existing phases, an effective medium with tunable optical properties

is formed. In particular, the absorption coefficient can be very large in proximity to the IMT. We show that thermal control of the phase co-existence in the VO_2 film enables switching of the absorption from about 20% to 99.75% at $\lambda = 11.6$ μm. The absorption in our device is greatly enhanced via critical coupling to a cavity resonance which is shown to exist when the ultra-thin film has a large imaginary part of the refractive index. Our device combines the deep-subwavelength thickness characteristic of nanostructure-based perfect absorbers with the wide tuning capability typical of asymmetric FP cavities, while comprising only a single film deposited on a reflecting substrate.

As in the section 2.2, we consider light incident from air ($n_1 = 1$) onto a dielectric film with complex refractive index $n_2 + ik_2$, deposited on a substrate with index $n_3 + ik_3$ (Fig. 2.24(a)). The reflection can be calculated as the coherent sum of the partial waves reflected from the first interface (with reflection coefficient r_0) and those reflected from the cavity after 1, 2, ..., m roundtrips with reflection coefficients r_1, r_2, $\ldots r_m$. Eqn. 2.1 describes the reflectivity from this structure just as it did in the previous sections.

When $k_2 << n_2$ (0 in the case of the conventional AR coating), this a simple asymmetric FP cavity. On resonance, light is stored for many optical cycles. If there are some losses present, light is gradually absorbed as it circulates; most FP modulators and RCE detectors operate in this manner. This is illustrated in Fig. 2.24(a), with a dielectric film deposited on a higher index substrate. In the partial wave picture, the first reflection r_0 has a phase shift of π with respect to the incident wave and thus the corresponding phasor points to the left, along the real axis in the complex plane (Fig. 2.24(b)). The front facet reflection can be cancelled out if the partial waves emerging from the film each have a phase shift of 0 and the phasor trajectory terminates at the origin; this occurs when the thickness h of the dielectric is an odd integer multiple of $\lambda/4n$ and the reflectivity $|r_{12}|^2$ is equal to the effective bottom mirror reflectivity $\left|r_{23}e^{2i\beta}\right|^2$, as can be

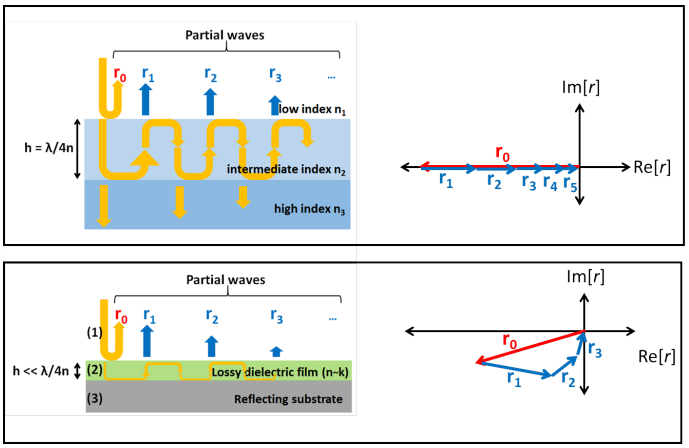

FIGURE 2.24: (a) The reflection process from a quarter-wave film on a high index substrate at normal incidence, showing the partial waves. Many multiple reflections are involved. (b) Phasor addition diagram (the reflected partial waves are represented in the complex plane) demonstrating that a properly-engineered quarter wave film on a high index substrate can result in zero reflection via destructive interference. The phase of the first partial wave r_0 is π with respect to the incident wave, but the phase of all of the other partial waves is 0. (c) Reflection process from a highly-absorbing (k_2 of the same order as n_2), ultra-thin film. (d) Phasor diagram demonstrating that a zero-reflection (and hence perfect absorption) condition is achievable if the complex refractive index of the film has a large imaginary component. In this case, the phase of r_0 deviates significantly from π (the phasor is not along the horizontal axis) and a small number of reflections is sufficient to cancel r_0 and maximize absorption.

seen from Eqn. 2.1 [27]. These arguments also persist if the substrate is reflecting, in which case some absorption (either in the substrate upon reflection or in the film) is required if a minimum in reflectivity is to be achieved. Even if the substrate is a PEC, with the proper value of k_2 the reflectivity can go to zero, indicating perfect absorption in the film.

The phasor diagram in Fig. 2.24(d) suggests another route to achieving the perfect absorption condition, as previously shown in Section 2.2.4. The exact phasor trajectory does not matter as it returns to the origin. One of the possible trajectories in which the phase of r_0 is not π is shown in Fig. 2.24(d). The interface reflection phase shifts become substantially different from 0 and π when at least one of the materials has k comparable to n. As a result a resonance can exist for a film that is much thinner than the wavelength of light, and critical coupling to this ultra-thin resonance yields a perfectly absorbing state (Fig. 2.24(c)). Our perfect absorber utilizes this condition

to enhance absorption, using the intermediate state in the insulator-to-metal transition (IMT) in VO_2 to introduce a large, controllable degree of loss.

VO_2 is a correlated oxide that undergoes a thermally triggered IMT near room temperature ($T_c \sim 340K$), which takes the material from an insulating state (band gap of about 0.6 eV) to a metallic one. The IMT occurs gradually as the temperature is increased: nanoscale islands of the metallic phase emerge in the surrounding insulating VO_2, which then grow and connect in a percolation process, leading to a fully metallic state where the band gap has collapsed [52][53][54]. This metal-dielectric phase coexistence within the phase transition results in widely-tunable optical properties; in fact the naturally occurring nanoscale structures in the IMT region can be viewed as a reconfigurable disordered metamaterial. The IMT has been utilized for optical switching [55][56], and has enabled several tunable devices comprising metallic nanostructures on VO_2 films [57][58][59]. VO_2 is also the target of active research for the realization of novel electronic switching devices that may complement MOSFET technology [54].

In general, probing the physics of this intermediate state is still in infancy because the material quality of VO_2 films has only recently been improved to the point where a complex region such as the intermediate state of the phase transition can be explored with reproducibility. The IMT in this material has been known for over 50 years, however bulk crystals often crack during the transition due to stress (as is often the case for brittle ceramics) [60]. Thin film structures can be made more robust to the stress relaxation caused by substrate clamping; however careful thermal profiles composition control are required to obtain reversible transition properties [61][62]. Studies on thin film VO_2 with reproducible phase transition properties can be considered an emerging field and within that, the intermediate state (i. e. a mixture of metallic and insulating states) is now being recognized as an opportunity, especially given recent interest in

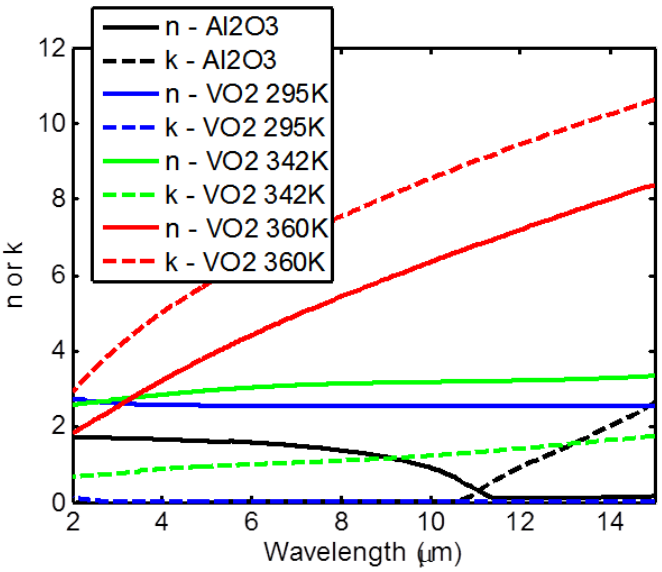

FIGURE 2.25: Complex refractive indices for sapphire and VO_2 in the metallic (red), insulating (blue), and intermediate (green) states, taken from Refs. [64] and [52].

metamaterials which often require composite structures comprising domains of sub-wavelength dimensions with vastly different optical properties [63].

To implement an absorber that can be tuned between low and perfect absorption states, we deposited a crystalline film of VO_2 with a thickness of 180 nm on a c-plane sapphire substrate. The VO_2 thin film was grown on a single-side-polished c-plane sapphire substrate (1 mm thick) using magnetron sputtering from a vanadium pentoxide (V_2O_5) target at 550°C under 10 mTorr pressure with 100 sccm argon (Ar) gas flow rate at a power of 120 W. The thickness was checked with a scanning electron microscope (SEM) after milling a cross-section with focused ion beam (FIB). For reference, literature values for the complex refractive indices of VO_2 and sapphire in the infrared are plotted in Fig. 2.25.

The absorption was investigated via normal incidence measurements using a Fourier transform infrared (FTIR) spectrometer and mid-IR microscope (Fig. 2.26(a)). The reflection spectrum was collected while gradually increasing the sample temperature from 297 K to 360 K at 1 K increments (Fig. 2.26(b)). The sample was mounted

on a temperature controlled stage (Bruker Optics A599) inside a mid-infrared (MIR) microscope (Bruker Optics Hyperion 2000). A reflective objective (15X, NA = 0.4) was used to focus an unpolarized beam from a MIR Globar source mounted in an Fourier transform infrared (FTIR) spectrometer (Bruker Optics Vertex 70) onto the sample from the VO_2 side, with the reflected light collected by the same objective and sent to a liquid nitrogen-cooled mercury-cadmium-telluride (MCT) detector. To normalize the reflectance spectra, a reference spectrum was taken in transmission mode utilizing a second identical objective to collect the light.

The 297 K curve is representative of the reflection spectrum at a temperature significantly below T_C. Since insulating VO_2 is transparent at photon energies below the band-gap, the primary features of the room temperature reflection spectrum are due to the underlying sapphire. Sapphire is highly absorptive at $\lambda \approx 5$ - 10 μm despite its large band gap in due to the presence of several phonon modes [53][18], which also result in high reflectivity between 10 and 15 μm. The VO_2 thickness is much smaller than the wavelength of the incident light, so no FP fringes are observed. The small features at approximately 3 μm, 4.5 μm, and 6 μm correspond to ambient atmospheric absorption. At high temperatures (e.g. 360 K curve in Fig. 2.26(b)), the VO_2 is entirely in the metallic phase, and displays relatively high reflectivity which slowly increases with increasing wavelength, as expected for a Drude-like metal.

The reflectivity spectrum does not transition monotonically from that of the low-temperature state to that of the high-temperature one due to the complex interplay between the effective medium formed when the VO_2 is in an intermediate state and the underlying sapphire substrate. In particular, we focus on the feature at $\lambda \approx 11.6\mu$ m (vertical dashed line in Fig. 2.26(b)); at this wavelength, the reflectivity is approximately 0.7 with the VO_2 in the insulating state (at room temperature) due to the high reflectivity of the

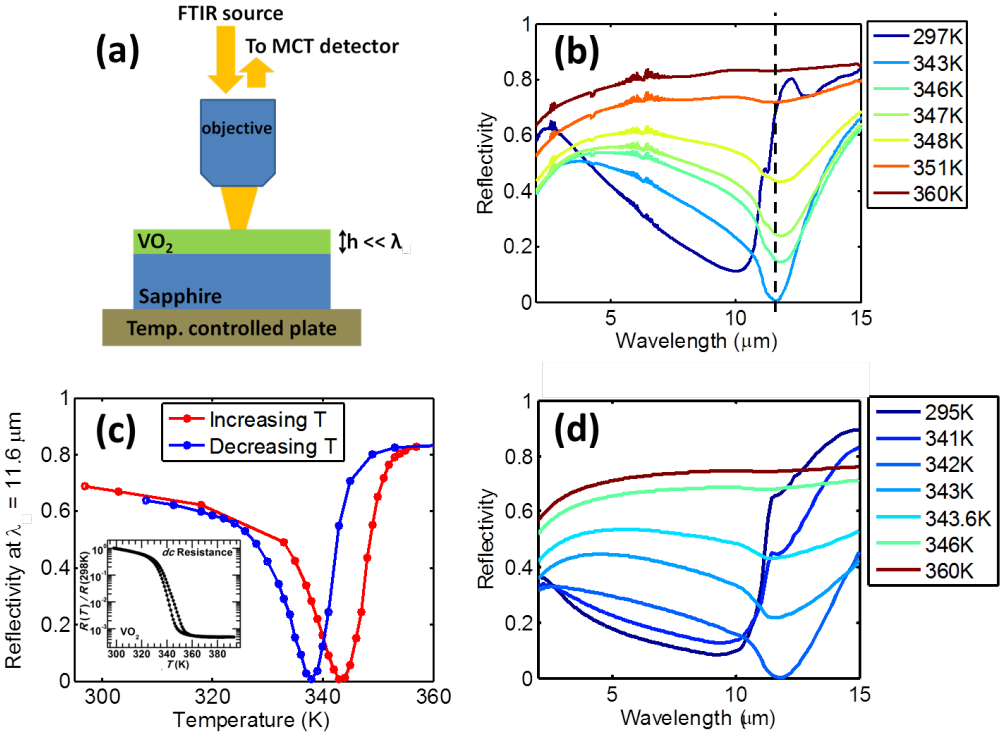

FIGURE 2.26: (a) Experimental setup. A sapphire substrate coated with $h = 180$ nm of VO_2 is placed on a temperature-controlled stage mounted inside an infrared microscope and illuminated at normal incidence using a mid-IR source. A mercury-cadmium-telluride (MCT) detector is used to collect the reflected light. (b) Experimental reflectivity spectrum at temperatures from 297 K to 360 K. At 343 K, the reflectivity drops to approximately 0.0025 at $\lambda = 11.6\mu$m, indicated by the vertical dashed line. (c) Experimental reflectivity from the sample at $\lambda = 11.6\mu$m as a function of increasing (red) and then decreasing (blue) temperature. A 5 K hysteresis is seen in the reflectivity. Inset: Normalized *dc* resistance of the VO_2 thin film sample as a function of temperature showing nearly four orders of magnitude of change in the resistance and hysteretic behavior. (d) Calculated reflectivity spectrum at temperatures from 295 K to 360 K using experimental values for the complex refractive indices of VO_2 [52] and sapphire [64]. The reflectivity of bare sapphire is shown in black.

underlying sapphire, and approximately 0.8 with the VO_2 in the metallic state (T = 360 K). At T = 343 K, however, the reflectivity abruptly drops to approximately 0.0025, corresponding to a reduction by a factor ≈ 280 with respect to the low-temperature insulating state and by a factor ≈ 320 with respect to the high-temperature metallic state. Since the sapphire substrate is opaque at this wavelength, this corresponds to a 99.75% absorbance within the VO_2 film and the top part of the substrate (1-2 μm), as discussed later in the text. For reference, we replotted Fig. 2.26(b) in Fig. 2.27,

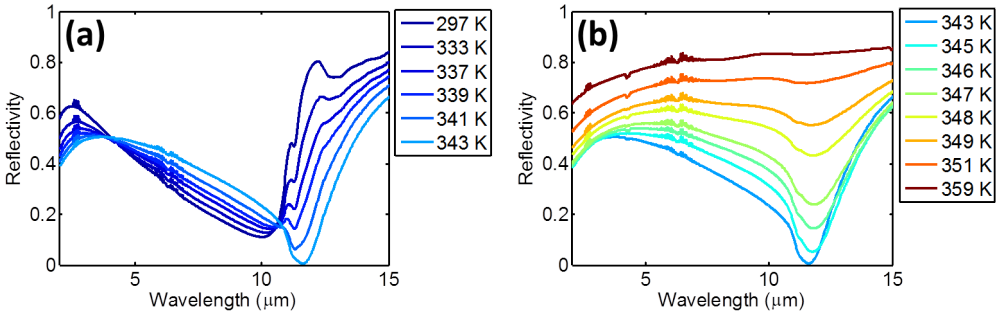

FIGURE 2.27: Detailed plots of them measured reflectance of the VO2/sapphire sample for increasing temperature. These figures separate out Fig. 2.26(b) so that it is easier to read.

breaking up the curves so that the figure is easier to read. The reflectivity spectrum has a hysteresis of approximately 5 K (Fig. 2.26(c)), comparable to the *dc* resistance hysteresis width of the VO_2 film (inset of Fig. 2.26(c)). The normalized *dc* resistance $R(T)/R(298\text{ K})$ exhibits a change of more than three orders of magnitude between 298 K and 393 K.

To obtain the theoretical reflectivity of our device, we used Eqn. 2.1 with the temperature-dependent complex refractive index for VO_2 (for increasing temperature) experimentally obtained by ellipsometry in Ref. [52], and the index for sapphire from Ref. [64]. The calculated spectra match well with the experimental data across the entire $\lambda = 2$ - 15 μm range (Fig. 2.26(b, d)), though the temperatures at which the various spectral features occur differ by 2 - 5 degrees. We attribute the latter to the differences in the growth conditions and film thicknesses between our VO_2 sample and the one measured in (Ref. [52]) [65]. The predicted reflectivity minimum is 0.0007 at $\lambda = 11.75\mu$m and $T \approx 342$ K, compared to the experimental data which showed a minimum value of approximately 0.0025 at $\lambda = 11.6\mu$m and T = 343 K.

As in Section 2.2.4, we performed a set of calculations in which the VO_2 film was replaced with an unknown homogeneous dielectric of the same thickness, assuming only that it has some complex refractive index $\tilde{n} = n + ik$. In Fig. 2.28, we plotted the calculated

reflectivity using Eqn. (2.1) at $\lambda = 11.75$ μm as a function of n and k, covering a wide range of potential values of $\tilde{n}$ for the material comprising the thin film. The complex index of sapphire at this wavelength was taken to be about 0.1 + 0.8i [64]. We found that for $\tilde{n} \cong 3.25 + 1.5i$, the calculated reflectivity drops to zero indicating critical coupling, with approximately 90% of the light absorbed in the 180 nm film and the remaining 10% absorbed in the top layer (1-2μm) of the underlying sapphire. This reflectivity minimum is very broad in $n-k$ space, making the phenomenon very robust; as a result, small changes in the composition (and hence $\tilde{n}$) of the lossy dielectric will not significant impact device performance. The spectral width of the absorption minimum at the perfect absorption condition (≈ 3 μm full-width half-max) is determined primarily by the dispersion of the materials comprising the absorbing layer and the underlying substrate.

As shown in Fig. 2.24(c, d), the complex values of the refractive indices lead to non-trivial reflection phase shifts (e.g. approximately 0.08π for the VO_2/air interface and -0.02π for VO_2/sapphire at λ 11.75 μm) and substantial absorption as light propagates through the lossy film. As a result of these high losses, all of the incident light is absorbed after only a few passes through the thin film; $R = |r|^2$already reaches about 0.0006 after including just the m = {0, 1, 2, 3}terms in Eqn. 2.1.

Critical coupling to a cavity consisting of an ultra-thin absorptive film, a dielectric spacer, and a quarter-wave stack reflector has been previously shown [43], to our knowledge it has not been demonstrated for a resonator formed by an ultra-thin layer absorbing layer on an opaque substrate. We additionally note that a distinct but related condition for maximizing absorption has been recently theoretically proposed for a vanishingly-thin film with $n \approx k$ embedded between two lossless dielectrics [66][67][68].

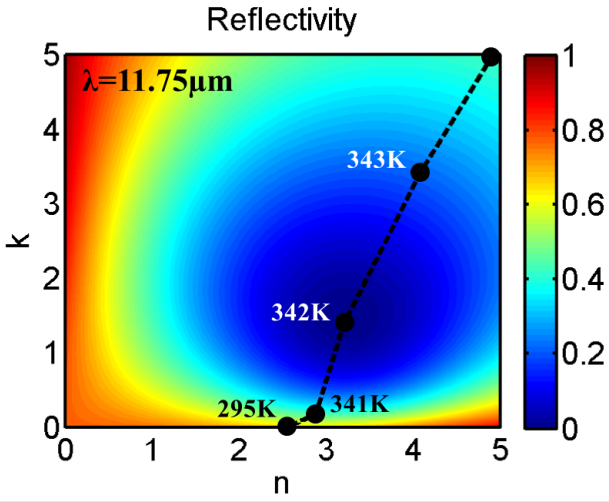

FIGURE 2.28: (a) Map of the calculated reflectivity as a function of n and k, the real and imaginary parts of the complex refractive index $\tilde{n}$, of a uniform dielectric film of 180 nm thickness on sapphire for $\lambda = 11.75\mu$ m. The reflectivity drops to zero for $\tilde{n} \cong 3.25 + 1.5i$. The black dashed line marks the trajectory of the complex refractive index of VO_2 with increasing temperature. The VO_2 index passes very close to the minimum reflectivity point in n-k parameter space (black dashed line).

Thermally tuning the phase co-existence in VO_2 is equivalent to tracing out a path in n-k space; this trajectory is plotted as a function of temperature in Fig. 3 (black curve) using the data from Ref. [52]. We observe that at T $\approx$ 342 K, the index of VO_2 passes almost exactly through the point of low reflectivity, confirming our experimental data. The phase transition in VO_2 results in a very large change in its optical properties, enabling a change in device reflectivity on the order of unity.

Calculations show that the spectral position of the absorption maximum can be tailored over a significant portion of the 8 μm - 14 μm atmospheric transparency window by changing the VO_2 film thickness, making this geometry potentially useful for infrared detection and imaging applications. The calculated absorption maximum occurs at $\lambda \approx 10.5$ μm for a 20 nm VO_2 film on sapphire, and can be continuously red-shifted with increasing VO_2 thickness; for example, at $h = 400$ nm the dip is predicted to be at $\lambda \approx 13.3$ μm with R ≈ 0.09.

We also explore the behavior of our perfect absorber given oblique incident light. We

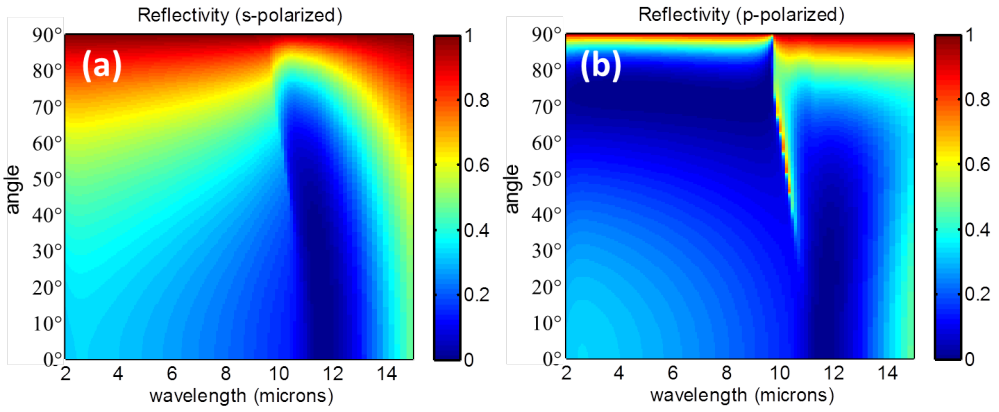

FIGURE 2.29: Calculated reflection spectra from the 180 nm VO_2 film on sapphire (T = 342 K) for (a) s-polarized and (b) p-polarized incident light at various angles of incidence

used Eqn. 2.1 to calculate the reflection spectra of our structure using the index for VO_2 at T = 342 K for various angles of incidence for s- and p-polarized light (Fig. 2.29(a) and (b), respectively). Very low reflectivity and high absorption values are observed over a broad range of angles around our wavelength of interest (≈ 11.75 μm). Our calculations show that the reflectivity remains under 0.01 for incident angles of 0° to 30° for both s- and p-polarization. This low sensitivity to incident angle is a result of the small propagation distance for light inside the VO_2 film. We note that in our experiment, the numerical aperture (NA) of the objective is 0.4 (corresponding to an acceptance angle of approximately 24°), which is the likely source of the discrepancy between the calculated and measured reflection minima (0.0007 and 0.0025, respectively).

2.4.3 Potential applications of the VO_2 perfect absorber

Thermal imagers are of increasing importance in numerous applications, from hyperspectral imaging to surveillance and medical devices. There is a need to reduce the size of photodiode-based imagers, increase their pixel count, and operate them at non-cryogenic temperatures. Modern uncooled microbolometers generally rely on detecting small changes in the electrical resistance of materials whose electric properties vary as

a function of temperature. Devices relying on thermal variations of electrical resistance are essentially thermistors [69].

VO_2 has long been investigated for applications in bolometers using the IMT [70], though this approach is complex due to the presence of hysteresis [71]. Nonetheless, various vanadium oxides (usually mixed valence VO_x) are widely used for commercial bolometers at temperatures away from the IMT (e.g. [72]). Recently, however, a bolometer based on newly-discovered non-hysteretic behavior within the transition region has been proposed [71], which may increase the temperature coefficient of resistance, leading to enhanced detectivity. Combining this approach with the perfect absorber geometry demonstrated in the present work could result in significantly improved infrared detection and imaging, especially if a dopant is used to decrease the transition temperature of VO_2 [65].

In order to extend the absorber concept demonstrated here to other spectral ranges, alternate materials for either the substrate or the ultra-thin film can be used. VO_2 films, for example, can be grown on a number of substrates such as glass, silicon, germanium, titanium oxide and indium-tin-oxide (ITO) [54][73]. In general, tunable highly-absorptive layers can be created using a variety of correlated oxides which exhibit phase co-existence in the vicinity of phase transitions [54] as well as other phase change materials [74].

The absorber demonstrated here requires no nanofabrication steps beyond deposition of the VO_2 film, and thus can easily be made to cover a large area. The IMT in VO_2 is known to occur on a picosecond timescale and can be triggered thermally, optically, or electrically [54], making VO_2-based components promising for future optoelectronic devices including optical switches and modulators.

2.5 Anomalous thermal emitter

Thermal radiation is light that is emitted by an object at a temperature above absolute zero. The spectrum and intensity of thermal radiation emitted by an object is a function of its temperature and emissivity, which is in general frequency (f) dependent. This is expressed by:

$$I(K,T) = 2hc\frac{K^3}{e^{hcK/k_BT}-1}\varepsilon(K) \tag{2.2}$$

where I is the spectral radiance (or the spectral radiant energy density), $K = f/c$ is the spectroscopic wavenumber, T is the temperature expressed in Kelvin, h is Planck's constant, c is the speed of light in vacuum, k_b is the Boltzmann constant, and $\varepsilon(K)$ is the frequency-dependent emissivity [75]. More specifically, the spectral radiance is the radiant power emitted from a unit area of the source per unit solid angle, in the wavenumber interval from K *to* $K + dK$, and has units of W cm^{-1}. The factor in front of $\varepsilon(K)$ in Eqn. 2.2 is known as Planck's law, and describes blackbody emission. For most objects, $\varepsilon(K)$ is largely independent of temperature (or other external variables such as applied fields).

There is substantial interest in engineering $\varepsilon(K)$for applications ranging from incandescent light sources [76] to heat management [77][78][79] to thermal tagging and imaging [80]. In determining $\varepsilon(K)$ for various materials and structures, frequent use is made of Kirchhoff's law of thermal radiation which states that the emissivity of an object $\varepsilon(K)$ is equal to its frequency-dependent absorptivity $a(K)$ [75].

One approach to engineering $\varepsilon(K)$ has been to select materials with appropriate material dispersion to achieve selective thermal emission [81]. A complementary approach

involves surface texturing, either disordered [76] or highly ordered in the case of gratings [82] or photonic crystals [83]. Similarly, photonic cavities can enhance or suppress thermal emission [84] [85]. More recently, optical antennas [86] and metamaterials [87] have also been employed to tailor the directionality and spectrum of thermal emission.

In addition to these static schemes, certain tunable materials can be employed to dynamically manipulate$\varepsilon(K)$. Of particular interest are electrochromic materials such as tungsten oxide (WO_3), which undergoes significant change in optical and infrared properties under an applied voltage, and can therefore be used to modulate emissivity of thermal radiators for applications such as temperature control of satellites by radiative cooling [77][78].

Modulation of the emissivity can also be achieved by using thermochromic materials, whose optical properties are temperature-dependent. Unlike in the case of electrochromic materials, a change in temperature can simultaneously alter the emissivity $\varepsilon(K,T)$ of the object incorporating a thermochromic material, and the blackbody contribution to the spectral radiance $K^3/(e^{hcK/k_BT}-1)$ (see Eqn. 2.2). A potential benefit of tuning based on thermochromic materials is that it allows for passive "smart" devices that can operate without the need for external power or controls. For example a radiator that has low emissivity at low temperatures and high emissivity at high temperatures can help keep heat in when cold and radiate heat away faster when hot, making it useful for passively maintaining a desired temperature [79].

As discussed in the previous section, vanadium dioxide (VO_2) is a thermochromic material and, as with absorptivity and reflectivity, present literature on tuning an object's thermal emissivity using VO_2 has largely focused on the considerable change of infrared

optical properties between the extreme states of the phase transition – fully insulating, and fully metallic [79][88][89][90][91]. However, as we showed previously, very rich physics can be found within the transition region itself, which can be harnessed to obtain additional control over thermal emission properties.

In this section, we show that a geometry comprising a thin film of VO_2 on a sapphire substrate like the one in the previous section can exhibit "perfect" blackbody-like emissivity (nearly 1) over a narrow range of frequencies when the VO_2 is in its transitional state and operates as a natural, tunable metamaterial, i.e. an effective medium with widely-tunable infrared optical properties. As a result of this resonance in emissivity, the sample displays substantial broadband negative differential thermal emittance; i.e. as the sample is heated the thermal emission decreases.

In VO_2 thin films, the IMT occurs gradually with increasing temperature: nanoscale inclusions of the metallic phase emerge in the surrounding insulating-phase VO_2, which grow and connect in a percolation process, eventually leading to a fully metallic state at the end of the transition [53][52]. These metallic inclusions are much smaller than the scale of the wavelength at infrared frequencies, and thus VO_2 can be viewed as a natural, reconfigurable, disordered metamaterial with variable effective optical properties across the phase transition. In the previous section, we utilized this unique temperature-dependent dispersion of the effective medium to demonstrate that a film of VO_2 with thickness much smaller than the wavelength deposited on sapphire can operate as a temperature-tunable absorber; in particular, nearly-perfect absorption was achieved at a particular temperature for a narrow range of infrared wavelengths. The reflectivity of such a device varies dramatically and non-monotonically across the phase transition, with the strong absorption feature appearing during an intermediate state of VO_2 as a result of critical coupling to an "ultra-thin-film resonance". Since $\varepsilon(K) = a(K)$, such a

thin-film VO_2 / sapphire structure is expected to have an emissivity ε(K, T) that also depends strongly and non-monotonically on temperature.

For this experiment, our sample consisted of an epitaxial VO_2 film of approximately 150 nm in thickness, grown on a polished single crystal c-plane sapphire by RF-magnetron sputtering with a V_2O_5 target (99.9% purity, AJA International Inc.). During film growth, the substrate temperature and RF source gun power were kept constant at 550 °C and 125 W respectively. A mixture of 99.50 sccm Ar and 0.50 sccm O_2 was used as the sputtering gas, maintaining the total pressure at 10 mTorr.

We measured the thermal emission from our VO_2/sapphire sample by mounting it on a temperature-controlled stage, changing the temperature from 40 °C to 100 °C and back down (resolution of 0.5 °in the range of 55 °C – 85 °C and 5 °outside of that, waiting at least 60 seconds to allow the temperature to settle), and directly sending the emitted light into a nitrogen-purged Fourier transform infrared (FTIR) spectrometer (Bruker Vertex 70) equipped with a room temperature DTGS detector (Fig. 2.30). As a reference, we replaced the sample with black soot [75], deposited onto a gold-coated silicon wafer using a candle (deposition time >10 minutes). After deposition, the soot-coated wafer was baked at 200°C for 30 minutes to remove any excess paraffin from the candle. At moderate temperatures, candle-deposited soot is expected to have a wavelength-independent emissivity ε between 0.95 and 0.98 in the infrared [92][93][94]; for this work, we assume $\varepsilon = 0.96$. Mid-infrared reflectance measurements taken using a microscope (Bruker Hyperion 2000, NA = 0.4, 15X objective) confirmed that the soot sample is a good blackbody reference (reflectance <0.01 with some light presumed to be scattered; data not shown).

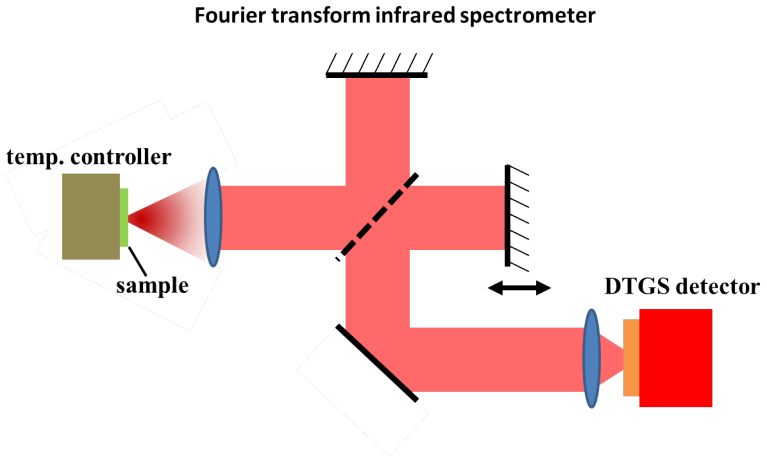

FIGURE 2.30: Experimental setup. The VO_2/sapphire sample is mounted on a temperature-controlled stage, and the thermal emission is sent into an FTIR spectrometer equipped with a DTGS detector.

To obtain an accurate emission spectrum, we had to correct for the wavenumber-dependent response of the optics of the FTIR spectrometer and the detector and also account for the thermal emission from sources other than our sample [75][95]. In particular, both the detector and the optical components of the FTIR (the beamsplitter, mirrors, etc) are all at room temperature, and all emit thermal radiation. Accounting for these becomes more complicated in our case compared to more conventional emittance measurements because our sample is partially reflective, and the reflectivity changes significantly as a function of temperature which affects how much of the thermal radiation emitted by the detector returns back to the detector.

A particular temperature-dependent measured spectrum $S(K,T)$can be broken down as

$$S(K,T) = m(K,T)[I(K,T) + b_{instr}(K) - (1 - R(K,T))b_{det}(K)] \tag{2.3}$$

where$I(K,T)$ is the actual spectral radiance of the sample, $m(K,T)$ is the instrument response transfer function including the effects of atmospheric absorption along the light path between the sample and the detector, $b_{instr}(K)$ is the thermal contribution of the instrument including emission from the optics and the walls of the FTIR spectrometer

(but not from the detector), $b_{det}(K)$ is the thermal emission from the detector, and $R(K,T)$ is the reflectivity of the sample which can be temperature-dependent for thermochromic materials. In our measurement, we assume that $b_{instr}(K) = 0$ because our DTGS detector is at the same temperature as the rest of the instrument, so there is no net flow of thermal radiation between the detector and the optics and walls. There is substantial radiation from the detector itself, so $b_{det}(K)$ cannot be neglected, and a portion of this radiation that enters the interferometer and reaches the sample is reflected back toward the detector; this is accounted for by the $(1 - R(K,T))$ term in Eqn. 2.3.

Because both our black soot reference and VO_2/sapphire sample are opaque within the wavelength range of interest (within the 5-15 μm range, sapphire is opaque as a result of multiple phonon resonances which are present [7][18]), we can write the emissivity as$\varepsilon(K,T) = a(K,T) = 1 - R(K,T)$, which simplifies Eqn. (2.3) to

$$S(K,T) = m(K,T)\varepsilon(K,T)[I_{BB}(K,T) - b_{det}(K)] \tag{2.4}$$

where $I_{BB}(K,T)$ is the thermal radiation spectrum from a perfect blackbody. Note that it is important to select the appropriate units when representing the Planck distribution function $I_{BB}(K,T)$ as the expressions differ depending on which units are used, e.g. wavenumber or wavelength. Since an FTIR yields spectra with constant resolution in wavenumber [75], we choose to use wavenumber units (which are equivalent to frequency units since $K = f/c$).

Given a reference sample with a known emissivity such as the black soot, one can calculate $m(K,T)$ and $b_{det}(K)$ by measuring the emitted spectrum at two different temperatures T_1 and T_2, and solving the system of two equations. In our measurement, however, this is unnecessary because $\varepsilon(K,T)$ is factored out in Eqn. (2.4). Instead we

can note that given the measured spectra $S_{sample}(K,T)$ and $S_{ref}(K,T)$ from our sample and reference, respectively, and knowledge of the reference emissivity $\varepsilon_{ref}(K,T)$, we can immediately obtain $\varepsilon_{sample}(K,T)$ by

$$\frac{S_{sample}(K,T)}{S_{ref}(K,T)} = \frac{\varepsilon_{sample}(K,T)}{\varepsilon_{ref}(K,T)}. \tag{2.5}$$

This analysis method is applicable only to samples that are smooth (any roughness must be on a substantially smaller scale than the wavelength of emitted light), which is the case for our VO_2/sapphire sample. For rough samples, not all of the light emitted by the detector will be specularly reflected from the sample, and instead some thermal emission from the surrounding area may be scattered into the beam path by the sample; in this case extra care must be taken during data analysis.

We used Eqn. 2.5 to determine the experimental emissivity of our VO_2/sapphire sample, which is plotted for increasing temperatures in Fig. 2.31(a, b). From the experimental emissivity, we calculated the spectral radiance $I(K,T) = \varepsilon(K,T)I_{BB}(K,T)$ of our black soot reference and the VO_2/sapphire sample, shown in Fig. 2.31(c) for three different temperatures. It can be directly observed that while the thermal emission from the black soot reference is monotonically increasing with increasing temperature, the emission from the VO_2/sapphire sample first increases and then decreases. At a particular temperature (approximately 74.5 °C) and wavelength (approximately 864 cm^{-1}), the emissivity approaches unity (Fig. 2.31), indicating that at that wavelength the sample displays nearly "perfect" blackbody-like emission, corresponding to the "perfect absorption" condition. The peak in infrared emissivity is relatively broadband (about 200 cm^{-1}), with the emissivity surpassing that of the black soot reference between 840 cm^{-1} and 885 cm^{-1}. The emissivity exhibits hysteresis in temperature (Fig. 2.31(d)) due to

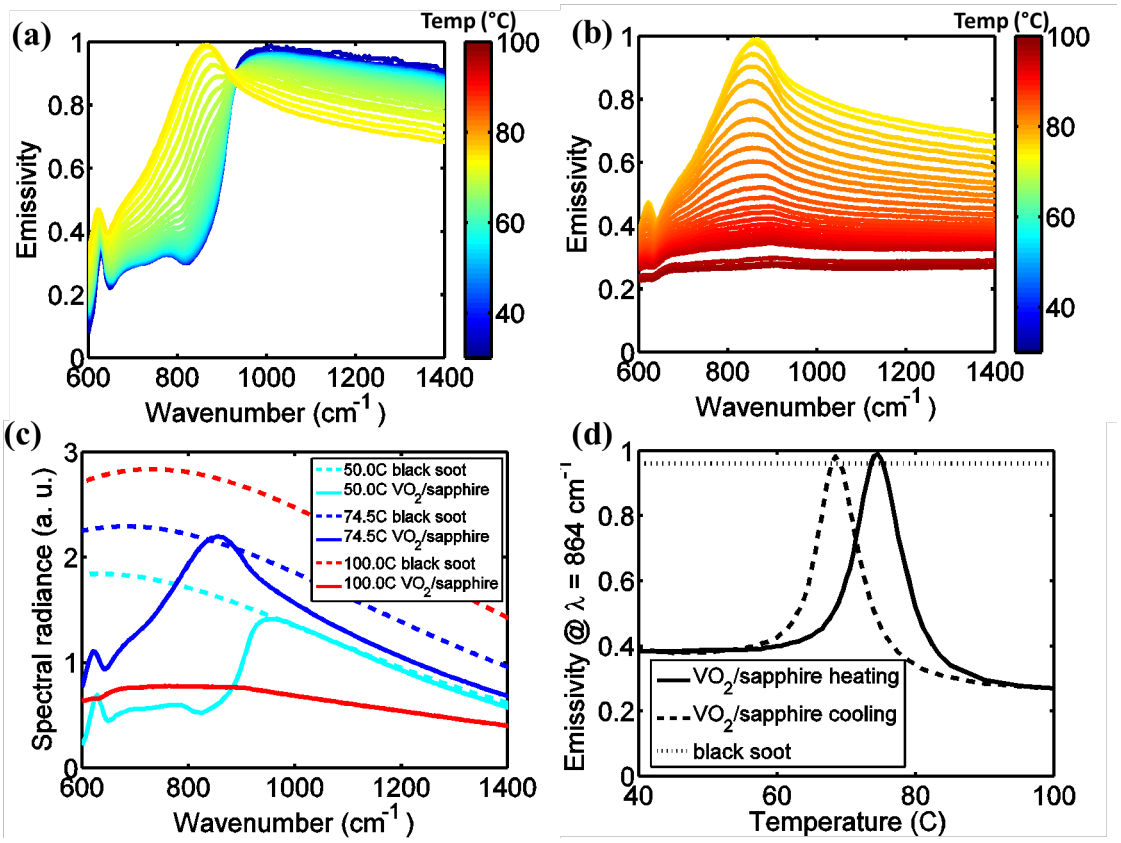

FIGURE 2.31: (a, b) Experimentally-determined evolution of the VO_2/sapphire emissivity for increasing temperature, separated into ranges of 35 °C – 74.5 °C and 74.5 °C – 100 °C for visual clarity. (c) Thermal emission density (spectral radiance) from black soot (dashed lines) and our VO_2/sapphire sample (solid lines) for three different temperatures. The data were taken for increasing temperatures. (d) Thermal emissivity of the VO_2/sapphire sample at a wavenumber of 864 cm^{-1} for heating (solid line) and cooling (dashed line), respectively. The dotted line denotes the assumed emissivity of the black soot reference ($\varepsilon = 0.96$).

the intrinsic hysteresis in undoped VO_2 [54]. Note that the data in Fig. 2.31(a, b) are shown for increasing temperatures only.

We integrated $I(K,T)$ of the black soot and VO_2/sapphire samples over the 8-14 μm atmospheric transparency window and plotted it as a function of temperature in Fig. 2.32(a). Plotted this way, it is clear that while heating, the samples displays broadband negative differential thermal emittance over the 73 °C – 85 °C temperature range while heating, and over 68 °C – 80 °C while cooling. The magnitude of the effect is large: over a $\approx 10^{\circ}$ C temperature range the slope is even larger in magnitude than the blackbody slope, indicating that the VO_2/sapphire sample has a larger negative differential

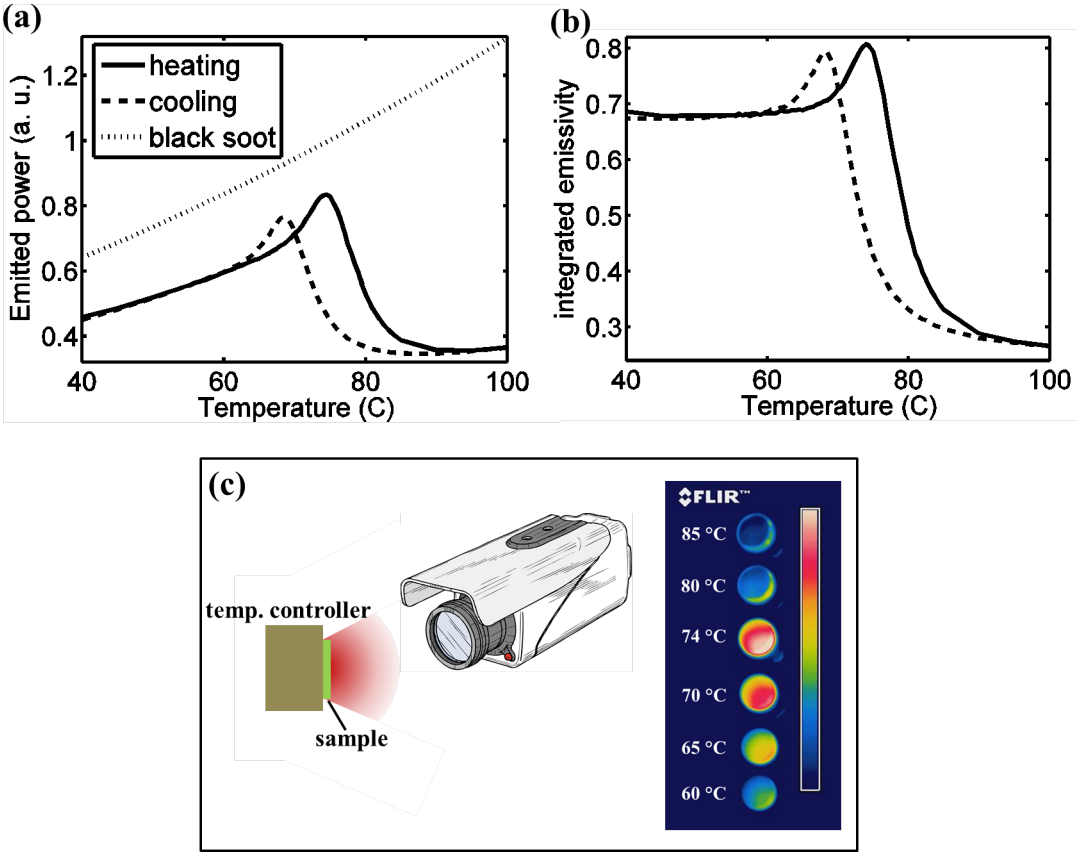

FIGURE 2.32: (a) Emitted power of the VO_2/sapphire sample integrated over the 8-14 μm atmospheric transmission window for heating (solid line) and cooling (dashed line), compared to the emitted power from black soot. (b) The integrated emissivity of the VO_2/sapphire sample over the 8-14 µm wavelength range. (c). Infrared camera images of the sample (diameter = 1 cm) for increasing temperatures.

thermal emittance than the blackbody positive differential thermal emittance over the same temperature range. Imaging these samples with a thermal camera (FLIR Systems Thermovision A40) confirms that due to the negative differential thermal emittance, the sample appears cooler even as it is heating up (Fig. 2.32(c)). Using the camera, some inhomogeneities in the thermal emittance of the film are visible, which likely result from slight inhomogeneities in the temperature and gradual long-range variations in the film thickness and roughness; these emittance inhomogeneities are amplified around the phase transition temperature.

The VO_2/sapphire thin film geometry (and, more generally, any geometries incorporating VO_2 with optical resonances in the infrared) is promising for a wide array of applications calling for tunable infrared emissivity, narrow-band "perfect" blackbody-like emission, negative differential thermal emittance, emissivity hysteresis, or some combination thereof. As one example, the emittance profile shown in Fig. 2.32 can be utilized to make a rewritable infrared "blackboard" by keeping the entire sample at the phase transition temperature, and using a cold or hot probe (such as a laser beam or soldering iron) to "write" messages by locally changing the emissivity. These persistent messages could be viewed with a thermal camera but would otherwise be invisible. A digital version of this device can be used as a rewritable infrared identification tag. As another example, the structure can be used as a type of infrared camouflage: within the 85 to 100 °C temperature region, the total thermally emitted power remains roughly constant, and therefore an infrared camera would not be sensitive to changes in temperature. The width of this flat-emittance region can be extended by decreasing the sharpness of the phase transition, which can be accomplished by introducing defects into the VO_2 films [96].

Depending on the application, the hysteresis intrinsic to VO_2 can either be beneficial (as in memory devices) or detrimental (for devices which require fast on/off switching). Fortunately, a variety of methods to modulate the hysteresis width have been studied, including engineering of the size and shape of grain boundaries [96] and stresses [97], as well as the introduction of various metallic dopants [98][99]. The aforementioned approaches have also been used to tailor the transition temperature of VO_2 within the 0°C to 100°C range [96][97][98][99], further expanding the application space.

While our study is limited to thin films of VO_2 on a sapphire substrate in the spectral region where the complex refractive index of sapphire is similar to that of metals at

visible or ultraviolet (UV) wavelengths due to the presence of strong phonon resonances, a variety of other substrates can be used to engineer the wavelength of the peak in emissivity resulting from the "ultra-thin-film resonance" in VO_2. Both highly-doped semiconductors and transparent conducting oxides (TCOs) have been shown to possess complex refractive indices similar to that of sapphire at λ = 10-15 μm (or metals in the visible/UV), and both can be engineered by modulating the doping [100], and are thus ideal candidate substrates for tailorable thermal emitters based on ultra-thin films of VO_2 or another material. The thin-film resonance condition can be further modified by introducing resonant metamaterials [57] or resonant optical antennas [101] on top or within the ultra-thin layer.

Ultimately, anomalous thermal emission properties which rely on the presence of a temperature-dependent emissivity such as the ones demonstrated in the present experiment can also be realized by integrating thermochromic materials into any number of optical structures including photonic crystals [83][102] or artificial metamaterials [87]. The inherent advantages of our thin-film geometry featuring a natural, disordered metamaterial within the VO_2 phase transition region are structural simplicity and ease of fabrication which allow for the creation of large-area anomalous thermal emitters. Nonetheless, emerging top-down and bottom-up fabrication methods may allow for the creation of large-area anomalous thermal emitters which combine thermochromics such as VO_2 with photonic crystals and artificial metamaterials to provide additional design degrees of freedom.

In conclusion, we have experimentally studied the infrared thermal emittance of a structure comprising a deeply-subwavelength thin film of vanadium dioxide (VO_2) on a sapphire substrate. Within the phase transition region of its insulator-metal transition (IMT), the VO_2 film comprises nanoscale islands of insulator- and metal-phase VO_2

which create a natural, disordered metamaterial with tunable optical dispersion and losses in the infrared, which leads to an absorption resonance within the film that appears and disappears upon temperature tuning. This resonance leads to a large peak in infrared emissivity spanning about 200 cm^{-1}, including a 50 cm^{-1} range over which the emissivity of the VO_2/sapphire sample is greater than that of black soot, a commonly used blackbody-like emissivity reference. This emissivity peak remains significant even when the emittance spectrum is integrated over the 8-14 μm atmospheric transparency window, and as a result the sample also features a broad-temperature (>10 °C) region of which it displays large negative differential thermal emittance such that the sample emits significantly less thermal radiation even as it is heated up. These anomalous emittance properties can find uses in infrared camouflage, thermal regulation, infrared tagging and identification, and other applications.

2.6 Additional discussion

In sections 2.2.4 and 2.4.1 we made the claim that the origin of the minimum in reflectivity (and hence maximum in absorbance) at the thin film is critical coupling to a resonance in the film. It is worth exploring this further: is there really a resonance in the film, and does a zero in the reflectivity necessarily correspond to critical coupling to this resonance?

We must first properly define resonance. The Wikipedia article on "resonance" defines it as "the tendency of a system to oscillate with greater amplitude at some frequencies than at others. [...] At these frequencies, even small periodic driving forces can produce large amplitude oscillations, because the system stores vibrational energy" [103]. According to Yariv and Yeh's *Photonics*, in an optical resonator, "the [resonance] frequencies are

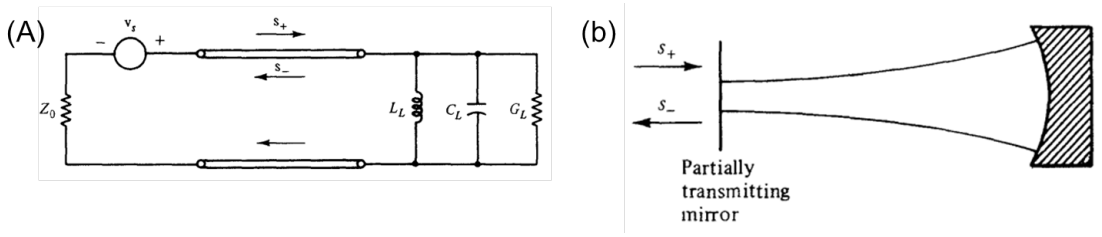

FIGURE 2.33: Schematics of a transmission line (a) or free space (b) terminated by a resonator. Reproduced from [26]

determined by the condition that the complete round-trip phase delay of a resonant mode be some multiple of 2π. [...] This requirement makes it possible for a stable standing wave pattern to establish itself" [104]. This definition of an optical resonance is fully consistent with the aforementioned general definition of resonance because the greatest electric field amplitude will tend to occur when a field has the same phase upon one round trip through the cavity, i. e. when there is a standing wave.

Next we must define the situation of "critical coupling to a resonance". Haus defines critical coupling as the situation when a waveguide (or free space, as in our case) is terminated by a resonator (or optical cavity), as shown in Fig. 2.33, the incident light is on resonance (no detuning from the resonant frequency), and the internal losses of the resonator are exactly matched with the external losses which are related to the coupling coefficient [26]. That means that a photon in the resonator that makes a single cycle (oscillation) is equally likely to be absorbed as it is to leak out of the resonator. This can be seen from the general expression for the complex reflection coefficient, which can be written as [26]

$$\tilde{r} = \frac{(1/\tau_e) - (1/\tau_o) - i(\omega - \omega_o)}{(1/\tau_e) + (1/\tau_o) + i(\omega - \omega_o)} \tag{2.6}$$

where ω is the angular frequency, ω_o is the resonance frequency, and $1/\tau_e$ and $1/\tau_o$ are the rate of decay due to escaping power and the rate of decay due to internal losses,

respectively. Clearly in order for the reflectivity $|\tilde{r}|^2$ to vanish, the relations $1/\tau_e = 1/\tau_e$ and $\omega = \omega_o$ must be satisfied, which is the definition of critical coupling.

With that definition of critical coupling to a resonator in mind, we now once again explore the analytical equation that describes the reflectance of a three layer system (Eqn. 2.1), which we reproduce below:

$$\tilde{r} = \frac{\tilde{r}_{12} + \tilde{r}_{23}e^{2i\tilde{\beta}}}{1 + \tilde{r}_{12}\tilde{r}_{23}e^{2i\tilde{\beta}}} \tag{2.7}$$

where $\tilde{r}_{mn} = (\tilde{p}_m - \tilde{p}_n)/(\tilde{p}_m + \tilde{p}_n)$, $\tilde{p}_m = \tilde{n}_m \cos(\tilde{\theta}_m)$, $\tilde{\beta} = (2\pi/\lambda)\tilde{n}_2 h \cos(\tilde{\theta}_2)$, $\tilde{\theta}_m = \sin^{-1}(\sin(\theta_1)/\tilde{n}_m)$, λ is the free space wavelength, $\tilde{n}_2 = n_2 + i\kappa_2$ is the complex index of medium 2, h is the thickness of medium 2, and the total reflectance $R = |\tilde{r}|^2$.

There are two limits of this equation that are interesting to explore. The first is the $R = 0$ condition which we term "perfect absorption" and is the one we are most interested in, and the $R \to \infty$ condition which we term "lasing threshold". The lasing threshold condition requires that the system have gain rather than loss, and that there is enough of this gain to sustain light oscillation with no light input. Note that we are still firmly in the realm of linear optics, so this is only valid precisely at threshold: any above-threshold behavior is nonlinear as a result of gain clamping [105], and thus can not simply be described by Eqn. 2.7.

The lasing condition $R \to \infty$ occurs when the demoniator of Eqn. 2.7 goes to zero, so $1 + \tilde{r}_{12}\tilde{r}_{23}e^{2i\tilde{\beta}} = 0$. By using $\tilde{r}_{21} = -\tilde{r}_{12}$ we can rewrite this as

$$1 = \tilde{r}_{21}\tilde{r}_{23}e^{2i\tilde{\beta}} = |\tilde{r}_{21}|\,|\tilde{r}_{23}|\,e^{i(\phi_{21}+\phi_{23})}e^{i4\pi\frac{h}{\lambda}n_2}e^{-4\pi\frac{h}{\lambda}\kappa_2} \tag{2.8}$$

where $\tilde{r}_{21} = |\tilde{r}_{21}|\, e^{i(\phi_{21})}$ and $\tilde{r}_{23} = |\tilde{r}_{23}|\, e^{i(\phi_{23})}$.

Breaking this up into the real and imaginary parts yields an amplitude condition (Eqn. 2.9) and a phase condition (Eqn. 2.10) for lasing. $\alpha_2 = 4\pi\kappa_2/\lambda$ is the gain/loss coefficient which is negative for gain and positive for loss, so it must be negative to meet the amplitude condition for lasing. $\phi_{prop} = \frac{\pi}{2}\frac{h}{\lambda/(4n_2)}$ is the propagation phase through thickness h of medium 2.

$$1 = \tilde{r}_{21}\tilde{r}_{23}e^{2i\tilde{\beta}} = |\tilde{r}_{21}|\,|\tilde{r}_{23}|\, e^{i(\phi_{21}+\phi_{23})}e^{i4\pi\frac{h}{\lambda}n_2}e^{-4\pi\frac{h}{\lambda}\kappa_2} \tag{2.9}$$

$$\phi_{21} + \phi_{23} + 2\phi_{prop} = 2\pi m \tag{2.10}$$

$$m \in \mathbb{Z}$$

From the phase condition in Eqn. 2.10 it is clear that the $R \to \infty$ lasing condition occurs precisely on resonance; that is, when the total round trip phase is a multiple of 2π, as expected.

Now we examine the $R = 0$ perfect absorption condition which we are more interested in. This occurs when the numerator of Ref. 2.7 goes to zero, so we can write this condition as

$$|\tilde{r}_{23}|\, e^{i(\phi_{23})}e^{i4\pi\frac{h}{\lambda}n_2}e^{-4\pi\frac{h}{\lambda}\kappa_2} = |\tilde{r}_{23}|\, e^{-4\pi\frac{h}{\lambda}\kappa_2}e^{i(\phi_{23}+4\pi\frac{h}{\lambda}n_2)} = |\tilde{r}_{21}|\, e^{i(\phi_{21})} \tag{2.11}$$

which can also be rewritten as separate amplitude (Eqn. 2.12) and phase (Eqn. 2.12) conditions:

$$|\tilde{r}_{21}| = |\tilde{r}_{23}|\, e^{-4\pi \frac{h}{\lambda}\kappa_2} = |\tilde{r}_{23}|\, e^{-h\alpha_2} \tag{2.12}$$

$$\phi_{23} + 2\phi_{prop} - \phi_{21} = 2\pi m \tag{2.13}$$

$$m \in \mathbb{Z}$$

From Eqn. 2.13, it is immediatelly apparent that the $R = 0$ does not occur on resonance unless $\phi_{21} = 0$, which only occurs if $\tilde{n}_2$ is purely real (i. e. medium 2 is lossless). So unless the film is purely lossless, the condition corresponding to maximum absorption is not the same as the condition corresponding to maximum field build up. It seems, then, that since $R = 0$ does not occur on resonance, it may not be considered "critical coupling" according to the definition of Haus [26]. Nethertheless, the derivation by Haus seems to imply a relatively small amount of loss, so perhaps our $R = 0$ condition falls under some sort of generalized definition of critical coupling. Ultimately this is just a discussion about semantics, but the analysis in this section may contribute to the overall understanding of these ultra-thin film, highly-lossy optical systems.

Chapter 3

Controlling light propagation with optical antenna metasurfaces

3.1 Introduction

In the context of physical optics the general function of most optical devices can be described as the modification of the wavefront of light by altering its phase, amplitude, and polarization in some desired manner. The class of optical components with a spatially varying phase response includes lenses, prisms, spiral phase plates [106], axicons [107], phase retarders, and more generally spatial light modulators (SLMs), which are able to imitate many of these components by means of a dynamically tunable spatial phase response [108]. Another broad class of optical components such as gratings and holograms is based on diffractive optics [109], where diffracted waves from different locations on a diffractive element interfere in the far-field (i. e. the Fraunhofer zone) to produce the desired optical pattern. These optical components generally shape optical wavefronts by relying on gradual phase shifts accumulated during propagation through different optical

lengths. This approach has been generalized in the field of transformation optics [110] [111] which utilizes composite materials with an engineered complex refractive index, or "metamaterials", to engineer the spatial distribution of refractive indices and therefore bend light in unusual ways, enabling striking phenomena such as negative refraction, subwavelength-focusing, and optical cloaking, among others [63] [112].

It is possible to break away from our reliance on the propagation effect and attain new degrees of freedom in optical design by introducing abrupt phase changes into the optical path (also abrupt amplitude and polarization changes, though these are more easily achieved and therefore we mainly focus on the abrupt phase control) [113] [114] [115] [116] [117] [118] [119]. This can be achieved by using the large and controllable phase shift between the excitation and re-radiation of optical resonators. This approach enables the design a new class of optical devices with pixellated phase elements, which are thin compared to the wavelength of light. The choice of optical resonators is potentially wide-ranging, from nano-cavities [73] [120], to nanoparticle clusters [121] and optical antennas [122]. In principle even quantum dots, nanocrystals, or resonant molecules could be used, though these are much more difficult to engineer. For our work, we focused on optical antennas, due to their widely tailorable optical properties and the ease of fabrication. In general, resonant behavior can be found for any type of vibration, including mechanical, electrical, optical, and acoustic, among others, and can be utilized in the manipulation of these various kinds of waves (e.g. [123] [124]).

Optical antennas are metal-based optical resonators that can manipulate manipulate light on a subwavelength scale and have a wide range of potential applications [125] [122] [126] [127] [128] [129] [130] [131] [132]. A commonly used definition from radio and microwave antenna theory states that the purpose of an antenna is to convert the energy of free space propagating radiation to localized energy "receiving antenna"),

and vice versa ("transmitting antenna") [133]. As such, one of the main themes of previous research efforts has been the capability of optical antennas to efficiently capture and concentrate light, enabling the enhancement of a variety of optical processes such as raman scattering [130], second harmonic generation [131], and nonlinear four-wave mixing [132].

We became interested in using optical antennas not in receiving or transmitting mode, but in scattering mode whereby an antenna simultaneously receives and then re-emits light. This process modifies the amplitude, phase, and polarization of an optical wavefront and thus can be used to re-direct and otherwise control light. In particular, the phase response of optical antennas has not been systematically studied prior to our work, and it is this feature that enables fine control over the propagation of light.

In the majority of cases, optical antennas fall squarely within the realm of linear optics, and can thus be modeled with conventional electromagnetic techniques such as the finite difference time domain (FDTD) method and the finite element method (FEM) [134]. As as a result much modern research involving these and other plasmonic structures revolves around using these solvers to predict and design the optical response. However, this "brute force" type of modeling has two limitations: (1) it provides limited intuition about the physics, making it difficult to design new structures in non-incremental ways and (2) it is relatively slow and resource-intensive, making it difficult to explore large parameter spaces.

Because of this, we developed several analytical or semi-analytical models which illustrate the physics behind the phase response of optical antennas. First, we use an analogy to the impedance of electric circuit elements which provides some intuition about the the charge, current, and near-field distributions of an optical antenna across a resonance (i.e.

at different detunings). Then we develop simple one-dimensional and two-dimensional "charged mass on a spring" oscillator models which explicitly separate the radiation reaction damping and the Ohmic absorption damping mechanisms for each fundamental eigenmode of an antenna. This model not only provides a simple way to understand antennas with multiple resonances, but also yields insight to the absorption, scattering, and near-field response of plasmonic structures in general.

After looking at these heuristic models, we develop two fully-analytical models based on solving rigorous integral equations of antenna currents that consider retardation effects and near-field interactions. We adapt methods used in radio frequency antennas for optical frequencies, and verify the validity of our models by comparing the results with full-wave FDTD simulations. After that, we explore the properties of V-shaped optical antennas by mapping out their two plasmonic eigenmodes and polarization conversion properties. These antennas are good examples of two-dimensional plasmonic structures and are the building blocks of our metasurfaces, which are essentially phased optical antenna arrays.

Wfter that, we discuss several applications of these metasurfaces, which are designed to mold an incident wavefront into desired shapes over a propagation distance which is smaller than or comparable to the optical wavelength. By using inhomogeneous arrays of V-shaped optical antennas (which we sometimes refer to as "optical phase discontinuities), we demonstrate generalized laws of refraction and reflection at an interface, tunable birefringence including background-free plasmonic wave plates, generation of optical vortices that carry optical angular momentum, and flat, ultra-thin optical components including lenses, axicons, and wave-plates. We conclude with some thoughts about how to add dynamic tunability to optical antennas, with the ultimate goal of

realizing fast, tunable metasurfaces for applications which include beam steering and fast spatial light modulators.

3.2 Semi-analytical models

3.2.1 Heuristics

The phase shift between the scattered and incident light of an optical resonator sweeps a range of approximately π across a resonance (from far below resonance to far above). This π phase shift corresponding to a resonance is observed in many other physical systems between the response of a resonator and its driving force (e.g., when the frequency of an applied force tunes over the resonant frequency of a mechanical harmonic oscillator such as a mass on a spring). Befpre resorting to rigorous theoretical models or full-wave simulations, we can gain a qualitative physical understanding by considering the phase response of a linear optical antenna of length L. If the antenna is small compared to the wavelength of light (i.e. $L/\lambda_0 << 1$), its charge distribution instantaneously follows the incident field (Fig. 3.1(a)), i.e., $\tilde{\sigma} \propto \tilde{E}_{inc} = E_{inc}\exp(i\omega t)$, where $\tilde{\sigma}$ is the charge density at one end of the antenna. This is referred to as the quasistatic limit. Therefore the emitted electric field, which is proportional to the acceleration of the charges (as is described by the classical Larmor formula [135]), is $\tilde{E}_{scat} \propto \partial^2\tilde{\sigma}/\partial t^2 \propto -\omega^2\tilde{E}_{inc}$. That is, the incident and scattered fields are π out of phase (also note that the ω^2 in electric field term becomes ω^4 in intensity, which is the familiar fourth-order dependence of scattered power on the frequency from Rayleigh scattering [136]). At the first order antenna resonance which occurs when the length is approximately half of the wavelength (i.e. $L/\lambda_0 \approx 1/2$), the incident field is in phase with the current at the center of the antenna (Fig. 3.1(a)), i.e. $\tilde{I} \propto \tilde{E}_{inc}$, and therefore drives the current most efficiently. As a result,

$\tilde{E}_{scat} \propto \partial^2\tilde{\sigma}/\partial t^2 \propto \partial\tilde{I}/\partial t \propto i\omega\tilde{E}_{inc}$, so the phase difference between $\tilde{E}_{scat}$ and $\tilde{E}_{inc}$ is $\pi/2$. For a long antenna with length comparable to the wavelength (i.e. $L/\lambda_0 \approx 1$), the antenna impedance (defined as the incident field divided by the current at the center of the antenna) is primarily inductive, or $\tilde{I} \propto -i\tilde{E}_{inc}$. Consequently, the scattered and incident light are almost in phase, $\tilde{E}_{scat} \propto \partial\tilde{I}/\partial t \propto \tilde{E}_{inc}$. So to summarize: for a fixed excitation wavelength, the impedance of an antenna changes from capacitive, to resistive, and to inductive cross a resonance as the antenna length increases, and a single antenna resonance is able to provide a range of phase change at most π between the scattered and incident light.

3.2.2 Single oscillator model for linear optical antennas

In this section, we describe a simple oscillator model for optical antennas and, in general, any nanostructures supporting localized surface plasmon resonances (LSPRs) [138] [122]. The model treats the resonant, collective oscillations of electrons in the nanostructure as a damped, driven harmonic oscillator consisting of a charge on a spring. Unlike previously proposed oscillator models in which all damping mechanisms were combined into a single loss term proportional to the charge velocity [139][140][141], we explicitly account for two decaying channels for LSPR modes: free carrier absorption (internal damping) and emission of light into free space (radiation damping) [114].

We begin by analyzing a system in which a charge q located at $x(t)$ with mass m on a spring with spring constant κ (Fig 3.2(a)) is driven by an incident electric field with frequency ω, and experiences internal damping with damping coefficient Γ_a:

$$m\frac{d^2x}{dt^2} + \Gamma_a\frac{dx}{dt} + \kappa x = qE_0e^{i\omega t} + \Gamma_s\frac{d^3x}{dt^3} \tag{3.1}$$

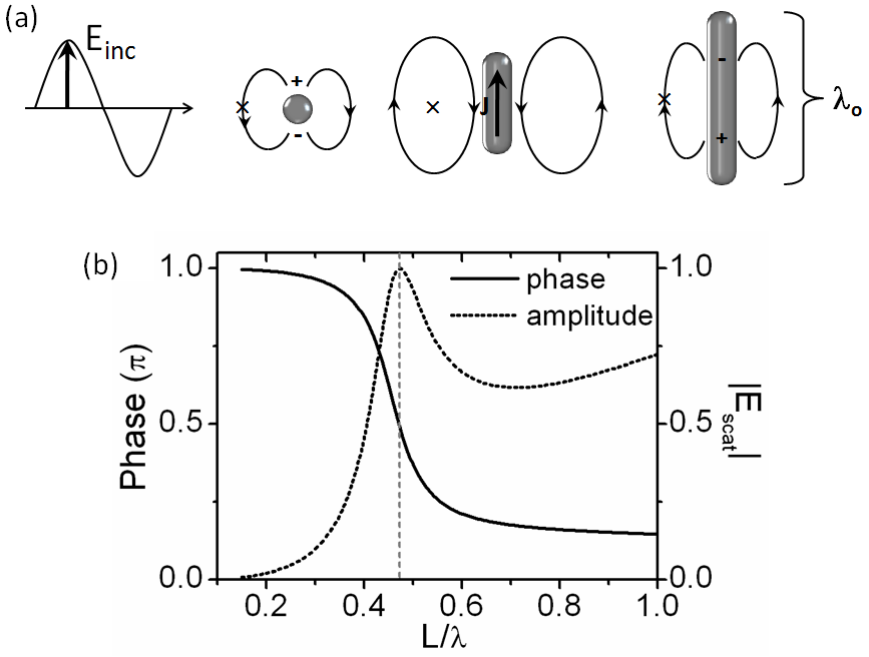

FIGURE 3.1: Schematics showing the instantaneous distributions of charge, current (big arrow through the antenna), and near-field (electric-field lines) of rod antennas of different lengths at the instant in time when the incident electric field is upward and has the largest amplitude. A perfectly conducting metal is assumed and antennas are suspended in vacuum. The second panel shows that maximum amount of charges accumulates at the ends of an antenna with length $L << \lambda_0$ and the current flowing through the antenna is zero. The third panel shows that the instantaneous current on a resonant antenna with $L \approx \lambda_0/2$ is maximized and is in phase with the incident field, while there is no charge accumulation at the ends. In the last panel, for an antenna with $L \approx \lambda_0$, the charge accumulation is again maxized (but located at a distance of about $L/4$ from the ends [137]) and there is no net current through the antenna. Assuming a test point (a monitor) $\lambda_0/4$ away from the antennas (indicated by the cross in the third panel) and measure the phase difference $\Delta\Phi$ between the antenna radiation at that point and the incident field. By comparing the electric field lines around the antennas and the instantaneous incident field it can be seen that $\Delta\Phi$ is π, $\pi/2$, and 0 for the three antennas with $L << \lambda_0$, $L \approx \lambda_0/2$, and $L \approx \lambda_0$, respectively. (b) Amplitude and phase response of a rod antenna as a function of antenna length calculated by analytically solving Hallen's integral equations for linear antennas [137]. The antenna is suspended in vacuum and has a circular cross-section with an aspect ratio of 50 (i.e. radius $r = L/50$). In this calculation, incident monochromatic light is incident normal to the rod and is polarized along it. The scattered light is monitored in the far-field along the direction of the incident light.

In addition to the internal damping force $F_a(\omega) = \Gamma_a dx/dt$, the charge experiences an additional force $F_s(\omega) = \Gamma_s d^3x/dt^3$ due to radiation reaction, where $\Gamma_s = q^2/6\pi_0 c^3$. This term describes the recoil that the accelerating charge feels when it emits radiation that carries away momentum, and is referred to as the Abraham-Lorentz force or the radiation reaction force [136]. Since classical laws of electrodynamics necessitate that an accelerating charge release energy in the form of radiation, conservation of energy implies that this charge must consequently lose kinetic energy. The form of the radiation reaction force can be derived by applying an energy balance argument to the classical Larmor formula for radiated power, and it can also be seen as the force which the field produced by the charge exerts on the charge itself [142]. For our charge-on-a-spring model, the radiation reaction term has to be included for physical consistency, and cannot be absorbed into the internal damping coefficient Γ_a.

By assuming harmonic motion $x(\omega, t) = x(\omega)e^{i\omega t}$ we can immediately write down the steady-state solution to Eqn. 3.1 as

$$x(\omega, t) = \frac{(q/m)E_0}{(\omega_0^2 - \omega^2) + i\frac{\omega}{m}(\Gamma_a + \omega^2\Gamma_s)} e^{i\omega t} = x(\omega)e^{i\omega t} \tag{3.2}$$

where $x(\omega)$ contains the amplitude and phase response of the oscillator and $\omega_0 = \sqrt{k/m}$. The time-averaged absorbed power by the oscillator can be written as $P_{abs}(\omega) = F_a(\omega)^*(i\omega x(\omega))$, where $F_a(\omega)^*$ is the complex conjugate of the internal damping force. Similarly, the time-averaged scattered power by the oscillator is $P_{scatt}(\omega) = F_s(\omega)^*(i\omega x(\omega))$. Therefore we have:

$$P_{abs}(\omega) = \omega^2\Gamma_a|x(\omega)|^2 \tag{3.3}$$

$$P_{scat}(\omega) = \omega^4\Gamma_s|x(\omega)|^2 \tag{3.4}$$

where

$$|x(\omega)|^2 = \frac{(q/m)^2 {E_0}^2}{\left({\omega_0}^2 - \omega^2\right)^2 + \frac{\omega^2}{m^2}\left(\Gamma_a + \omega^2 \Gamma_s\right)^2}. \tag{3.5}$$

Our oscillator model can shed light on the relationship between the near-field, absorption, and scattering spectra in optical antennas. Broadly considering the study of localized surface plasmon systems, a number of both near- and far-field quantities are used to characterize plasmonic resonances with the most common ones being near-field enhancement, and the absorption and scattering cross-sections (the last two are often combined into an extinction cross-section). It has been observed that the wavelength dependence of near-field quantities such as electric field enhancement can be significantly red-shifted compared with far field quantities such as scattering [18] [19] [20] [21] [22] [23]. This discrepancy has significant implications for plasmonic applications where care must be taken to optimize the appropriate figure of merit for the wavelength of interest.

If we interpret the optical antenna as an oscillator that obeys the absove equations, we can associate P_{abs} and P_{scat} in Eqns. 3.3 and 3.4 with the scattering and absorption spectra of the antenna. Furthermore, we can calculate the near-field intensity enhancement at the tip of the antenna as $|E_{near}(\omega)|^2 \propto |x(\omega)|^2$ [122].

By examining Eqns. 3.3 and 3.4 and noting that $P_{scat} \propto \omega^2 P_{abs} \propto \omega^4 |E_{near}(\omega)|^2$ we can deduce that the scattering spectrum $P_{scat}(\omega)$ will be blue-shifted relative to the absorption spectrum $P_{abs}(\omega)$, which will in turn be blue-shifted relative to the near-field intensity enhancement spectrum $|E_{near}(\omega)|^2$. This is in agreement with experimental observations that the wavelength dependence of near-field quantities such as the electric-field enhancement can be significantly red-shifted compared with far field quantities such as scattering spectra [143][144][145][146][147][148]. These spectral differences can also be clearly seen in finite difference time domain (FDTD) simulations of gold linear

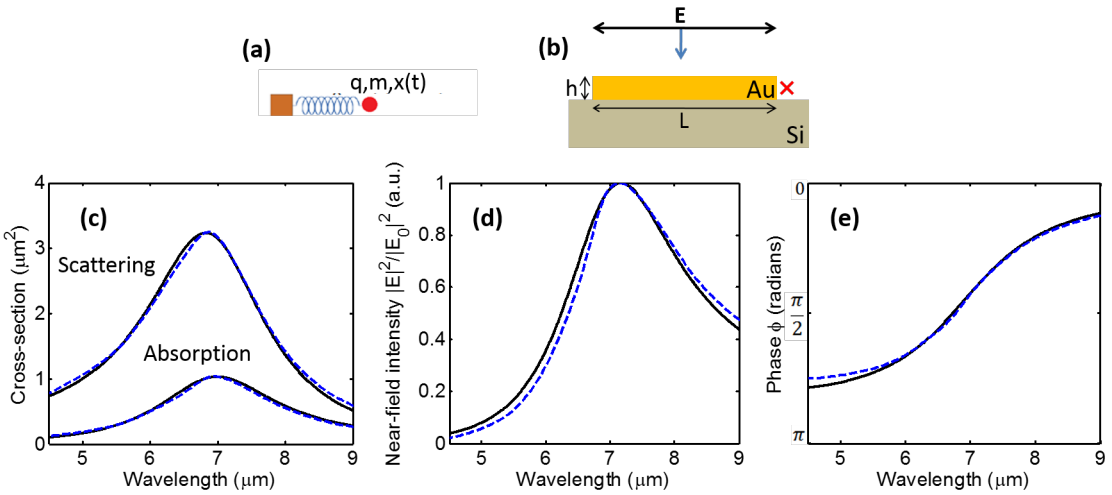

FIGURE 3.2: (a) Representation of an optical antenna in oscillator form, where q is the charge, m is the inertial mass, and $x(t)$ is the displacement from the equilibrium position. (b) Schematics for FDTD simulations. A gold optical antenna (length L = 1 μm, thickness t = 50 nm, width w = 130 nm) sits on a silicon substrate and is illuminated by a normally incident plane wave polarized along the antenna axis. The cross represents the point approximately 4 nm away from the antenna edge where the near-field is calculated. Complex permittivity of gold is taken from Palik [64]. (c) Scattering and absorption cross-sections as calculated via FDTD (dashed curves) and the model (solid curves). (d) Near-field intensity calculated by the oscillator model (solid curve) and via FDTD (dashed curve) at the location identified by the cross, with the incident field subtracted off. (e) Oscillator phase (solid curve) and the phase of the near-field calculated via FDTD (dashed curve).

antennas on a silicon substrate designed to resonate in the mid-infrared spectral range (Fig. 3.2(b)). In Fig. 3.2(c-e), we show the scattering and absorption cross-sections, the near-field intensity, and the near-field phase, respectively, for our antenna as calculated by FDTD (dashed lines). We fit the simulation results presented in Fig. 3.2(c) with Eqns. 3.3 and 3.4 to obtain the parameters q, m, ω_0, and Γ_a. The resulting model is able to explain the peak spectral position and general shape of the near-field intensity (Fig. 3.2(d)), as well as the phase response of the antenna (Fig. 3.2(e)). Note that no additional fitting was done to obtain the near-field curves in Figs. 3.2(d) and (e). This result suggests that this model can predict the near-field amplitude and phase response from experimental far-field spectra of antennas, which are much easier to obtain than near-field measurements.

The parameters obtained from the fit are consistent with the interpretation that the

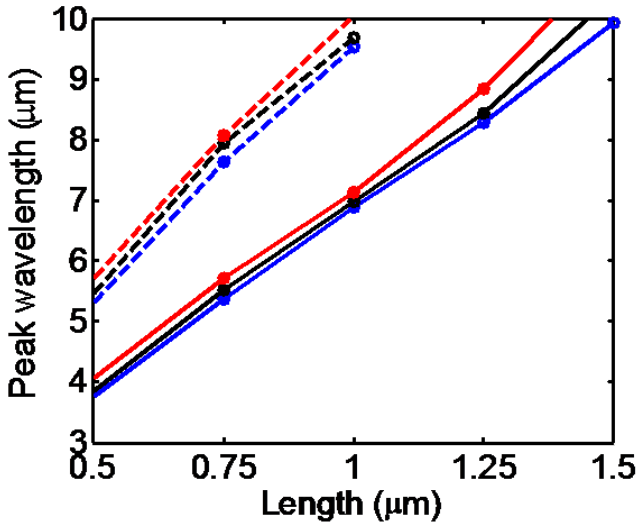

FIGURE 3.3: Peak wavelengths of the near-field (red), absorption (black), and scattering (blue) of linear antennas (w = 130 nm, h = 50 nm, gold) of various lengths sitting on (solid lines) and embedded in (dashed lines) a silicon substrate

driving and radiative damping of the antenna mode are due to conduction electrons in the antenna. Our model shows that in LSPR systems the near-field, absorption, and scattering spectra are all expected to peak at different frequencies and have distinct profiles, which agree very well with electromagnetic simulations of plasmonic antennas in the mid-infrared, and are consistent with experiments.

To further illustrate the spectral differences between our quantities of interest, in Fig. 3.3 we plot the wavelength peaks of the scattering (blue), absorption (red), and near-field (black) spectra for antenna lengths from 0.5 μm to 1.5 μm both on a silicon substrate (solid lines) and embedded in silicon (dashed lines). In both cases, the aforementioned trend remains unchanged, with the near-field peak always red-shifted relative to the absorption, and with both red-shifted relative to the scattering spectrum.

3.2.3 Two-oscillator model for 2D structures supporting two orthogonal plasmonic modes

To gain full control over an optical wavefront, we need a subwavelength optical element able to tailor the phase of the radiated light relative to that of the incident light over a range of 2π. Single oscillators such as the linear optical antennas shown in the last section cannot be engineered in a way to provide an arbitrary phase response over the entire 2π range, and can barely cover a range of π while maintaining a large scattering cross-section (Figs. 3.2(c) and (e)), so a more elaborate oscillator element is required. In this section, we show that an element consisting of two independent and orthogonally oriented oscillator modes is sufficient to provide arbitrary amplitude and phase response, and is therefore suitable for the creation of designer optical interfaces. We derive the phase and amplitude properties of this two-oscillator system, and illustrate how the phase coverage is extended due to the dual oscillator modes and a phase contribution from a coordinate transformation [115].

We focus on lithographically-defined nanoscale V- and Y-shaped plasmonic antennas as examples of two-oscillator systems. These antennas exhibit two non-interacting plasmonic modes, each of which can be treated as an independent oscillator. We choose our axes such that the two oscillators are oriented along x and y axes, respectively, with the incident light propagating along z and its electric field oriented along an axis w, which lies in the x-y plane at an angle θ from the y-axis (Fig. 3.4(b)). According to Eqn. 3.4 the fields scattered by the oscillators oriented along the x- and y-axis can be written respectively as

$$E_{s,x}(\omega) = -D_x(\vec{r})\sqrt{\Gamma_{s,x}}\omega^2 x(\omega) \tag{3.6}$$

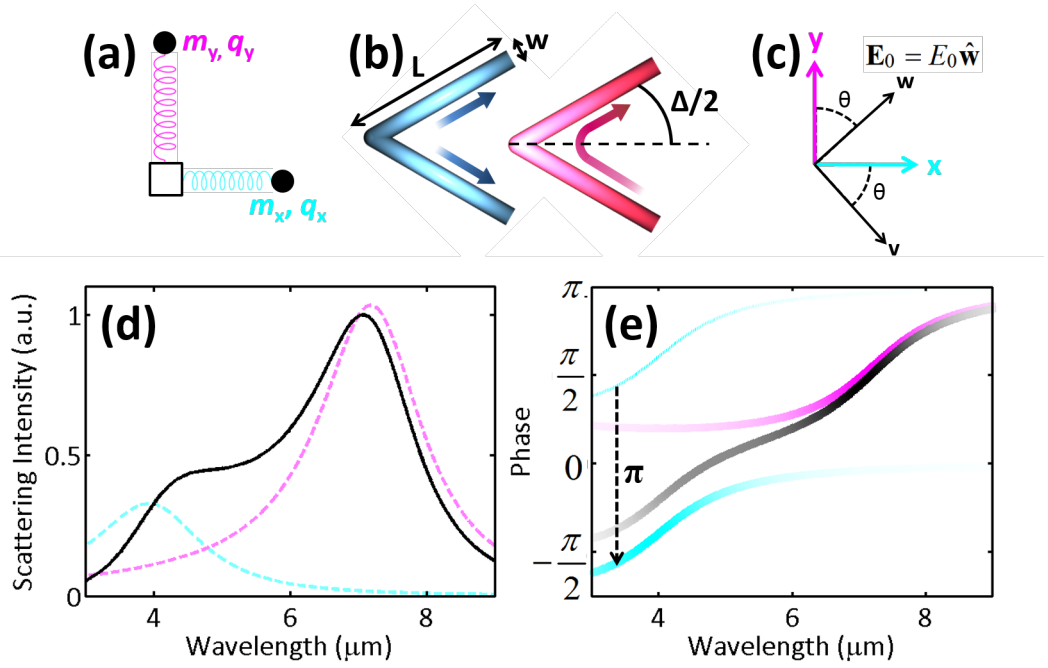

FIGURE 3.4: (a) Charge-oscillator model for a two-oscillator element, where q is the charge and m is the inertial mass. (b) Two coordinate systems related by a rotation by angle θ. The x-y axes are along the two fundamental oscillator modes, the w-axis is along the polarization of the incident field, and the v-axis is along the cross-polarization direction with respect to the incident polarization. A V-shaped optical antenna is a simple example of a plasmonic two-oscillator element. Its two orthogonal modes, i.e., symmetric and antisymmetric modes, are shown respectively in (c) and (d). The schematic current distribution on the antenna is represented in gray scale with lighter tones indicating larger current density. The instantaneous direction of current flow is indicated by arrows with gradient. (e) Calculated intensity ($|E|^2$) of the field scattered into the cross-polarization by individual oscillators representing the two modes of a V-shaped antenna (dashed and dotted curves) with $\Delta = 90°$ and $h = 650$ nm, and by the two-oscillator system representing the V-antenna (solid curve) for $= 45°$. Note that the solid curve is not simply the sum of the dashed and dotted curves because of the coherent addition of fields. (f) Phase of the field scattered into the cross-polarization by the individual oscillators (dashed and dotted curves), and by the two-oscillator system (solid curve).

$$E_{s,y}(\omega) = -D_y(\vec{r})\sqrt{\Gamma_{s,y}}\omega^2 y(\omega) \tag{3.7}$$

where $D_{x(y)}(\vec{r})$ contains the angular and radial dependence of the emitted field. In general, light is scattered by our two-oscillator element into some elliptical polarization state. We focus on light scattered only into the polarization state along the v-axis in Fig. 3.4(b), which is the cross-polarized direction relative to the incident polarization. The reason for this particular choice is two-fold; the first is a matter of experimental

convenience as it allows us to fully decouple the scattered light from the incident light by simply filtering out the former with a linear polarizer. The second is more subtle; as we will show, this configuration provides an additional phase shift which extends the potential phase coverage of our elements to the full 2π range.

Given an incident field polarized along the w-axis (Fig. 3.4(b)), we wish to study the component of the emitted field polarized along the v-direction We can break up this polarization-conversion process into two steps: the in-coupling of incident light into the two oscillator modes, and the out-coupling of cross-polarized light from the oscillators. The in-coupling process depends on θ because it involves the projection of the incident field along the two oscillator modes, i.e., $E_{0,x} = E_0 \hat{w} \cdot \hat{x} = E_0 \sin(\theta)$ and $E_{0,y} = E_0 \hat{w} \cdot \hat{y} = E_0 \cos(\theta)$. For the out-coupling process, we project the field scattered by each oscillator onto the v-axis (Fig. 3.4(b)):

$$E_{s,x} \hat{v} \cdot \hat{x} = -D_x(\vec{r}) \sqrt{\Gamma_{s,x}} \omega^2 x(\omega) E_{0,x} \cos(\theta) \tag{3.8}$$

$$E_{s,y} \hat{v} \cdot \hat{y} = D_y(\vec{r}) \sqrt{\Gamma_{s,y}} \omega^2 y(\omega) E_{0,y} \sin(\theta) \tag{3.9}$$

After summing these projections, the total cross-polarized field emitted by the structure $E_{s,v}$ can be written as

$$E_{s,v}(\omega) = D(\vec{r}) \frac{E_0}{2} \sin(2\theta) \omega^2 \left[\sqrt{\Gamma_{s,x}} x(\omega) e^{i\pi} + \sqrt{\Gamma_{s,y}} y(\omega) \right] \tag{3.10}$$

where we assumed that $D_x(\vec{r}) \approx D_y(\vec{r}) = D(\vec{r})$, which is true for light emitted roughly normal to the orientation of the two oscillators. Equation (3.10) provides a complete

description of the generation of cross-polarized light by our two-oscillator system.

A large class of plasmonic elements can support two orthogonally-orientated modes. We choose V-shaped antennas consisting of two arms of equal length h connected at one end at an angle Δ. They support "symmetric" and "antisymmetric" modes (Figs. 3.4(c) and (d)), which are excited by electric-field components parallel and perpendicular to the antenna symmetry axis, respectively. In the symmetric mode, the current and charge distributions in the two arms are mirror images of each other with respect to the antenna's symmetry plane, and the current vanishes at the joint that connects the two arms (Fig. 3.4(c)). This means that, in the symmetric mode, each arm behaves similarly to an isolated rod antenna of length h, and therefore the first-order antenna resonance occurs at $h \approx \lambda_{\text{eff}}/2$, where λ_{eff} is the effective wavelength [122]. In the antisymmetric mode, antenna current flows across the joint (Fig. 3.4(d)). The current and charge distributions in the two arms have the same amplitude but opposite sign, and they approximate those in the two halves of a straight rod antenna of length $2h$, and the condition for the first-order resonance of this mode is $2h \approx \lambda_{\text{eff}}/2$. The calculations of Fig. 3.4(e) indeed show that the two modes differ by about a factor of 2 in resonance wavelength.

The calculated intensity $|E_{s,v}(\omega)|^2$ and phase $\phi(\omega)$ of the cross-polarized light $E_{s,v}(\omega) = |E_{s,v}(\omega)|\, e^{i\phi(\omega)}$for a representative V-antenna are plotted in Figs. 3(e) and (f). The specific parameters $\Gamma_{a,i}$, $\Gamma_{s,i}$, m_i, $\omega_{0,i} (i \in x, y)$ for its two modes correspond to antenna geometries specified in the caption of Fig. 3.4. As can be clearly seen from the black curve in Fig. 3.4(f), our two-oscillator element is able to span twice the range of phase of either single oscillator (dashed or dotted), even though the two oscillators are uncoupled. This phase extension, which can be seen as the $e^{i\pi}$ term in Eq. (3.10), is due to the

fact that the projections of the scattered fields from the spatially-overlapped x- and y-oriented oscillators onto the v-axis are opposite in phase (Fig. 3.4(b)).

Equation (3.10) encodes the θ-dependence of the polarization conversion properties with a $\sin(2\theta)$ term. No cross-polarized light is generated for $\theta = 0°$ or $90°$ when the incident field is aligned along one of the two orthogonally-oriented modes, and maximum polarization conversion is obtained for $\theta = 45°$. A feature of the two-oscillator element is that the rotation of both oscillators relative to the incident polarization allows for control of the scattering amplitude independent of the phase response or the linewidth of the resonances. Within the 0-90° range, the θ-dependence in Eq. (3.10) only affects the amplitude of $E_{s,v}$, so θ can be used as a degree of freedom to control the cross-polarized scattering amplitude of the two-oscillator element without altering its phase response. Due to the $\sin(2\theta)$ dependence, a rotation of the structure by 90° maintains the amplitude of cross-polarized scattering while adding an extra phase of π to the scattered light. This feature is used in later sections to generate 8 distinct phase elements from 4 structures and allows us to construct antenna elements that are able to span the full 0-to-2π range in phase, while maintaining relatively large scattering amplitudes.

3.3 Analytical models for V-shaped optical antennas

In this section, we present two analytical models for solving the current distribution and scattered fields of V-shaped antennas and in doing so obtain a detailed picture of their near- and far-field properties. In particular, we are able to study the near-field coupling between the two antenna arms, and accurately map the amplitude, phase, and polarization of the antenna radiation. These modeling tools enable us to select and assemble various V-shaped antennas into more complex optical components. We

should emphasize that while these models are computationally-efficient and fast, they are limited in application to V-shaped antennas embedded in a homogeneous environment. By using these models together with certain approximations we are able to deduce the optical response from these antennas on a substrate, but if we desire to study any other type of antenna (e.g. a Y-shaped antenna, or any more complicated shape) via analytical methods, new models must be developed.

Models describing the response of antennas have been extensively studied [137][149][150][151]. One of the main challenges is that the integral equations governing the behavior of antennas have no exact analytical solutions. However, the integral equations can be solved in an approximate way by following an iteration procedure developed in 1950s by King [137]. Furthermore, with the development of numerical methods in the last few decades, we can obtain accurate numerical solutions of the integral equations by using the method of moments (MoM).

Our solutions follow the derivations presented in ref. [137] for solving Hallen's integral equation using the iteration method, and in ref. [151] for solving Pocklington's integral equation using the MoM. We derived the integral equations governing the behavior of V-shaped cylindrical antennas, reduce the 2D problem to one dimension, and implement a numerical solution based on the iteration method or the MoM. We obtain the current distribution driven at the surface of the antenna by an incident excitation field. The far-field scattered by the antenna in any direction, with amplitude, phase and polarization information, is then calculated as the coherent sum of the fields scattered by a series of infinitesimal current elements distributed along the antenna and having their amplitude and phase given by the current distribution, using an analytical expression for the radiation pattern of interfacial dipoles [152].

Because the derivations are lengthy and themselves do not shed light on antenna behavior, we do not reproduce them in this thesis. Instead the iteration technique derivation can be found in the supplementary information of ref. [113], and the MoM derivation can be found in the appendix of ref. [119]. We study how the methods and approximations used for long-wavelengths apply to the mid-infrared spectral range, where plasmonic properties play a significant role, by comparing the results of our analytical models with the results of FDTD simulations. Our main goal in this section is to demonstrate fast and efficient methods as alternatives to full-wave simulations to probe a large design parameter space, bringing techniques commonly used in the microwave and radio frequency ranges into the optical regime.

The main approximation used in our derivations is the thin-wire approximation ($a << \lambda_o$ and $a << h$, with a being the antenna radius and h its arm length) which enables us to consider the current distribution on the antenna to be purely axial and azimuthally invariant [150][151]. While fully justified at long wavelengths, this approximation may not necesarily hold for mid-infrared antennas for which typically $\lambda_o a \approx 50$ and $h/a \approx 10$. Our first task is thus to validate our results by comparing them to the results of well established simulation tools such as FDTD. We assume monochromatic light at $\lambda_o = 7.7\mu$m coming at normal incidence with respect to the antenna plane. We calculated the amplitude and phase of the scattered light in the far-field, in the direction normal to the plane of the antenna, for different antenna arm lengths h, ranging from 0.3 to 1.6 μm, and different opening angles Δ, ranging from 0 to 180°. The results are summarized in Fig. 3.5 for the symmetric and antisymmetric plasmonic mode (see inset schematics). We observe a good agreement between FDTD calculations and our calculations based on the MoM and iteration method. The locations of the two modes are different with respect to h because the physical length of the antenna for the two modes differs by a

factor of 2. We also observe a phase shift approximately equal to π across the resonances, as is expected across any resonance. We note that our calculations are in good agreement with FDTD simulations for $\Delta < 90°$, where the shift of the resonance peaks occurs, indicating that the interaction between the antenna arms is well accounted for in our analytical models. These maps were obtained in about 20 seconds using the MoM, and about half an hour using the iteration method on a desktop computer, compared to about one month for the FDTD calculations.

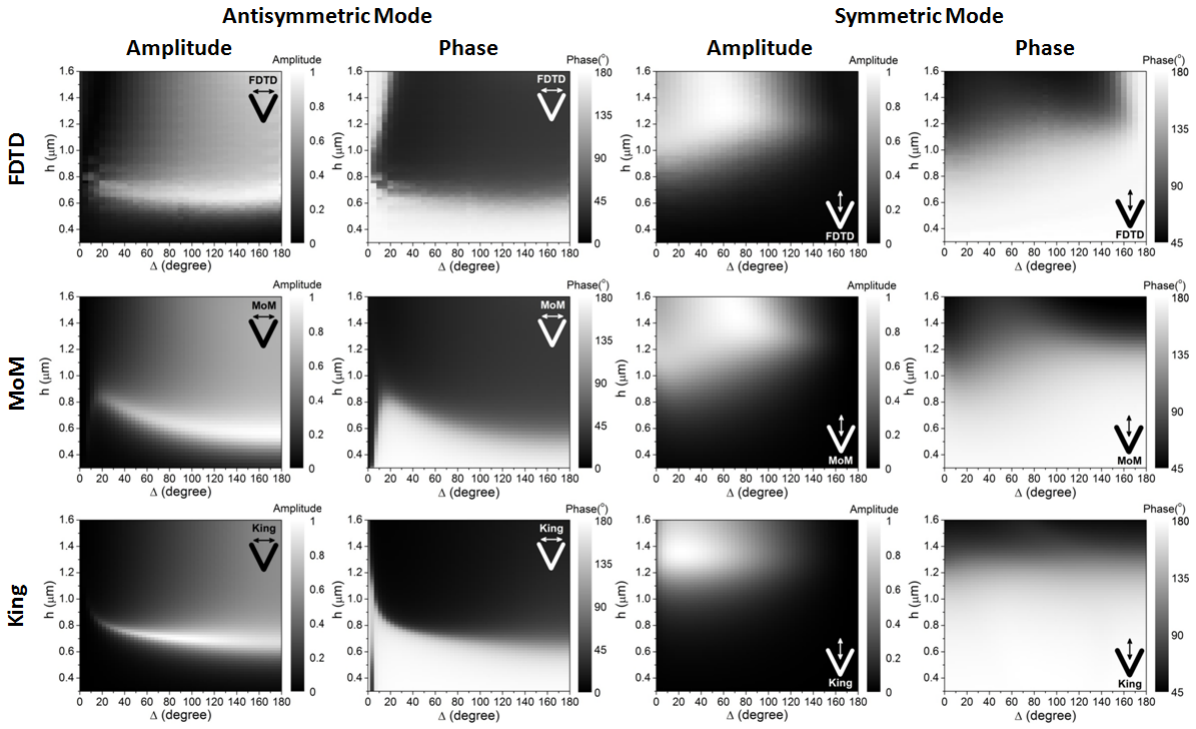

FIGURE 3.5: The first, second, and third rows are, respectively, FDTD simulations, method of momentums (MoM) calculations, and calculations following King's iteration method of the amplitude and phase responses of V-antennas. The first and third columns are the amplitudes of the scattered light ($|E|$) as a function of the antenna arm length h, and the angle between the antenna arms Δ, for the antisymmetric and the symmetric modes, respectively. The second and fourth columns are the phases of the scattered light for the antisymmetric and the symmetric modes, respectively. The double arrows indicate the orientation of the two antenna modes.

Figure 3.6 shows the current distributions along the antenna as a function of arm length h for the symmetric modes with $\Delta = 45°$ and ((a) and (b)), and for the antisymmetric modes with $\Delta = 135°$ ((c) and (d)). We observe that the antenna resonances occur when the length of the antenna equals an odd integer multiple of half of the effective

wavelength, i.e., $h \approx N\lambda_o/(2n_{eff})$ for the symmetric modes, and $2h \approx N\lambda_o/(2n_{eff})$ for the antisymmetric modes, where $N = 1, 3, 5, ...$ We also observe resonances when the antenna length equals an integer multiple of the effective wavelength, i.e., $h \approx N\lambda_o/n_{eff}$, for the symmetric modes when Δ is small (Fig. 3.6(a)). In straight rod antennas, these resonances feature symmetric charge distribution (e.g., +-+) along the antenna axis and cannot be excited by plane waves [153][154]. In the case of our V-antennas, the coupling between the two arms breaks this symmetry so these resonances can be optically addressed.

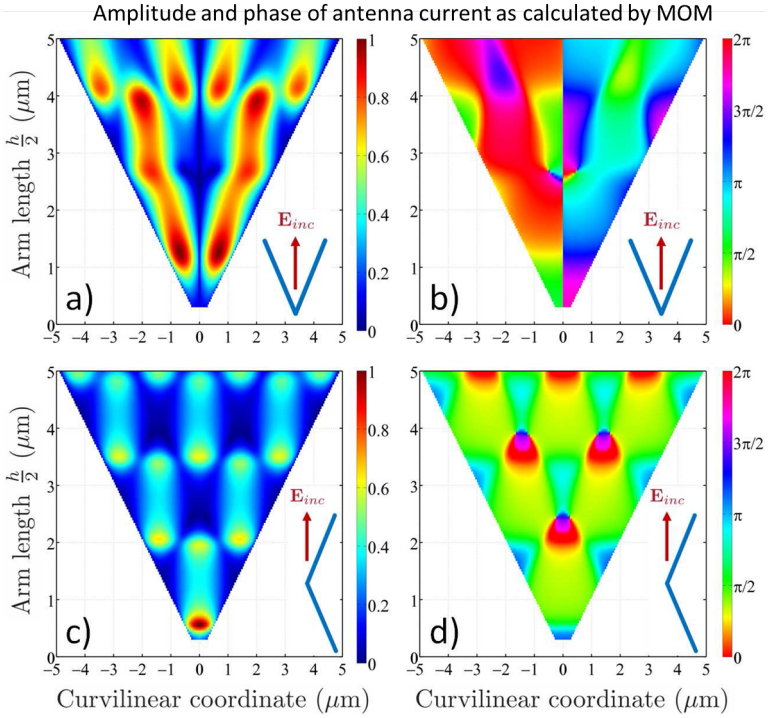

FIGURE 3.6: (a) Amplitude and (b) Phase of the current along an antenna with opening angle $\Delta = 45°$ and antenna arm length h varying from to 0.3 to 5 μm. The incident electric field is polarized along the symmetry axis. The incident wavelength is $\lambda_o = 7.7$ μm. (c) and (d) are similar to (a) and (b) for an incident electric field polarized perpendicular to the antenna symmetry axis and for an opening angle $\Delta = 135°$.

3.4 Characterization of V-shaped antennas: experiments and simulations

We characterize the spectral response of these antennas by Fourier transform infrared (FTIR) spectroscopy and numerical simulations. The gold V-shaped antennas fabricated on silicon wafers have arm length $h = 650$ nm, width $w = 130nm$, thickness $t = 60nm$, and opening angle ranging from 45° to 180° (Fig. 3.7). In Fig. 3.8, we mapped the two oscillator modes of the antennas as a function of wavelength and opening angle Δ by showing the measured (a-c) and calculated (d-f) transmission spectra. The orientation of the incident polarization is shown in the upper right corner. Figures 3.8(a) and (d) correspond to excitation of only the x-oriented symmetric antenna mode, whereas (b) and (e) correspond to the y-oriented antisymmetric mode, and (c) and (f) shows both excited modes. The spectral position of these resonances are slightly different from the first order approximation which would yield $\lambda_{\mathrm{x}} \approx 2hn_{eff} \approx 3.4$ μm and $\lambda_{\mathrm{y}} \approx 4hn_{eff} \approx 6.8$ μm, taking n_{eff} as 2.6 [15-17], with the differences attributed to the finite aspect ratio of the antennas and near-field coupling effects, which are especially strong for small Δ when the arms are in closer proximity to each other, leading to a significant resonance shift (Figs. 3.8(b) and (e)). All of the results of the experiment are reproduced very well in simulations, including the feature at 8-9 μm due to a phonon resonance in the 2-nm native silicon oxide layer on the silicon substrate, which is enhanced by the strong near fields formed around the metallic antennas. In Figs. 3.8(b), (c), (e), and (f), a higher order antenna mode is clearly visible at $\lambda_{\mathrm{o}} \approx 2.7\mu$m for large Δ.

We measured the generated cross-polarization using our FTIR setup in transmission mode, inserting a polarizer after the sample at a 90° angle to the incident polarization. The resulting spectrum for incident polarization 45° from the x-axis, normalized to the

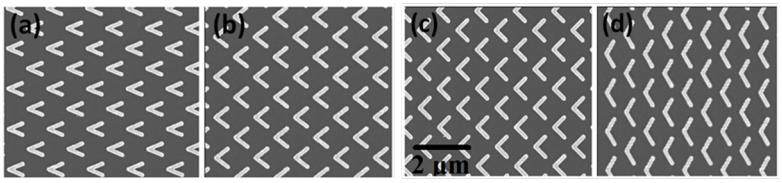

FIGURE 3.7: (a, b, c, d) SEM images of gold V-shaped antennas fabricated on a silicon substrate with opening angles $\Delta = 45°, 75°, 90°, and 120°$, respectively.

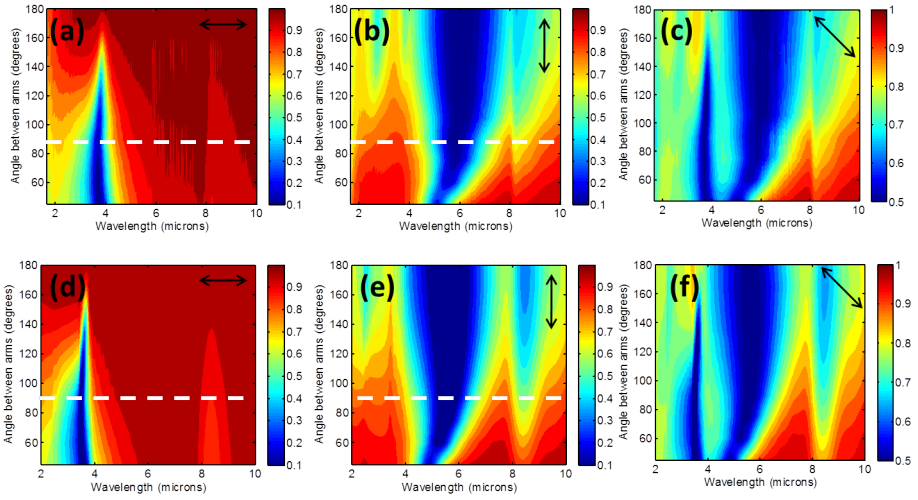

FIGURE 3.8: (a-c) Measured transmission spectra through the V-antenna arrays at normal incidence as a function of wavelength and angle Δ for fixed arm length $h = 650$ nm. The incident light is polarized (a) along the symmetry axis of the antennas, (b) perpendicular to the symmetry axis, and (c) at a 45° angle. (e-g) FDTD simulations corresponding to the experimental spectra in (a-c), respectively. The feature at δ_o =8-9 μm is due to the phonon resonance in the 2 nm SiO2 on the substrate.

light directly transmitted through the bare silicon substrate, is shown in Fig. 3.9(a). As expected, the polarization conversion peaks in the 3–8 μm range, in the vicinity of the two antenna resonances. The corresponding FDTD simulation is shown in Fig. 3.9(b), and retains the same features as the experiment, though the simulated polarization conversion spectrum is more clearly broken up into two resonances. The experimental data show less of this separation probably due to inhomogeneous broadening in the experiment due to fabrication imperfections, non-normal incident angle in our FTIR-microscope setup (the numerical aperture of our Cassegrain microscope objective is 0.4), and the limited coherence area of our thermal source.

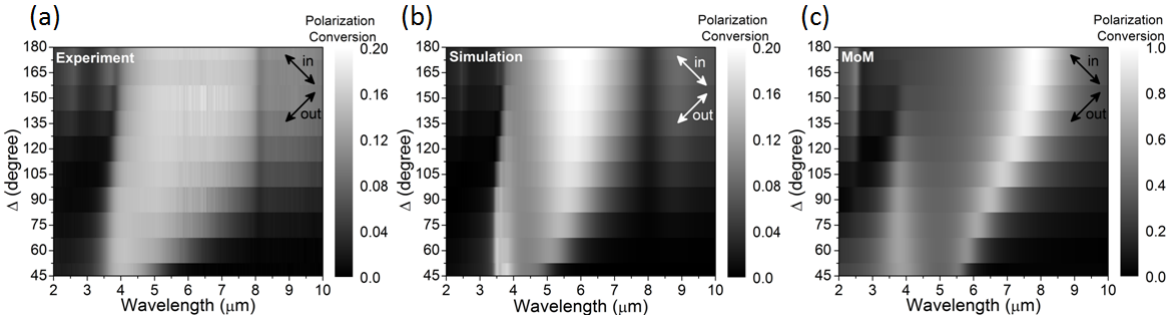

FIGURE 3.9: Experimental measurements (a), FDTD simulations (b), and MoM calculations (without considering the absorption of the SiO_2 layer on the silicon substrate) of the cross-polarized scattering for the V-antenna arrays in Fig. 3.7. The arrows indicated the polarization of the incident and output light.

3.4.1 Effects of a finite substrate

In this section we briefly discuss a subtelty that we found by carefully comparing the simulations and experimental data on the spectral response of antennas. In fact, the results of this section apply to most practical measurements of resonant plasmonic structures in the laboratory, and thus have broad implications on the field of plasmonics; surprisingly we did not find a similar discussion anywhere in the literature.

First we re-plot the data from Fig. 3.8 in Fig. 3.10 including both the color maps and line-scans, showing both the experimental and the simulation data, as well as some added details. Note that there are significant differences between the basic simulations assuming an infinite substrate and the experimental data. In fact, in the experiment a finite, 280 μm thick double-side polished silicon substrate is used; however, it is computationally intensive to include this large, finite slab in the simulations due to the high resolution required to model the nanoscale antennas. The polarization-conversion result shown as the black curve in Fig. 3.10(e) is a result of such a complete simulation and matches quite well the experimental measurements, but all of the other simulations presented in this article are performed using an infinite silicon substrate.

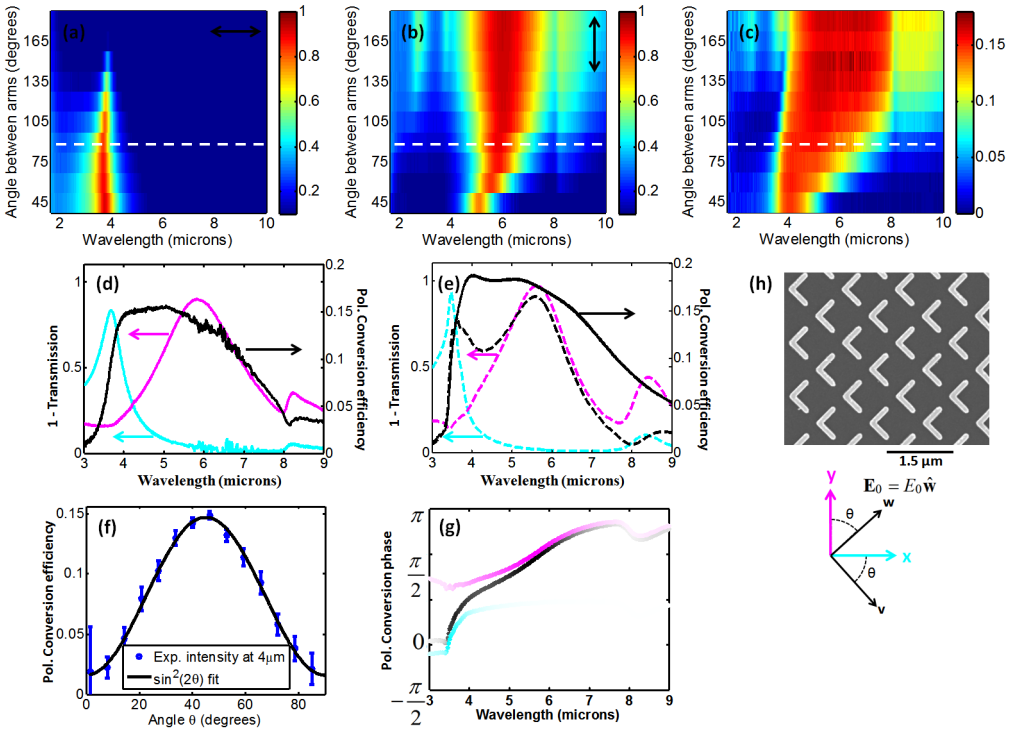

FIGURE 3.10: (a, b). Color maps showing the measured extinction (defined as 1 - Transmission) spectra through arrays of lithographically-defined V-antennas ($L \approx 650$ nm, Δ from 45° to 180°) for x- and y-oriented incident polarizations, respectively. (c). Color map showing the polarization conversion efficiency spectra corresponding to (a, b) when the incident field is polarized at a $\theta = 45°$ angle between both principle axes. (d). Blue and pink curves are the measured extinction through the V-antenna array with $\Delta = 90°$ for the x-oriented (blue) and y-oriented (pink) incident polarization for every antenna. The black curve is the polarization conversion efficiency from the array for $\theta = 45°$. All three curves correspond to line scans of (a-c), shown by the white dashed line. (e). FDTD simulations corresponding to the curves in (d), with the dashed curves representing simulations with an infinitely thick substrate and the solid black curve representing the calculated polarization-conversion efficiency when the finite (280 μm) thickness of the substrate is accounted for. (f). Measured polarization conversion efficiency at $\lambda = 4$ μm plotted vs. the incident polarization angle θ (blue symbols) and a fit to a $\sin^2(2\theta)$ dependence as predicted by Eqn. 3.10. The calculated correlation R is 0.997. (g). Phase response of the cross-polarized light generated by the antennas as calculated by FDTD (black). The blue and pink curves represent the phases of the contributions from the symmetric and antisymmetric modes, respectively. Brightness of the phase curves indicates the intensity of the scattered light. (h). SEM image of the $\Delta = 90°$ V-antenna array and the coordinate system.

The finite extent of the substrate in the experiment significantly changes the spectrum of our metallic nanostructures. Because light can be reflected from both interfaces of the silicon wafer, a Fabry-Perot-type cavity is formed within the wafer, and the light which is trapped within this cavity affects the scattered fields from the antennas.

It is possible to account for this effect in FDTD simulations by simply introducing the finite substrate into the geometry. However, due to the differences in scale between the antennas (tens to hundreds of nanometers) and the substrate thickness (hundreds of microns), these simulations are exceptionally time- and resource-consuming. As a result, it is impractical to replace all of the simulations in Figs 3.8 and 3.10 with ones taking into account the finite substrate. Instead, we performed one such simulation to correct the simulated spectrum of Fig. 3.10(e) and demonstrate how the substrate generally alters the spectrum of our antennas.

The resulting polarization-conversion spectrum is re-plotted in Fig. 3.11(a). The main effect of the substrate is the broadening of the antenna resonances and the washing out of the dip in the polarization-conversion spectrum. In principle this effect can be beneficial because it increases the effective bandwidth of our antennas, and can be explained as follows.

A substrate with finite thickness behaves as a Fabry-Perot resonator, which enhances the scattering efficiency of the antennas into the air side by feeding back some of the energy which would have otherwise been scattered away into the substrate side. In proximity of the resonance frequency of antennas, the scattering by the antennas is maximized, and since it is a loss channel for the Fabry-Perot resonator, the intensity build-up within the substrate is minimized. Therefore, the scattering enhancement into the air provided by the Fabry-Perot modes is also minimized. At frequencies away from the antenna

resonances the scattering cross-section of the antennas decreases, allowing more energy to be stored in the substrate. Consequently, this provides a larger enhancement to scattering from the antennas.

This effect serves to flatten out the scattering spectrum of our antennas, washing out features such as the dip around 4.5 μm expected in presence of an infinite substrate (Fig. 3.11(a)). In the simulated spectrum that takes into account the effect of finite substrate thickness (Fig 3.11(a) black curve), the Fabry-Perot fringes have been low-pass filtered to reproduce the effect of the finite numerical aperture (0.4) of the objective in the experimental setup, along with the finite spectral resolution of the measurement. Due to the large order of the cavity (the thickness is much larger than the wavelength), small numerical apertures are sufficient to filter out most of the Fabry-Perot fringes. However, low-pass filtering does not eliminate the overall scattering enhancement provided by the Fabry-Perot modes. As shown in Fig. 3.10, this calculated spectrum matches well with the experimental data. For completeness, we show in Fig. 3.11(b) the expected spectrum for zero numerical aperture, where the Fabry-Perot fringes are shown, as well as the spectrum normalized to the average intensity (Fig. 3.11(c)), which shows that the energy density inside slab (represented by the relative amplitude of the Fabry-Perot fringes) is minimized in the vicinity of the antenna resonances.

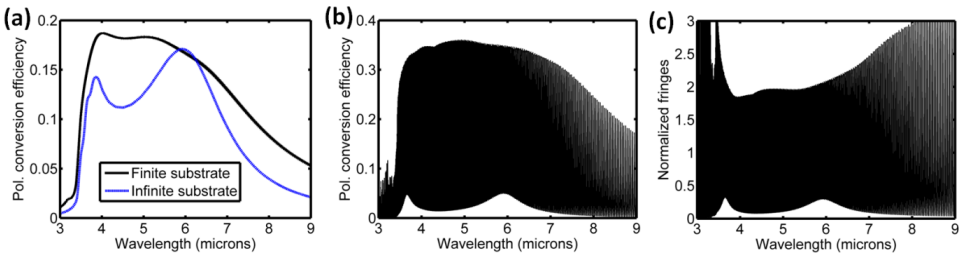

FIGURE 3.11: (a) Polarization conversion spectrum from a V-antenna array (reproduced from Fig. 3.10(e)) as calculated by FDTD with a 280 μm-thick substrate (black) and an infinite substrate (blue). The finite substrate curve was smoothed with a low-pass filter. (b) Raw polarization conversion spectrum from the simulation without the filter. (c) The curve in (b) divided by its low-pass-filtered version which shows the relative amplitude of the fringes.

3.5 Generalized laws of reflection and refraction

3.5.1 Anomalous reflection and refraction

In this section, we show a dramatic demonstrations of controlling light using the tunable phase shift between the emitted and incident radiation of optical resonators; that is, a linear phase variation along an interface introduced by an array of phased optical antennas leads to anomalously reflected and refracted beams in accordance with generalized laws of reflection and refraction.

The path that light takes as it propagates through a medium can be predicted by Fermat's principle, which states that the trajectory taken between two points A and B by a ray of light is that of least optical path, $\int_A^B n(\vec{r})dr$, where $n(\vec{r})$is the local index of refraction. Light chooses this least path from point A to B because it lies at an extremum, where the derivative of the optical path length, or equivalently the accumulated optical phase $\int_A^B d\varphi(\vec{r}) = \int_A^B k_o n(\vec{r})dr$, with respect to infinitesimal variation of the path is zero. Light waves that stay close to this variationally stable path arrive at their destination with nearly the same phase and therefore interfere constructively, whereas all other paths interfere destructively. In this sense, Fermat's principle can be stated as the principle of stationary phase [1][155][156], which is actually the most general and applicable form of Fermat's principle (on the other hand the weaker form of Fermat's principle, the principle of least time, can not properly predict all of the light paths for certain simple situations such as light reflecting off a mirror). Now suppose an abrupt, spatially varying phase shift $\Phi(\vec{r}_s)$ is introduced in the optical path by suitably engineering the interface between two media, which depends on the coordinate $\vec{r}_s$ along the interface. If we then apply Fermat's principle of stationary phase, then the total phase shift $\Phi(\vec{r}_s) + \int_A^B k_o n(\vec{r})dr$ must be stationary for the actual path that light takes. As a result, the reflected and

refracted paths may no longer be the same as that of the interface without these phase discontinuities.

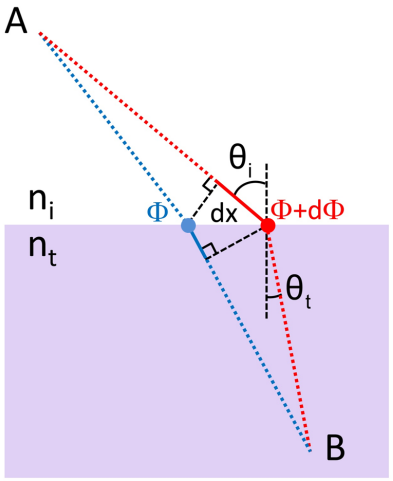

FIGURE 3.12: Schematics used to derive the generalized Snell's law of refraction. The interface between the two media is artificially structured in order to introduce an abrupt phase shift in the light path, which is a function of the position along the interface. Φ and Φ+dΦ are the phase shifts where the two paths cross the boundary.

Consider an incident plane wave at an angle θ_i. Assuming that the two paths are infinitesimally close to the actual path that light takes (Fig. 3.12), then the phase difference between them is zero such that

$$[k_o n_i \sin(\theta_i)\, dx + (\Phi + d\Phi)] - [k_o n_t \sin(\theta_t)\, dx + \Phi] = 0 \tag{3.11}$$

where θ_t is the angle of refraction, Φ and Φ+dΦ are, respectively, the phase shifts at the locations where the two paths cross the interface, dx is the distance between the intersections, n_i and n_t are the refractive indices of the two media. If the phase gradient along the interface is designed to be constant, the previous equation leads to the generalized law of refraction (i.e. a generalized Snell's law)

$$\sin(\theta_t)\, n_t - \sin(\theta_i)\, n_i = \frac{\lambda_o}{2\pi}\frac{d\Phi}{dx} \tag{3.12}$$

Equation (3.12) implies that the refracted ray can have an arbitrary direction, provided that a suitable constant gradient of phase discontinuity along the interface ($d\Phi/dx$) is introduced. Because of the non-zero phase gradient in this modified Snell's law, the two angles of incidence $\pm\theta_i$ lead to different values for the angle of refraction. As a consequence, there are two possible critical angles for total internal reflection, provided that $n_t < n_i$

$$\theta_c = \arcsin\left(\pm\frac{n_t}{n_i} - \frac{\lambda_o}{2\pi n_i}\frac{d\Phi}{dx}\right) \tag{3.13}$$

Similarly, for the reflected light we have

$$\sin(\theta_r) - \sin(\theta_i) = \frac{\lambda_o}{2\pi n_i}\frac{d\Phi}{dx} \tag{3.14}$$

where θ_r is the angle of reflection. There is a nonlinear relation between θ_r and θ_i, which is dramatically different from conventional specular reflection. Equation (3.14) predicts that there is always a critical incidence angle

$$\theta_c' = \arcsin\left(1 - \frac{\lambda_o}{2\pi n_i}\left|\frac{d\Phi}{dx}\right|\right) \tag{3.15}$$

above which the reflected beam becomes evanescent.

As shown in previous sections, the phase shift between the scattered and the incident radiation of an optical antenna changes across a resonance. By tailoring the geometry of the antennas and hence their phase response as a function of position on the interface, one can introduce a linear phase shift along the interface and thus mold the wavefront of the reflected and refracted beams in nearly arbitrary ways. The spacing between the antennas in the array should be sub-wavelength to provide efficient scattering and to

prevent the apperance of multiple diffraction orders. However this spacing should simultaneously not be so small that strong near-field coupling between neighboring antennas would perturb their phase responses (in general one could also make strongly coupled antennas and properly engineer their near-field coupling such that the spatially varying phase is still maintained, but this is a much more difficult design problem). Note that due to the discreteness in our approach to approximate the linear phase distribution, in general there will always be regularly reflected and refracted beams, which follow conventional laws of reflection and refraction (i.e., $d\Phi/dx=0$ in Eqs. (3.12) and (3.14)). The antenna packing density controls the relative amount of energy in the anomalously reflected and refracted beams.

Figure 3.13 shows the amplitude and phase responses of gold V-antennas calculated using the previously discussed analytical iteration method. The antenna symmetry axis is along 45° direction so that both the symmetric and antisymmetric plasmonic modes are excited, given a vertical incident polarization (Fig. 3.13(a) inset). As a result of the modal properties of the V-antennas and the degrees of freedom in choosing antenna geometry (h and Δ), the cross-polarized scattered light can have a large range of amplitudes and phases for our chosen wavelength $\lambda_o = 8$ μm. We chose four antennas indicated by circles in Fig. 3.13, which provide an incremental phase of $\pi/4$ from left to right and almost equal scattering amplitudes for the cross-polarized scattered light.

Phase shifts covering the entire 0-to-2π range are needed to provide full control of the wavefront. We take the mirror structure (Fig. 3.14(a) lower panel) of an existing V-antenna (Fig. 3.14(a) upper panel) (or rotate the original antennas clock-wise by 90°) so that the cross-polarized emission has an additional π phase shift. This is evident by observing that the currents leading to cross-polarized radiation are π out of phase in the two panels of Fig. 3.14(a). A set of eight antennas are thus created from the initial

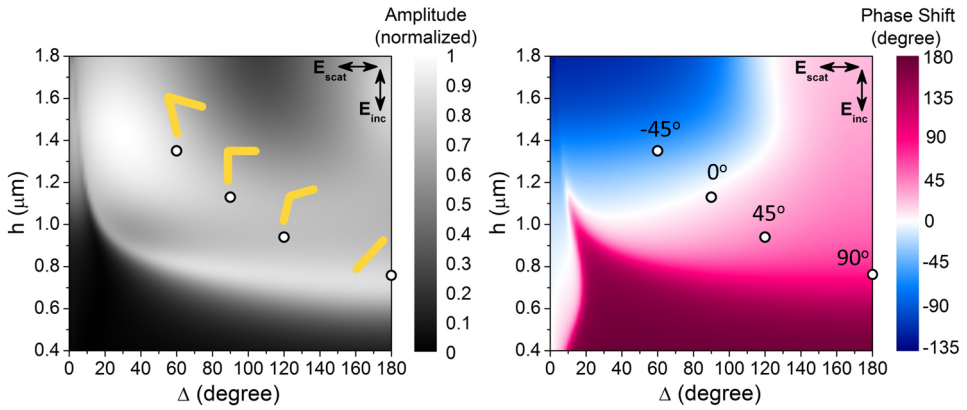

FIGURE 3.13: Analytically calculated amplitude and phase shift of the cross-polarized scattered light for gold V-antennas at $\lambda_o = 8$ μm. The four circles in the figures indicate the values of h and Δ used in experiments.

four antennas shown in Fig. 3.13, and by periodically arranging these eight antennas we created metasurfaces that can imprint a linear phase shift to the optical wavefronts. A representative fabricated sample with the densest packing of antennas is shown in Fig. 3.14(b). FDTD simulations confirm that the amplitudes of the cross-polarized radiation scattered by the eight antennas are nearly equal with phases in $\pi/4$ increments (Fig. 3.14(c)). The periodic antenna arrangement is used here for convenience, but is not necessary to satisfy the generalized laws of reflection and refraction. It is only necessary that the phase gradient is constant along the plasmonic interface and that the scattering amplitudes of the antennas are all equal. The phase increments between nearest neighbors do not need to be constant, if one relaxes the unnecessary constraint of equal spacing between nearest antennas.

We used a setup illustrated in Fig. 3.15(a) to demonstrate the generalized laws of reflection and refraction. Large arrays (230 μm by 230 μm) like the one shown in Fig. 3.14(b) were fabricated to accommodate the size of the plane-wave-like excitation (beam radius of approximately 100 μm). Figure 3.15(b) summarizes the experimental results showing ordinary and anomalous refraction for six samples with different Γ at normal incidence. The sample with the smaller Γ corresponds to a larger phase gradient and more efficient

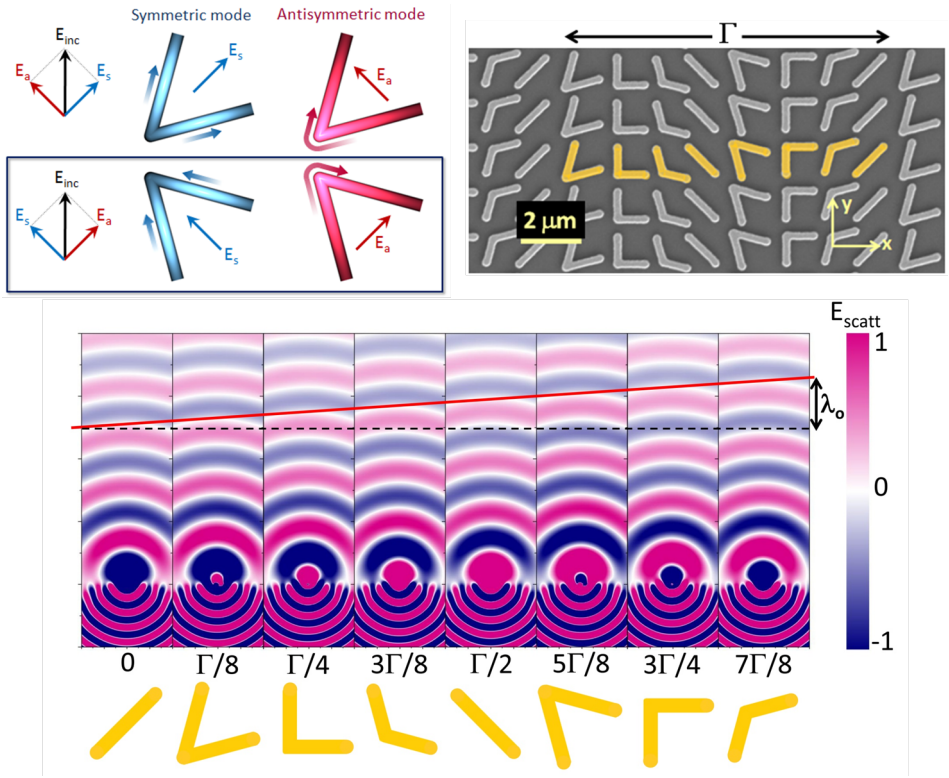

FIGURE 3.14: (a) V-antennas (upper panel) and their mirror structures (lower panel). The horizontal components of the scattered electric field in the two cases have a π phase difference. (b) SEM image of a metasurface consisting of a phased optical antenna array fabricated on a silicon wafer. The metasurface can introduce a linear phase distribution along the interface and is used to demonstrate the generalized laws of reflection and refraction. The unit cell of the structure (highlighted) comprises eight gold V-antennas of width of approximately 220 nm and thickness of approximately 50 nm and it repeats with a periodicity of $\Gamma = 11\mu$m in the x-direction and 1.5μm in the y-direction. The antennas are designed to have equal scattering amplitudes and constant phase difference $\Delta\Phi = \pi/4$ between neighbors. (c) FDTD simulations of the scattered electric field for the individual antennas composing the unit cell. Plots show the scattered electric field polarized in the x-direction for y-polarized plane wave excitation at normal incidence from the silicon substrate. The silicon substrate is located at $z \leq 0$. The antennas are equally spaced at a sub-wavelength separation $\Gamma/8$, where Γ is the unit cell length. The tilted white straight line is the envelope of the projection on the x-z plane of the spherical waves scattered by the antennas. On account of Huygens's principle, the anomalously refracted beam resulting from the superposition of these spherical waves is then a plane wave that satisfies the generalized law of refraction (Eq. (3.12)) with a phase gradient $|d\Phi dx| = 2\pi/\Gamma$ along the interface.

light scattering into the cross-polarized anomalous beams. We observed that the angles of anomalous refraction agree well with theoretical prediction (Fig. 3.15(b))

$$\theta_{t,\perp} = \arcsin\left[n_{Si}\sin(\theta_i) - \lambda_o/\Gamma\right] \tag{3.16}$$

which is obtained by substituting into Eq. (3.12) $-2\pi/\Gamma$ for $d\Phi/dx$ and the refractive indices of silicon and air (n_{Si} and 1) for n_i and n_t. Our FDTD simulations indicate that the scattering cross sections σ_{scat} of the antennas range from 0.7 to 2.5 μm^2, which is comparable to or smaller than the average area each antenna occupies, σ_{aver} (i.e., the total area of the array divided by the number of antennas). Therefore, it is reasonable to assume that near-field coupling between antennas will introduce only small deviations from the response of isolated antennas. Simulations also shows that the absorption cross-sections σ_{abs} are 5-7 times smaller than σ_{scat}, indicating relatively small Ohmic losses in the antennas at mid-infrared wavelength range.

Figures 3.15(c) and (d) show the angles of refraction and reflection, respectively, as a function of θ_i for both the silicon-air interface and the metasurface. In the range of θ_i = 0-9°, we see negative angles of refraction and reflection for the cross-polarized scattered light (schematics are shown in the lower right insets of Figs. 3.15(c) and (d)). The critical angle for total internal reflection is modified to about $-8°$ and $+27°$ for the metasurface in accordance with Eq. 3.13 compared to ± 17 degrees for the silicon-air interface; the anomalous reflection does not exist beyond $\theta_i = -57°$.

We note that antenna arrays in the microwave and millimeter-wave regime have been used for the shaping of reflected and transmitted beams in the so-called reflectarrays and transmitarrays [157] [158] [159] [160]. There is a connection between that body

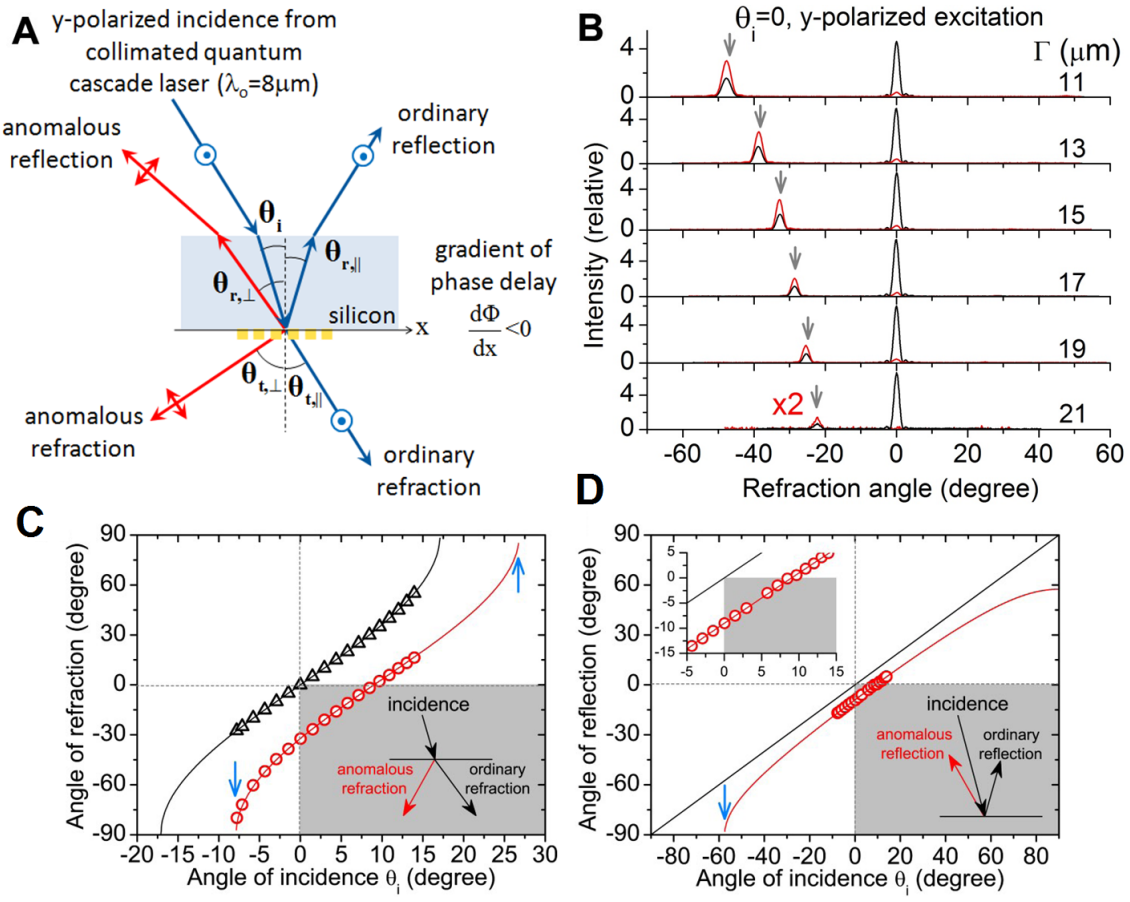

FIGURE 3.15: (a) Schematic experimental setup for y-polarized excitation (electric field normal to the plane of incidence). (b) Measured far-field intensity profiles of the refracted beams for incidence normal to the interface. The gray and black curves are measured with and without a polarizer, respectively, for six samples with different Γ. The amplitude of the gray curves is magnified by a factor of three for clarity. The polarizer is used to filter out the anomalous refraction. The arrows indicate the calculated angles of anomalous refraction according to Eq. 3.16. (c) Angle of refraction versus angle of incidence for the ordinary and anomalous for the sample with $\Gamma = 15\ \mu$m. The curves are theoretical calculations using the generalized Snell's law for refraction (Eq. (3.12)) and the symbols are experimental data. The two arrows indicate the modified critical angles for total internal reflection. The shaded region represents "negative" refraction for the cross-polarized light as illustrated in the inset. (d) Angle of reflection versus angle of incidence for the ordinary and anomalous reflection for the sample with $\Gamma = 15\ \mu$m. The upper left inset is the zoom-in view. The curves are theoretical calculations using Eq. (3.14) and the symbols are experimental data. The arrow indicates the critical incidence angle above which the anomalously reflected beam becomes evanescent. The shaded region represents "negative" reflection for the cross-polarized light as illustrated in the lower right inset.

of work and our results in that both use abrupt phase changes associated with antenna resonances. However the generalization of the laws of reflection and refraction we present is made possible by the deep-subwavelength thickness of our optical antennas and their subwavelength spacing. It is this metasurface nature of the plasmonic interface that distinguishes it from reflectarrays and transmitarrays, which typically consist of a double-layer structure separated by a dielectric spacer of finite thickness, and the spacing between the array elements is often not subwavelength.

The antenna designs in Fig. 3.14(b) are relatively broadband, i.e., they provide approximately 0-to-2π phase coverage with approximately $\pi/4$ intervals over a wide range of wavelengths. Figure 3.16(a) shows experimental results of ordinary and anomalous refraction for normally incident light with 5 different wavelengths. There are four samples with unit cell length Γ ranging from 11 μm to 17 μm, corresponding to different phase gradients. For all samples and all excitation wavelengths, we observe anomalously refracted beams away from the surface normal by an angle $-\arcsin(\lambda_o/\Gamma)$, predicted by the generalized laws. Most importantly, we see negligible intensity at $+\arcsin(\lambda_o/\Gamma)$, indicating that the interfaces operate in the "metamaterial" regime and do not function like a grating with periodicity Γ. The reason for this broadband behavior can be understood by looking at the phase responses of the 8 constituent antennas (Fig. 3.16(b)). Although the antennas were designed to generate anomalous beams at $\lambda_o = 8$ μm, their phase responses, in terms of both the total phase coverage and the incremental phase between neighbors, do not vary too much over a large range of wavelengths from $\lambda_o =$ 6 to 14 μm.

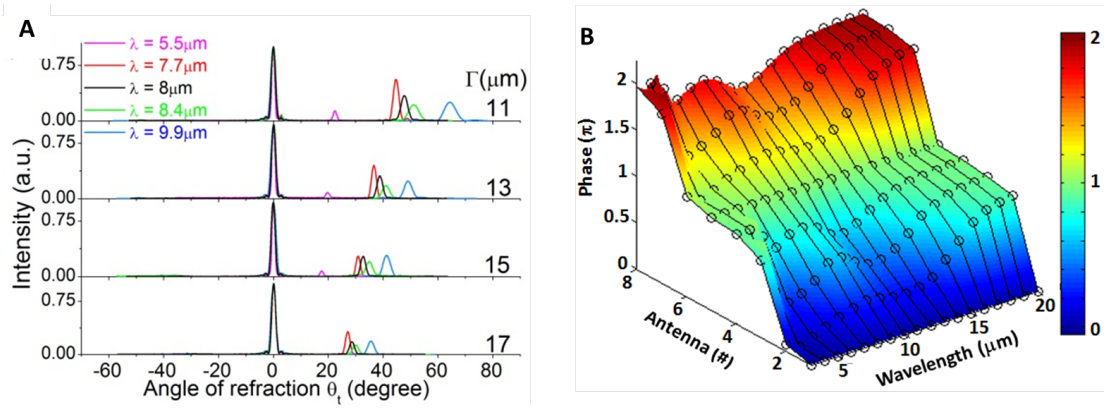

FIGURE 3.16: (a) Experimental results showing anomalous refraction ($\theta_t < 0$) from metasurfaces with various phase gradients (from $2\pi/11\mu$m to $2\pi/17$ μm) at different wavelengths (from 5.5 μm to 9.9 μm), as well as the ordinary refraction (located at $\theta_t = 0$), given normal incidence excitation. (b) FDTD simulations of the phase responses of the 8 antennas in Fig. 3.14(b) at wavelengths ranging from 4 to 20 μm. The phase response is roughly linear from 0 to 2π for wavelengths from $\lambda_o = 6$ to 14 μm. For clarity we use the phase of the first antenna as the reference and thus set it to zero.

3.5.2 Out-of-plane reflection and refraction

A feature of the conventional laws of reflection and refraction is that the incident, reflected, and transmitted beams lie in the same plane, which is usually called the plane of incidence. Recent research on metamaterials and in particular on left-handed optical materials has shown that even if light can be refracted in unusual ways, the refraction angle is still described by the traditional form of Snell's law, albeit with a negative index of refraction [161][162][163][164][165]. In this section, we derive laws of reflection and refraction in three dimensions, applicable to the case in which interfacial phase gradient does not lie in the plane of incidence, leading to reflection and refraction directions that deviate from the plane of incidence [118].

Once again we use the principle of stationary phase to derive the reflection and refraction laws, this time in three dimensions. Suppose the two paths in Fig. 3.17(a) are infinitesimally close to the actual optical path,so $\int_A \varphi(\vec{r})d\vec{r} = \int_B \varphi(\vec{r})d\vec{r}$, where the integrals are along the paths through point A and B on the interface, respectively. The equation can

be rewritten as

$$\left(\int_{P_i}^{A} \vec{k}_i \cdot d\vec{r} - \int_{P_i}^{B} \vec{k}_i \cdot d\vec{r}\right) + \left(\int_{A}^{P_t} \vec{k}_t \cdot d\vec{r} - \int_{B}^{P_t} \vec{k}_t \cdot d\vec{r}\right) + \frac{d\vec{\Phi}}{dr} \cdot (\vec{r}_A - \vec{r}_B) = 0 \quad (3.17)$$

where $\vec{k}_i$ ($\vec{k}_t$) is the wavevector of light in the medium of index n_i (n_t) and $\vec{r}_A$ ($\vec{r}_B$) is the position of A (B) on the x-y plane. For constant phase gradients, the accumulated phase of rays intersecting the interface is a convex downward function for all values of x and y [16], so we can rewrite the stationary phase condition in Eq. 3.17 for the x and y spatial coordinates independently

$$\begin{cases} k_{x,t} = k_{x,i} + \frac{d\Phi}{dx} \\ k_{y,t} = k_{y,i} + \frac{d\Phi}{dy} \end{cases} \quad (3.18)$$

By considering two infinitesimally close paths separating two points located in the same medium one can immediately see that a similar equation holds for the wavevector components $k_{x,r}$ and $k_{y,r}$ of the reflected beam. Note that due to the lack of translational invariance along the interface the tangential wavevector of the incident photon (and hence the Minkowski photon momentum [166]) is not conserved; the interface contributes an additional "phase matching" term equal to the phase gradient.

Without loss of generality, we choose a coordinate system such that $\vec{k}_i$ lies in the yz-plane (the plane of incidence), i.e., $k_{x,i} = 0$ (Fig. 3.17(b)). Equation (3.17) shows that an interfacial phase gradient with a component oriented along the x-direction leads to an x-component for both $\vec{k}_r$ and $\vec{k}_t$. It is therefore no longer possible to define a single plane that contains the incident, reflected and transmitted beams. The usual planar k-space representation used to illustrate refraction and reflection needs to be extended into three dimensions (as depicted in Fig. 3.17(b)). The angle of reflection (refraction) is now given

by the wavevector that satisfies the tangential wavevector relation (Fig. 3.17(c)) and intersects the k-sphere in the medium 1 (2) of radius $k = n_i k_o$ ($k = n_t k_o$). A schematic of this new physical situation is presented in Fig. 3.17(b). This 3D geometrical k-space representation is widely used to describe electron, neutron and X-ray diffraction and is known in the literature [167].

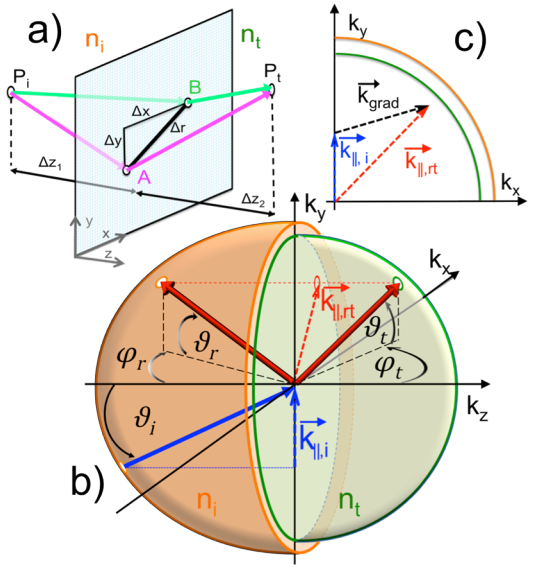

FIGURE 3.17: Schematics used to describe the generalized refraction at an interface with arbitrary orientation of the phase gradient and the associated k-space representation. (a) The interface between two media of refractive index n_i and n_t is structured to introduce a constant phase gradient $d\vec{\Phi}/dr \equiv \vec{k}_{grad}$ along the line connecting points A and B that are separated by a distance Δr. Two points, P_i and P_t are located respectively in medium 1 and 2. The difference of the phase accumulated along two paths from P_i to P_t that are infinitesimally close to the actual optical path is zero according to Fermat's principle of stationary phase. (b) and (c) The projection of the incident wave-vector on the interface $\vec{k}_{||,i}$ forms a non-zero angle with the direction of the phase gradient. As a result during the interaction with the metasurface, the light beam acquires a k-vector component parallel to the interface equal to the phase gradient ($\vec{k}_{||,rt} = \vec{k}_{||,i} + \vec{k}_{grad}$) that gives rise to the out of plane anomalously reflected and refracted beams.

The directions of the reflected and refracted wavevectors are characterized by the angles $\theta_{r(t)}$ (the angle between $\vec{k}_{r(t)}$ and its projection on the xz-plane) and $\varphi_{r(t)}$ (the angle formed by the projection of $\vec{k}_{r(t)}$ on the xz-plane and the z-axis) as defined in Fig. 3.17(b). With this choice of notation, we obtain the generalized law of reflection in 3D

$$\begin{cases} \cos\theta_r \sin\varphi_r = \frac{1}{n_i k_o}\frac{d\Phi}{dx} \\ \sin\theta_r - \sin\theta_i = \frac{1}{n_i k_o}\frac{d\Phi}{dy} \end{cases} \tag{3.19}$$

and the generalized law of refraction in 3D

$$\begin{cases} \cos\theta_t \sin\varphi_t = \frac{1}{n_t k_o}\frac{d\Phi}{dx} \\ n_t \sin\theta_t - n_i \sin\theta_i = \frac{1}{k_o}\frac{d\Phi}{dy} \end{cases} \tag{3.20}$$

Notice that when the phase gradient is oriented along the plane of incidence ($d\Phi/dx = 0$) the anomalous reflection and refraction are in plane and one recovers Eqs. (3.12) and (3.14). The nonlinear nature of these equations is such that two different critical angles now exist for both reflection and refraction. When a ray of light traverses an interface, it will propagate in the new medium as long as its longitudinal wavevector k_z remains real. This implies that the tangential components of the k-vector have to be smaller than the modulus of the k-vector in the medium. When a phase gradient along the interface provides an additional tangential component of the k-vector, the condition for the existence of a transmitted or reflected propagating beam is changed. From Eq. (3.19), we can find the condition for $k_{z,t}$ to be zero, leading to the expression for two critical angles for refraction:

$$\theta_i^{c,t} = \sin^{-1}\left[\pm\frac{1}{n_i}\sqrt{n_t^2 - \left(\frac{1}{k_o}\frac{d\Phi}{dx}\right)^2} - \frac{1}{n_i k_o}\frac{d\Phi}{dy}\right] \tag{3.21}$$

Note that a critical angle for refraction may exist even when $n_i < n_t$ for some interfacial phase gradients. For reflection, the nonlinear relation between θ_r and θ_i yields two critical angles for reflection:

$$\theta_i^{c,r} = \sin^{-1}\left[\pm\sqrt{1-\left(\frac{1}{n_i k_o}\frac{d\Phi}{dx}\right)^2} - \frac{1}{n_i k_o}\frac{d\Phi}{dy}\right] \tag{3.22}$$

We experimentally observed out-of-plane refraction in accordance with the new 3D law (Eq. (3.19)) using the same sample patterned with phased optical antenna arrays that was used in Fig. 3.14, but oriented in such a way that the interfacial phase gradient forms an angle α with respect to the plane of incidence (Fig. 3.18).

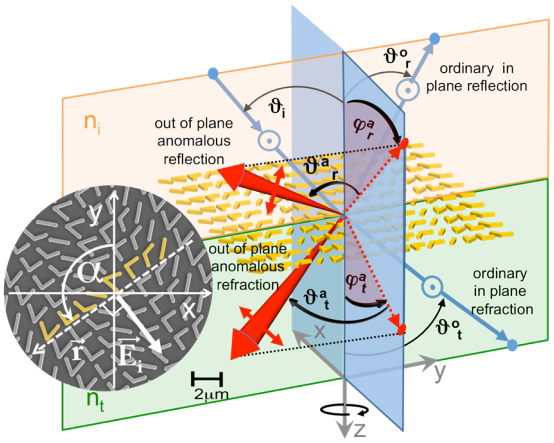

FIGURE 3.18: Schematic representation of the reflection and refraction of light in 3D. The incident light from a collimated quantum cascade laser emitting at $\lambda_o = 8$ μm impinges at an angle θ_i with respect to the z-axis on an interface between silicon and air. The incidence is from silicon and the polarization of the incident light is maintained so that it forms an angle of 45° with respect to the two plasmonic modes of the antennas. The sample is the same as that used in Fig. 3.14(b). When the interfacial phase gradient $\vec{k}_{grad}$ imposed by the V-antenna arrays is not parallel to the y-axis, a component of the phase gradient out of the plane of incidence is created, resulting in out-of-plane anomalous beams satisfying the 3D laws of reflection and refraction (Eqs. 3.18 and 3.19).

We studied both the ordinary and anomalous refraction for various incidence angles and various phase gradient orientations. The magnitude of the phase gradient is fixed to $d\Phi/dr = 2\pi/15$ (radian/μm) for all the experiments. The experimental results are summarized in Fig. 3.19(b) and unambiguously show out-of-plane refraction that agrees well with the prediction of Eq. (3.19) Figure 3.19(a) shows measured far-field intensity distribution for a phase gradient perpendicular to the plane of incidence.

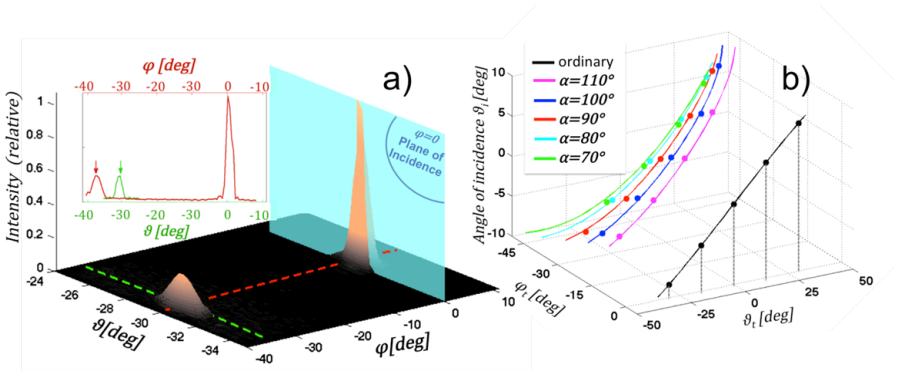

FIGURE 3.19: Experimental observation of out-of-plane refraction. (a) Measured far-field intensity as a function of the angular position of the detector θ and ϕ for a laser beam incident on the interface from the silicon side at an angle $\theta_I = -8.45°$ and for a phase gradient perpendicular to the plane of incidence. As expected, the ordinary refracted beam is in plane ($\phi = 0°$) at an angle following the conventional Snell's law, i.e. $\theta = -30°$. The anomalous beam is refracted out of plane at angles $\phi = -38°$ and $\theta = -30°$. The inset shows the angular distribution of the intensity at a fixed angle $\phi = -38°$ (green curve) and at a fixed angle $\theta = -30°$ (red curve). (b) Angles of refraction versus angles of incidence and orientations of phase gradient α. The black line is the theoretical curve from the conventional Snell law. Colored lines are theoretical curves from the 3D Snell's law (Eq. (3.19)) for different phase gradient orientations. Circles are experimental data.

In summary, three-dimensional laws of reflection and refraction are derived for optically thin metasurfaces that impart an abrupt phase gradient oriented at some angle with respect to the plane of incidence to the incident wavefront. Due to the tangential wavevector provided by the anisotropic interface, the incident beam and the anomalously reflected and refracted beams are in general non-coplanar and two different critical angles exist for both reflection and refraction. The beams' direction can be controlled over a wide range by varying the angle between the plane of incidence and the phase gradient. Experiments on arrays of sub-wavelength optical antennas demonstrate out-of-plane refraction in excellent agreement with the 3D Snell law, illustrating the unique beaming capabilities of metasurfaces at optical frequencies.

3.6 Giant and tunable optical birefringence

We have shown that the optical properties of V-antennas, and in general any 2D plasmonic structures that support two charge-oscillation eigenmodes, can be captured by a simple model involving two independent, orthogonally-oriented harmonic oscillators. We show in this section that metasurfaces consisting of V- and Y-shaped plasmonic antennas exhibit widely-tailorable birefringence, where the optical anisotropy can be controlled by interference between the light scattered by the two plasmonic eigenmodes of the antennas.

We studied the birefringence properties of the metasurfaces shown in Fig. 3.14(b) by changing the incident polarization at normal incidence so that the two orthogonal plasmonic modes are excited with different amplitudes, leading to a rotation of the polarization of the scattered light. Assume that the angle between the incident polarization and the x-axis is α and the symmetry axes of the 8 antenna elements are 45° away from the vertical direction (Fig. 3.20(a)). We decompose the incident electric-field into components that drive the symmetric and antisymmetric modes, respectively (i.e., parallel and perpendicular to the antenna symmetry axis), and calculate the scattered light based on the amplitude and phase responses of the two modes. Theoretical analysis shows that the scattered light contains two contributions that are polarized along the α-direction and $(90^\circ - \alpha)$-direction, respectively (Fig. 3.20(b)). The $(90^\circ - \alpha)$-polarized components of all 8 antennas have the same amplitude and incremental phase of $\pi/4$, which give rise to an anomalously refracted beam. The α-polarized components, however, do not have the same amplitude and the proper phase relation between neighboring antennas, which lead to a beam that propagates in the same direction as the ordinary refraction, as well as a small optical background over a large angular range. These birefringence properties

of the metasurface are experimentally confirmed at $\lambda_o = 8$ μm, and Figs. 3.20(c)-(g) show measured intensity of the ordinarily and the anomalously refracted beams as a function of the rotation angle of a linear polarizer located in front of the detector for different incident polarizations. The "eight" patterns in the figures indicate that both beams are linearly polarized, and that the polarizations of the ordinary and anomalous refraction are symmetric with respect to the 45° direction.

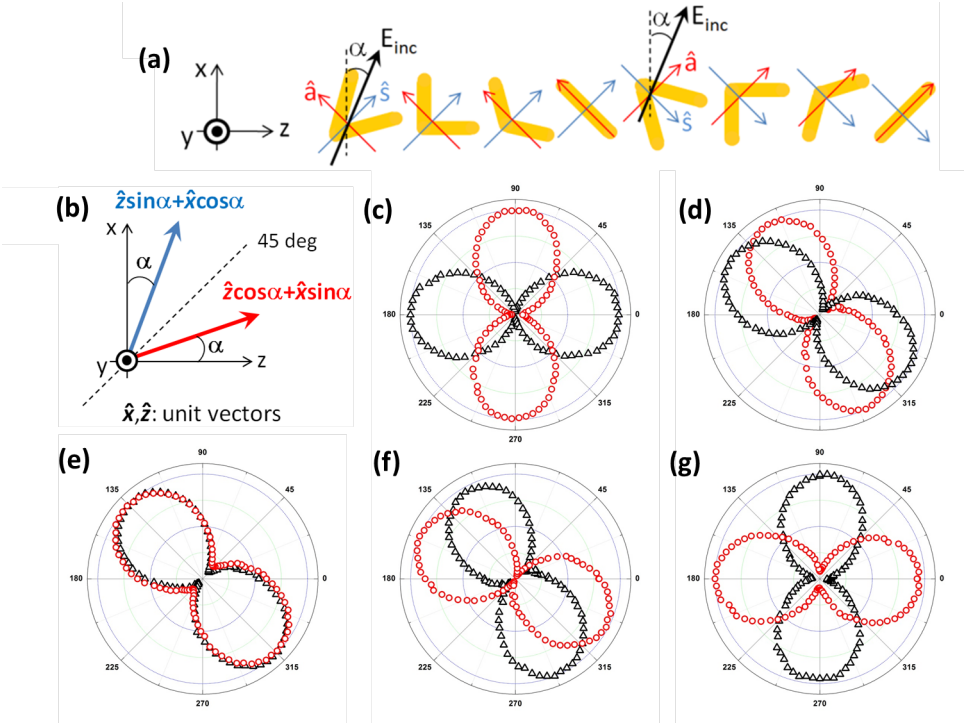

FIGURE 3.20: (a) Schematics of the 8-antenna unit cell and the incident polarization. The antenna symmetry axes, ŝ, are 45° from the vertical direction. (b) For incident polarization along the α-direction, the scattered fields from the antennas contain two components, directed along the gray and black arrows, respectively. Only the latter has the properly-engineered phase response, i.e., $\pi/4$ phase difference between neighbors, which leads to anomalously refracted beams polarized along the $(90° - \alpha)$-direction. (c)-(g) Measured intensity of the ordinarily- and anomalously-refracted beams (triangles and dots, respectively) as a function of the rotation angle of a linear polarizer located in front of a detector (α = 0, 30, 45, 60, and 90° from (c) to (g)). The free-space wavelength is 8 μm.

The spectral position of the two plasmonic modes of V-antennas can be tuned by varying the arm length h and, to a smaller extent, by adjusting the opening angle Δ (Fig. 3.13). However, both of these simultaneously shift the resonance frequencies of the symmetric and antisymmetric modes of the antenna. By appending a "tail" to the

V-antenna as shown in Fig. 3.21(a), an additional degree of freedom is attained that allows for independent tuning of the spectral position of the symmetric mode [115]. By increasing the tail length, h_T, the symmetric mode is red-shifted without affecting the antisymmetric mode. This is confirmed by mapping out the two plasmonic modes for 4 different values of h_T, by measuring the reflectivity spectra from arrays of these antennas (Figs. 3.21(b) and (c)) and by FDTD simulations (Figs. 3.21(f) and (g)).

The measured polarization conversion efficiency of the Y-antennas is plotted in Fig. 3.21(d), given incident polarization along 45° with respect to the antenna symmetry axis, such that the projections of the incident field along the two antenna modes are equal. There is a substantial amount of polarization conversion for h_T = 100, 300, and 700nm (red, black, and blue curves, respectively). However, for h_T = 500nm (green curve), the polarization conversion is almost completely extinguished. FDTD simulations (Fig. 3.21(h)) demonstrate the same behavior as in the measurements. The origin of this effect can be interpreted as destructive interference between the contributions to the cross-polarization generation from the two oscillator modes. As illustrated in Fig. 3.21(e), the incident field excites both modes of the Y-antenna, each of which contribute to the cross-polarized field. However, as shown in Fig. 3.4(b), the projections of the emission of the two modes onto the v-axis are opposite in phase, so when the two modes are nearly identical in amplitude and phase responses (as is the case for h_T = 500nm), their contributions to the polarization conversion are π out of phase, resulting in destructive interference.

To further illustrate this effect, we use the two-oscillator model developed earlier to demonstrate how the polarization conversion efficiency evolves with various parameters for the two oscillator modes. In Figs. 3.22 and 3.23 we plot the intensity and phases of light scattered into the cross-polarization by a two oscillator element following the same

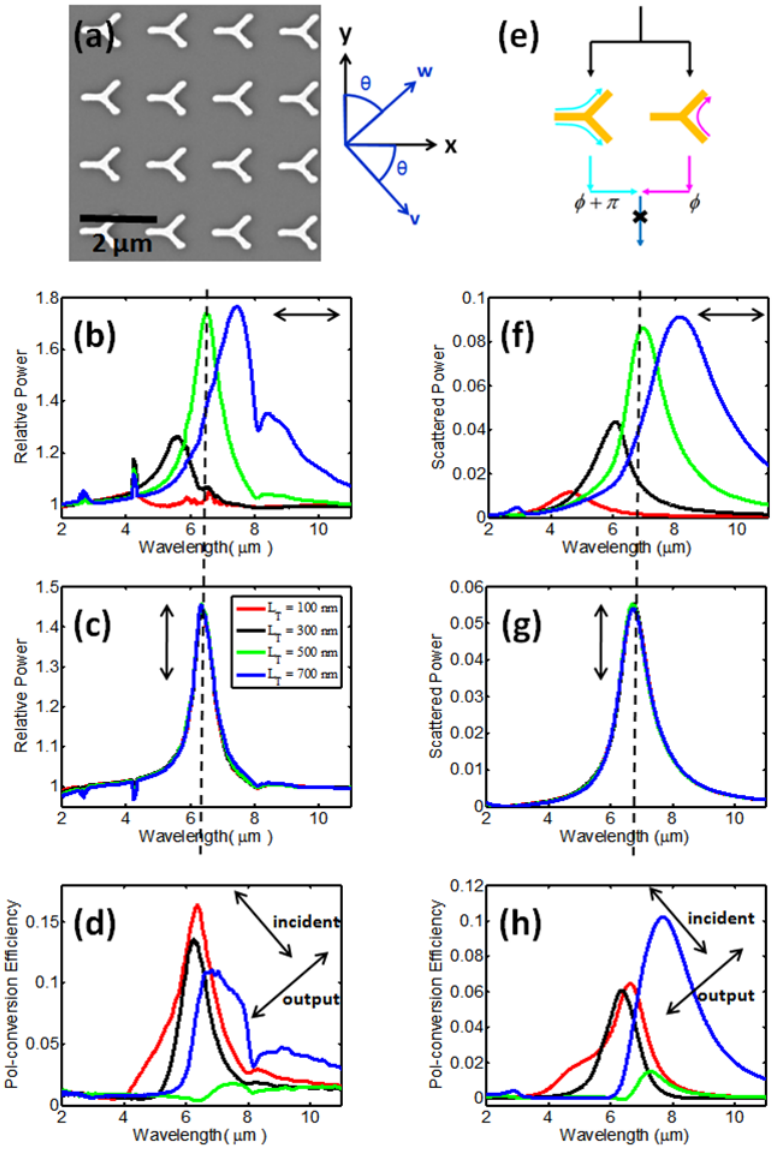

FIGURE 3.21: Y-shaped plasmonic antennas. (a) SEM image of the antenna array. (b) and (c) Measured normal-incidence reflectivity spectra of the symmetric and antisymmetric antenna modes, respectively, as a function of tail length h_T, which varies from 100 nm to 700 nm by increments of 200 nm. The reflectivity of the bare silicon substrate is approximately 0.3. The vertical dashed line shows that for $h_T = 500$nm (green curves), the two modes are overlapping. The arrows in the insets indicate the polarization of the incident field. (d) Polarization conversion spectrum with incident polarization along 45°, with the incident and measured polarizations indicated with arrows. The polarization conversion is nearly extinguished for one intermediate value of h_T (green). (e) Diagram explaining the extinguishing of polarization conversion due of destructive interference between contributions of the two antenna modes when h_T is adjusted such that the two modes have the same resonant response. (f-h) FDTD simulations corresponding to the measurements in (b-d).

convention and coordinate systems as Fig. 3.4. The blue and pink curves represent the polarization conversion intensity due to the x- and y-oriented modes, respectively, while the black curve represents the total polarization conversion intensity from the two-oscillator element, which includes the interference between the two independent contributions.

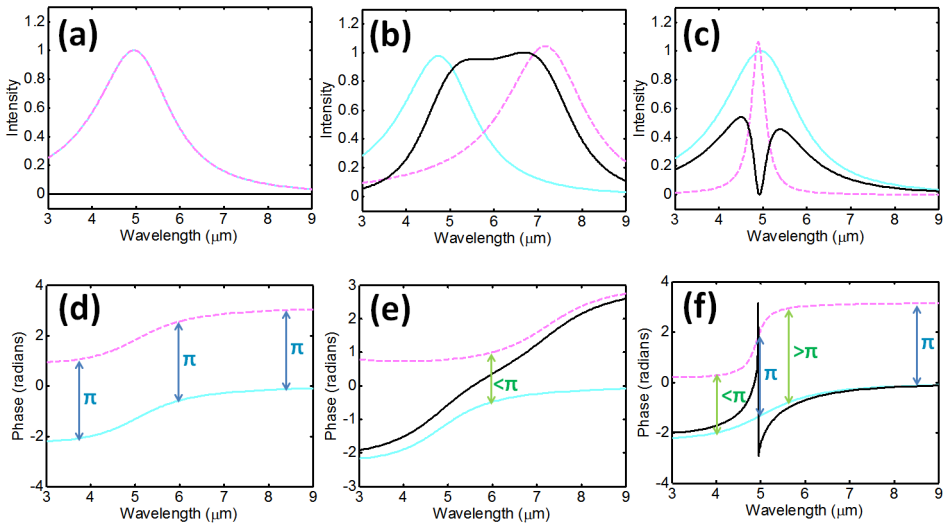

FIGURE 3.22: Polarization conversion due to the x- or y-oriented mode only (blue and pink curves, respectively, and due to both (black curve) (a). The two modes are exactly overlapping, generating no polarization conversion due to destructive interference. (b). The two modes are similar in linewidth, but have differing resonant frequencies, so some polarization conversion is seen. (c). The two modes are roughly overlapping in resonant frequency, but have very different linewidths, leading to some polarization conversion but a 0 exactly on resonance where destructive interference occurs.

In Fig. 3.22(a), we plot the polarization conversion contributions from two identical orthogonal oscillators, with resonant wavelengths around 5 μm. Note that the blue and pink curves are overlapping exactly. The phase response of these two contributions to the polarization conversion is show in Fig. 3.22(d). There is a π phase difference between the two curves across all wavelengths; this is a graphical representation of the $e^{i\pi}$ term in Eqn. 3.10 and is due to the fact that the projections of the x- and y- oscillators onto the v-axis in Fig. 3.4 are exactly out of phase. As a result, the two contributions completely destructively interfere, and therefore the total polarization conversion efficiency from the two-oscillator element is identically 0 (black curve in Fig. 3.22(a)).

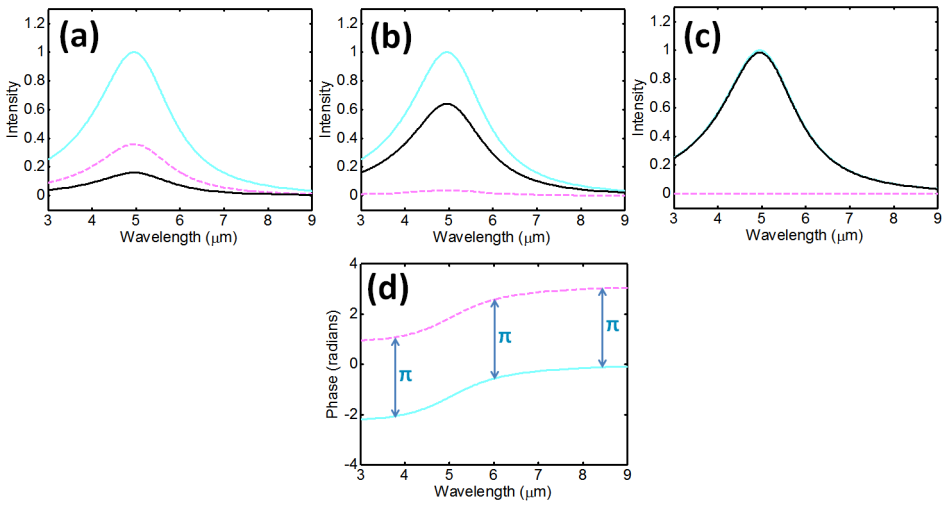

FIGURE 3.23: (a) - (c). Polarization conversion due to the x- or y-oriented mode only (blue and pink curves, respectively, and due to both (black curve). The strength of the y-oriented (pink) mode is decreased between panels (a), (b), and (c), increasing the value of the overall polarization conversion. (d). Relative phase of the contributions to the cross-polarization of the two modes.

By moving the two resonances apart (e.g. to approximately 4.5 μm and 7 μm, respectively) as in Fig. 3.22(b), the two contributions to the polarization conversion no longer destructively interfere (see 3.22(e) for the phase), and therefore there is substantial polarization conversion intensity (black curve in 3.22(b)). Note that the movement of one resonance with respect to the other can be achieved in Y-shaped antennas by varying L_T (Fig. 3.21). A similar effect is seen by keeping the two resonances roughly at the same wavelength, but changing their linewidths significantly, as in Fig. 3.22(c), such that the contributions are π out of phase at very long and very short wavelengths, and also exactly on resonance, creating the sharp dip in polarization conversion.

We further explore the relationship between the two modes and the total polarization conversion efficiency by keeping the two modes at the same resonant wavelength and with the same linewidth, only changing their relative amplitudes. As can be seen in Fig. 3.22(a), when the two modes are identical in every way, the polarization conversion efficiency is 0 at all wavelengths (black curve) due to perfect destructive interference. By decreasing the amplitude of one of the modes (pink) in Fig. 3.23(a), we obtain some

polarization conversion signal. This signal increases further and further with decreasing amplitude of the pink mode (Fig. 3.23(b)) until finally reaching the exact value of the contribution from the blue mode (Fig. 3.23(c)), since there is no longer any contribution from the pink mode. The phase response of both oscillators is plotted in Fig. 3.23(d), and is the same for (a-c). As expected, despite the π phase difference between the two curves, complete destructive interference only happens when the two amplitudes are identical (as in Fig. 3.22(a)).

In general, arrays of resonant structures which support two orthogonal plasmonic eigenmodes can be viewed as metasurfaces with large and tunable birefringence: they can rotate the polarization of light over a thickness of just tens of nanometers at infrared wavelengths, and the degree of polarization rotation is controlled by the phase and amplitude responses of the two modes. This type of birefringence in anisotropic structures is referred to as "form birefringence" in literature (see, e.g., [168][169][170][171]), though in the literature form birefringence usually involves anisotropic dielectric structures with significant thickness compared to the wavelength of light.

3.7 Vortex beams created by metasurfaces

To demonstrate the versatility of the concept of interfacial phase discontinuities, we fabricated metasurfaces capable of creating vortex beams upon illumination by normally incident linearly polarized Gaussian beams [113] [116]. Optical vortices are a peculiar type of beam which has a doughnut-like intensity profile and a helicoidally shaped wavefront [172][173]. Unlike plane waves or Gaussian beams for which the Poynting vector (or the energy flow) is parallel to the propagation direction, the Poynting vector of a vortex

beam follows a spiral trajectory around the beam axis (Fig. 3.24(a)). This circulating flow of energy gives rise to an orbital angular momentum [173].

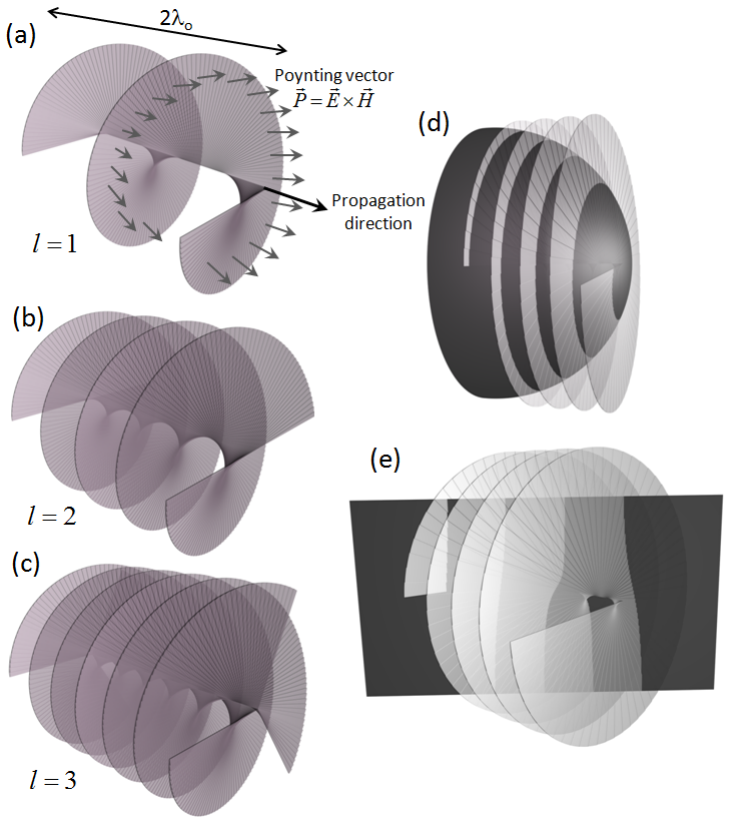

FIGURE 3.24: (a)-(c) Wavefronts of optical vortex beams with topological charge l = 1, 2, and 3; l represents the number of twists of wavefront within a wavelength. (d) and (e) show common methods for characterizing an optical vortex. One can interfere the vortex beam with a diverging or converging Gaussian beam, producing a spiral interference pattern, as demonstrated in (d) by the spiral intersection between the wavefronts of the two beams. Alternatively, one can interfere the vortex beam with a plane wave, producing an interference pattern with dislocated fringes, schematically shown in (e).

The wavefront of optical vortices has an azimuthal phase dependence, $\exp(\mathrm{i}l\theta)$, with respect to the beam axis. The number of twists, l, of the wavefront within a wavelength is called the topological charge of the beam and is related to the orbital angular momentum L of individual photons by the relationship $L = \hbar l$ [173][174], where $\hbar$ is Planck's constant. Note that the polarization state of an optical vortex is independent of its topological charge. For example, a vortex beam with $l = 1$ can be linearly polarized or circularly polarized. The wavefront of the vortex beam can be revealed by a spiral

interference pattern produced by interference of the beam with a Gaussian beam (Fig. 3.24(d)). The topological charge can be identified by the number of dislocated interference fringes when the vortex beam and a plane-wave-like beam intersect with a small angle (Fig. 3.24(e)).

Optical vortex beams profile are conventionally generated using spiral phase plates [175], spatial light modulators [176], or holograms with fork-shaped patterns [177]. This type of beam can also be directly generated by lasers as an intrinsic transverse mode [178]. Vortex beams are also important for a number of applications, such as stimulated emission depletion microscopy (STED) [179], optical trapping and manipulation [180][181], and in optical communication systems, where in some instances the quantized orbital angular momentum can carry additional information per photon [182][183].

Figure 3.25 shows the experimental setup used to generate and characterize the optical vortices. It consists of a Mach-Zehnder interferometer where the optical vortices are generated in one arm and their optical wavefronts are revealed by interference with a reference Gaussian beam propagating through the other arm. A laser beam from a distributed feedback QCL emitting monochromatic light at $\lambda_o = 7.75$ μm in continuous wave mode with power of approximately 10 mW is collimated and separated in two parts by a beam splitter. One part of the beam is rotated in polarization using a set of mirrors to serve as the reference beam. The second part is focused on a metasurface phase mask using a ZnSe lens (20-inch focal length, 1-inch diameter). The phase mask comprises a silicon-air interface decorated with a 2D array of V-shaped antennas designed and arranged so that it introduces a spiral shaped phase distribution to the scattered light cross-polarized with respect to the incident polarization. The inset SEM image of Fig. 3.25 shows the metasurface designed to generate the $l = 1$ beam. We chose a packing density of about 1 antenna per 1.5 μm^2 (approximately $\lambda_o^2/40$), to maximize

the efficiency of the device while avoiding strong near-field interactions. We estimate that about 30% of the light power impinging on the metasurfaces is transferred to the vortex beams in this setup.

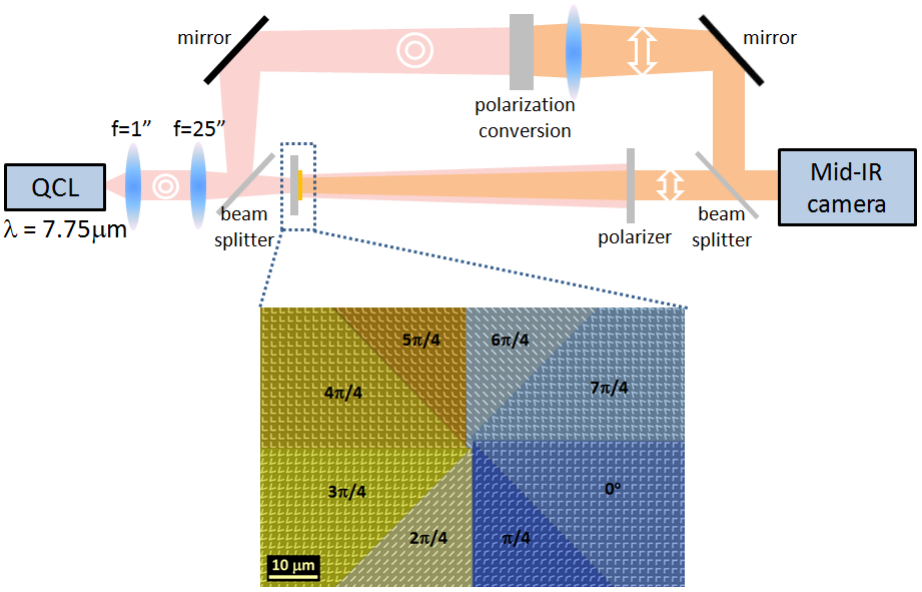

FIGURE 3.25: Experimental setup based on a Mach-Zehnder interferometer used to generate and characterize optical vortices. The bottom inset SEM image shows a metasurface phase plate with topological charge one. The plate consists of eight regions, each occupied by one of the eight elements in the unit cell in Fig. 3.14(b). The antennas are arranged to generate a phase shift that varies azimuthally from 0 to 2π, thus producing a helicoidal wavefront.

Figure 3.26(a) shows interferograms created by the interference between a plane-wave-like reference beam and the beam generated by the metasurface while the two intersect with a small angle. The dislocation at the center of the interferograms confirms the presence of a phase singularity at the core of the beam generated by the metasurface. The orientation and the number of the dislocated fringes of the interferograms can be used to characterize the sign and the topological charge L of the vortex beam.

Figure 3.27 presents FDTD simulations of the evolution of the cross-polarized scattered field after a Gaussian beam at $\lambda_o = 7.7$ μm impinges normally on a 50 by 50 μm^2 metasurface phase plate like the one shown in Fig. 3.25. We observe that a phase singularity, where the phase is undefined, is established at the center of the phase distribution as

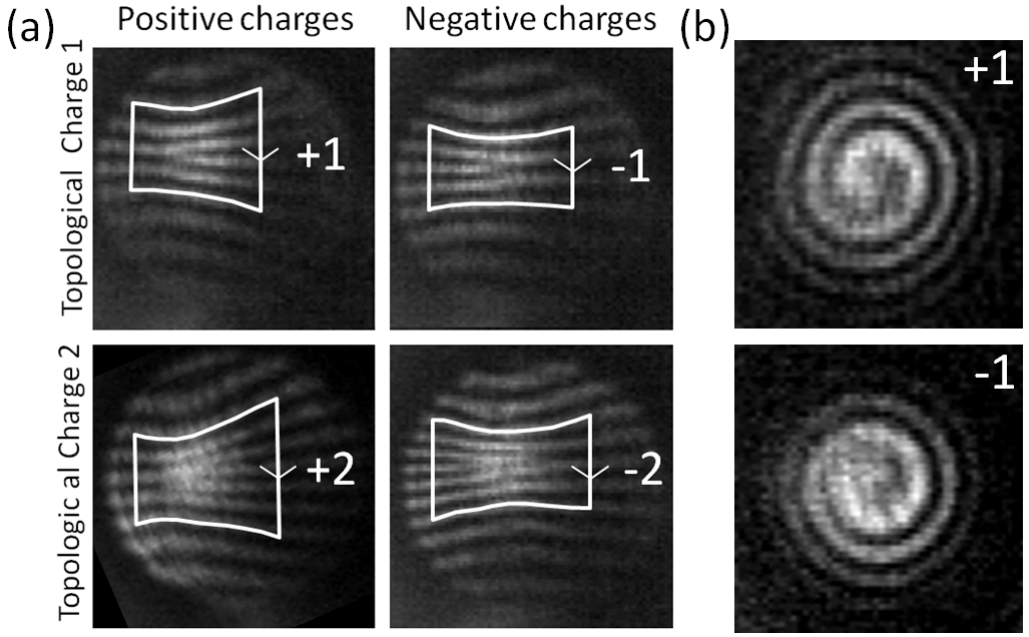

FIGURE 3.26: (a) Interferograms obtained from the interference between a plane-wave-like reference beam and optical vortices with different topological charges. The dislocation of the fringe pattern indicates the presence of a phase defect along the axis of the transmitted beam. Vortex beams with single (double) charge(s) are generated by introducing an angular distribution ranging from 0 to 2π (4π) using metasurfaces. The azimuthal direction of the angular phase distribution defines the sign of the topological charge (also called chirality). (b) Spiral interferograms created by the interference of vortex beams and a co-propagating Gaussian beam.

close as one micrometer (approximately $\lambda_o/8$) away from the interface. The presence of such phase singularity produces the characteristic zero of intensity at the beam axis less than a wavelength away from the interface. The fact that a metasurface molds the incident wavefront into an arbitrary shaped almost instantaneously presents an advantage over conventional optical components, such as liquid-crystal spatial light modulators, which are optically thick, and diffractive optics, which require observers to be in the far-field zone characterized by Fraunhofer distance $2D^2/\lambda_o$, where D is the size of the element [16].

We conducted a quantitative analysis of the generated optical vortices in term of the purity of their topological charge. The amplitude distribution of the optical vortex is obtained from the measured intensity distribution (Fig. 3.28(a)), and its phase profile

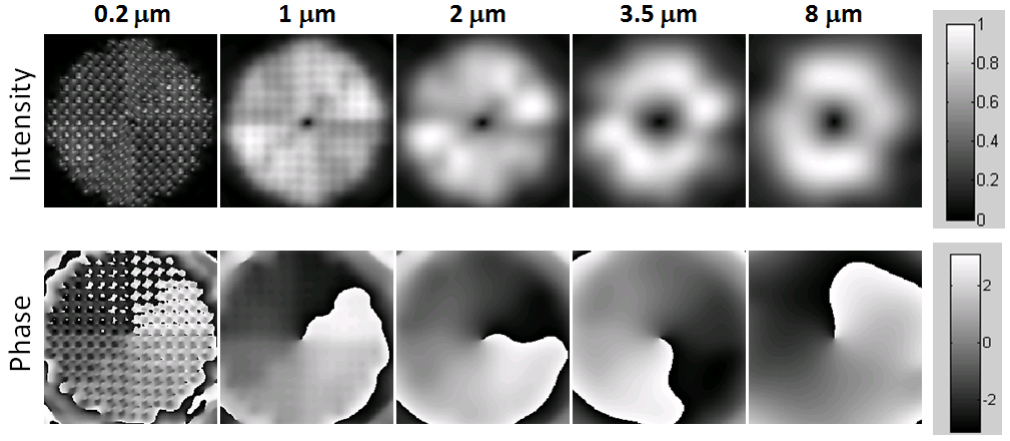

FIGURE 3.27: FDTD simulations of the cross-polarized scattered field as a function of distance from a metasurface phase plate designed to create a single charge optical vortex. The characteristic zero intensity at the center of the beam and the phase singularity develop as soon as the evanescent near-field components vanish, i.e., about 1 μm or one eighth of wavelength behind the interface.

(Fig. 3.28(c)) is obtained by the recorded interferogram (Fig. 3.28(b)). The purity of the optical vortex is calculated by decomposing its complex field on a complete basis set of optical modes with angular momentum, i.e. the Laguerre-Gaussian (LG) modes ($E^{LG}_{l,p}$) [105]. The weight of a particular LG mode in the vortex beam is given by $C^{LG}_{l,p} = \iint E_{vortex} E^{LG^*}_{l,p} dxdy$, where E_{vortex} is the complex electric field of the vortex beam, the star denotes complex conjugate, and the integers l and p are the azimuthal and radial Laguerre-Gaussian mode indices, respectively. The relative charge distribution of an optical vortex is obtained by summing all the modes with the same azimuthal index l_o, $C_{l_o} = \sum_p C^{LG}_{p,l_o}$. A histogram representing the charge distribution for our vortex beam is plotted in Fig. 3.28(d). The purity of the single charged vortex ($l = 1$) created with our technique is above 90%, similar to the purity of vortex beams obtained with conventional spatial light modulators.

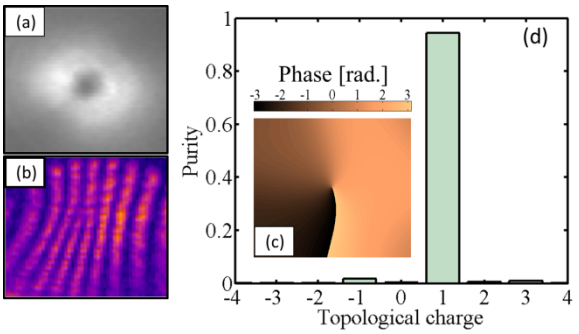

FIGURE 3.28: Analysis of the purity of the optical vortices generated by metasurface phase masks. (a) Measured doughnut-shaped intensity profile of a vortex beam with $l = 1$. (b) Measured interferogram of the vortex beam when it interferes with a plane wave. The phase profile of the vortex beam in (c) is extracted via 2D Fourier and inverse Fourier transforms of the interferogram in (b), separating the vortex and reference beam in the Fourier space. (d) Histogram representing the decomposition of the single charge vortex beam on a basis set of Laguerre-Gaussian modes with topological charge index $l_o l_0$.

3.8 Broadband metasurface wave plates

Considerable attention has been drawn to the optical properties of assemblies of anisotropic metallic and dielectric structures, which can mimic the polarization-altering characteristics of naturally-occurring birefringent and chiral media. Planar chiral metasurfaces change the polarization state of transmitted light to a limited degree [184][185][186][187][188][189]. Circular polarizers based on three-dimensional chiral metamaterials primarily pass light of circular polarization of one handedness while the transmission of light of the other handedness is suppressed [190][191]. Because of the difficulty of fabricating thick chiral metamaterials, the demonstrated suppression ratio between circular polarizations of different handedness is usually quite small (<10). One way to overcome this difficulty is to use planar structures comprising strongly-scattering anisotropic particles that are able to abruptly change the polarization of light. V-antennas are one example; other examples include arrays of identical rod or aperture metallic antennas [192][193][194][195][196] or meander-line structures [197][198]. Light scattered from such particles changes polarization because they have different spectral responses (in amplitude and phase) along the

two principle axes [199][200][201], as described in section 3.6.

Wave plates comprising identical plasmonic scatters have a number of issues. First, their performance is usually degraded by the optical background originating from direct transmission due to the finite metasurface filling factor and non-perfectly-overlapping scattering cross-sections (i.e., transmitted light not scattered or absorbed by the plasmonic structures). Second, their spectral response is limited because of the relatively narrow plasmonic resonance. For example, once a plasmonic quarter-wave plate operates away from the optimal wavelength, the ratio of scattering amplitude R between the two eigenmodes deviates from unity and their differential phase Ψ is no longer $\pi/2$, as it has to be to function as a quarter wave plate (Fig. 3.29(a)).

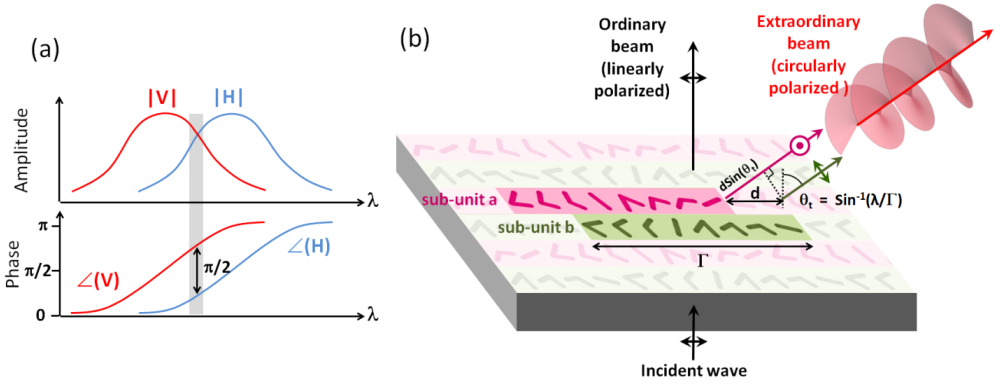

FIGURE 3.29: (a) Conventional plasmonic quarter-wave plates are based on arrays of identical anisotropic plasmonic structures that support two orthogonal plasmonic eigenmodes, **V** and **H**, which have an amplitude and phase response characteristic of any resonance (red and blue curves). The devices operate as quarter-wave plates only within a narrow wavelength range (gray area) in which the two eigenmodes have approximately equal scattering amplitudes and a phase difference of $\Psi = \pi/2$. The design also suffers from the presence of a background, which occurs because the scattered light from plasmonic structures is not spatially separated from the directly transmitted light. (b) To circumvent the problems of optical background and narrow bandwidth, we use a different design based on optical antenna metasurfaces. The unit cell of the metasurface consists of two sub-units (purple and green) each containing eight gold V-shaped antennas. Upon excitation by linearly polarized incident light, the sub-units generate two co-propagating subwaves with equal amplitudes, orthogonal linear polarization states, and a $\pi/2$ phase difference (when offset d = $\Gamma/4$), producing a circularly polarized extraordinary beam that bends away from the surface normal. The amplitudes of the subwaves are equal because corresponding antennas in the sub-units have the same geometries (i.e., arm length and opening angle); the orthogonal polarizations are ensured by different antenna orientations in the sub-units; the $\pi/2$ phase difference is introduced by the offset, d, between the sub-units. The metasurface also generates an ordinary beam propagating normal to the surface and polarized in the same way as the incident light.

In this section we describe metasurfaces based on phased optical antenna arrays that can generate scattered light waves with arbitrary polarization states. In particular, we demonstrated a quarter-wave plate that features ultra-broadband and background free performance, and works for any orientation of the incident linear polarization. The present design builds upon the work in the previous sections, in which it is demonstrated that phased optical antenna arrays can design arbitrary linearly-polarized wavefronts.

The schematic of our metasurface quarter-wave plate is shown in Fig. 3.29(b). The unit cell consists of two sub-units (purple and green in Fig. 3.29(b)), which generate two co-propagating subwaves with equal amplitude, orthogonal polarization, and a $\pi/2$ phase difference from an incident beam with linear polarization. The subwaves coherently interfere, producing a circularly polarized extraordinary beam that bends away from the propagation direction of the background, that is, the ordinary beam (Fig. 3.29(b)). Due to the spatial separation of the two beams, the extraordinary beam is background free. Our quarter-wave plate performs well over a much larger wavelength range compared to existing designs for two reasons. First, the optical response of the V-antennas has a broader effective resonance over which the antenna scattering efficiency is significant and the phase response is approximately linear (Figs. 3.30(a) and (b)). This broadened effective resonance is a result of the combined responses of the two eigenmodes of the V-antennas. Second, our metasurfaces are robust against wavelength change because we use a "balanced" design featuring two sub-units in one unit cell. Away from the optimal operating wavelength, the phase and amplitude responses of the antenna arrays will deviate from their designed values (Figs. 3.30(c) and (d)); nevertheless, the two subwaves have the same wavefronts (Figs. 3.30(c) and (d)) so they always contribute equally to the extraordinary beam, resulting in a pure circular polarization state.

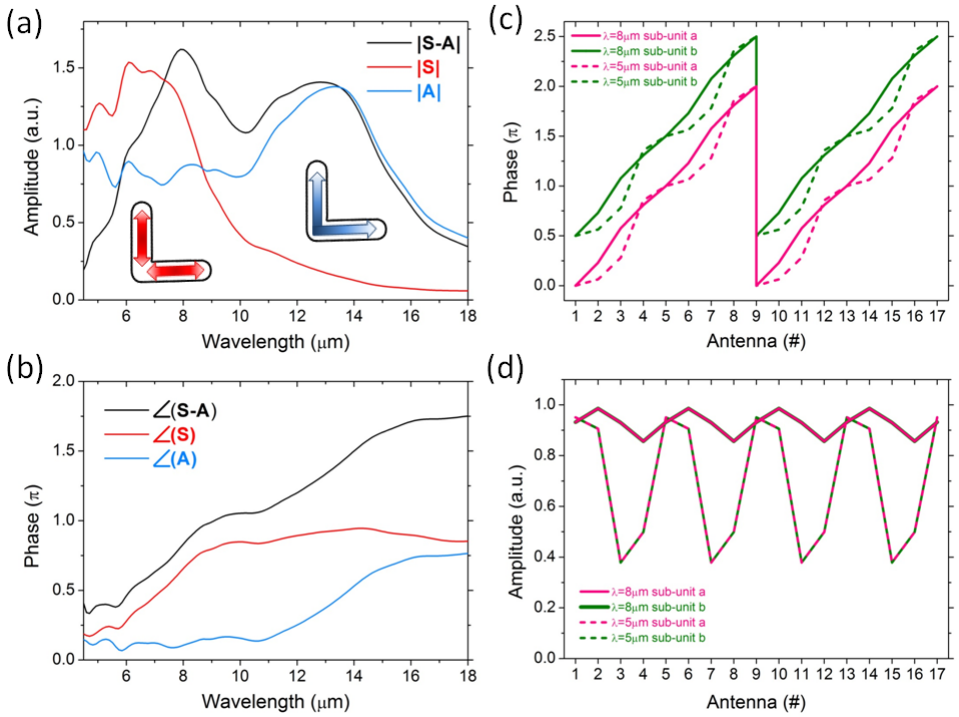

FIGURE 3.30: (a) and (b) Amplitude and phase responses of **S**, **A**, and **S** – **A** for a representative V-antenna obtained by full-wave simulations; here S and A represent the complex scattering amplitudes of the symmetric and antisymmetric eigenmodes, respectively. The arm length of the V-antenna is 1.2 μm and the angle between the two arms is 90°. This is the second antenna from the left in a given sub-unit (Fig. 3.31(a)). The current flow of the two eigenmodes of the antenna is shown in the insets. The arrows refer to the direction of current flow and the brightness represents the magnitude of the current density, with darker colors representing larger currents. The scattered light from the antenna can be decomposed into two components (**S** + **A**) and (**S** – **A**). By properly designing the phase and amplitude responses of these components in the antenna arrays, we can spatially separate them so that (**S** + **A**) and (**S** – **A**) lead to, respectively, the ordinary and extraordinary beams propagating in different directions. Because of the much broader effective plasmonic resonance as a result of the combined responses (i.e., **S** – **A** as compared to **S** or **A**), our metasurface quarter-wave plates can provide significant scattering efficiency over a broader wavelength range, as is shown in (a). The combined plasmonic resonances can also provide a larger coverage in the phase response (i.e., approximately 1.5π for **S** – **A** as compared to approximately 0.75π for **S** or **A**), as is shown in (b). (c) and (d) Calculated phase and amplitude responses along the antenna array. Responses for two consecutive sub-units are shown (i.e., antennas #9-16 are identical to antennas #1-8). Pink and green curves are for the first and second sub-unit, respectively; solid and dashed curves are for excitation wavelengths of 8 μm and 5 μm, respectively. As designed, the phase response at $\lambda = 8$ μm exhibits an almost constant gradient (i.e., 2π over 8 antennas in the sub-unit); the amplitude response at this wavelength is quite uniform. These properties correspond to an extraordinary beam with a flat wavefront and high intensity. However, at $\lambda = 5$ μm the phase does not follow a perfect linear profile and the amplitude response shows large variations. Even at this non-ideal situation, however, we still obtain an extraordinary beam with close-to-unity degree of circular polarization (but with reduced intensity) because the subwaves always have equal contributions to the beam since they have exactly the same wavefronts (compare the dashed curves in (c) or (d)).

The basic elements in our metasurface design are gold V-shaped antennas, each supporting symmetric and antisymmetric eigenmodes as previously discussed. For arbitrary incident polarization, both modes are excited and contribute to the antenna scattering response. The scattered waves from the eight antennas in a sub-unit can be written as:

$$\begin{pmatrix} \vec{E}_1 \\ \vec{E}_2 \\ \vec{E}_3 \\ \vec{E}_4 \\ \vec{E}_5 \\ \vec{E}_6 \\ \vec{E}_7 \\ \vec{E}_8 \end{pmatrix} = \frac{1}{2} \begin{bmatrix} \mathrm{S}_1 - \mathrm{A}_1 \\ \mathrm{S}_2 - \mathrm{A}_2 \\ \mathrm{S}_3 - \mathrm{A}_3 \\ \mathrm{S}_4 - \mathrm{A}_4 \\ -(\mathrm{S}_1 - \mathrm{A}_1) \\ -(\mathrm{S}_2 - \mathrm{A}_2) \\ -(\mathrm{S}_3 - \mathrm{A}_3) \\ -(\mathrm{S}_4 - \mathrm{A}_4) \end{bmatrix} [\cos(2\beta - \alpha)\ \hat{y} + \sin(2\beta - \alpha)\hat{x}] + \frac{1}{2} \begin{pmatrix} \mathrm{S}_1 + \mathrm{A}_1 \\ \mathrm{S}_2 + \mathrm{A}_2 \\ \mathrm{S}_3 + \mathrm{A}_3 \\ \mathrm{S}_4 + \mathrm{A}_4 \\ \mathrm{S}_1 + \mathrm{A}_1 \\ \mathrm{S}_2 + \mathrm{A}_2 \\ \mathrm{S}_3 + \mathrm{A}_3 \\ \mathrm{S}_4 + \mathrm{A}_4 \end{pmatrix} (\cos\alpha\hat{y} + \sin\alpha\hat{x}) \tag{3.23}$$

Here α and β are the orientation angles of the incident field and the antenna symmetry axis, respectively; $\hat{x}$ and $\hat{y}$ are the unit vectors along the x and y axes, respectively (Fig. 3.31(a) and (b)); $\mathrm{S_i}$and $\mathrm{A_i}$ are the complex scattering amplitudes of the symmetric and antisymmetric mode of the ith antenna in the sub-unit, respectively. Equation (3.23) shows that the scattered light from the antennas ($\vec{E}_\mathrm{i}$, with i =1-8) contains two terms, which are polarized along the $(2\beta - \alpha)$-direction and the α-direction from the y-axis, respectively. The antenna array is designed so that at $\lambda = 8\mu$m the $(2\beta - \alpha)$-polarized components of all the antennas have the same amplitude and an incremental phase of $\Delta\Phi = \pi/4$. That is, $\left|\mathrm{S_i} - \mathrm{A_i}\right|$ is constant, with i =1-4, and $\angle\left(\mathrm{S_{i+1}} - \mathrm{A_{i+1}}\right) - \angle\left(\mathrm{S_i} - \mathrm{A_i}\right) = \pi/4$, with i =1-3. Therefore the $(2\beta - \alpha)$-polarized partial waves scattered from the antenna array produce a wave propagating along the

$\theta_t = \arcsin(\lambda/\Gamma)$ direction from the surface normal. On the other hand, the α-polarized components, which have the same polarization as the incident light, have unequal amplitudes but similar phase responses. Therefore, the α-polarized partial waves combine to form a wave that propagates in a direction normal to the metasurface and contributes to the ordinary beam.

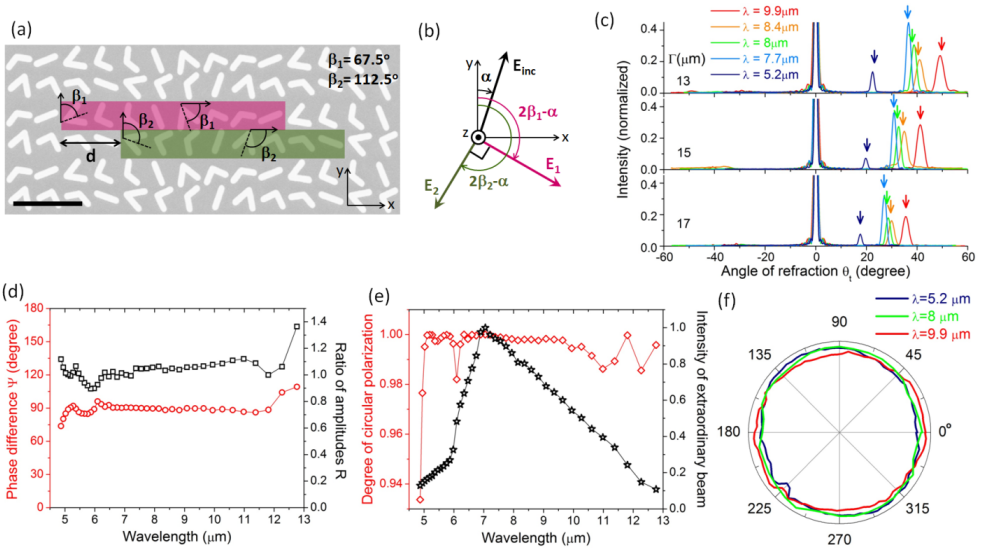

FIGURE 3.31: (a) SEM image of a metasurface quarter-wave plate. The unit cell of the metasurface comprises two sub-units (pink and green). Each sub-unit contains eight V-antennas, with the last four antennas obtained by rotating the first four clockwise by 90°. Antenna orientation angles are indicated by β_1 and β_2, and dashed lines represent the antenna symmetry axes. Scale bar is 4 μm. (b) Schematic showing the polarization of the two subwaves $\mathbf{E_1}$ and $\mathbf{E_2}$ scattered from the two sub-units, as well as that of the incident light. (c) Experimental far-field scans showing extraordinary beams at $\theta_t > 0$ generated by metasurfaces with different interfacial phase gradients (from $2\pi/13\mu$ m to $2\pi/17\mu$ m) at different wavelengths (from 5.2μ m to 9.9μ m), as well as the ordinary beams located at $\theta_t = 0$, given normally incident excitation. This broadband response is independent of the incident polarization. The scans are normalized with respect to the intensity of the ordinary beams. At a wavelength of 7.7 μm, the intensity of the extraordinary beams is 30-40% of that of the ordinary beams, corresponding to approximately 10% of the total incident power. The arrows indicate the calculated angular positions of the extraordinary beams according to $\theta_t = arcsin(\lambda/\Gamma)$. (d) Calculated phase difference Ψ and ratio of amplitudes R between the two subwaves as a function of wavelength. (e) Calculated degree of circular polarization and intensity of the extraordinary beam as a function of wavelength. (f) State-of-polarization analyses for the extraordinary beam at $\lambda = 5.2$, 8, and 9.9 μm. The measurements are performed by rotating a linear polarizer in front of a detector and measuring the transmitted power.

The metasurface quarter-wave plate has a unit cell consisting of two sub-units that are offset from each other in the horizontal direction by d (Fig. 3.31(a)). They create two

coherent subwaves that propagate along the θ_t =arcSin(λ/Γ) direction (Fig. 3.29(b)), The subwaves spatially overlap since the spacing between the two sub-units in the vertical direction is much smaller than the free-space wavelength (Fig. 3.31(a)), and have equal amplitude because the corresponding antennas in the two sub-units have the same geometries (i.e., arm length and opening angle). The orthogonal polarization between the subwaves is achieved by choosing antenna orientations $\beta_1 = 67.5^o$ and $\beta_2 = 112.5^o$ so that ($2\beta_2$ - α) - ($2\beta_1 - \alpha$) = 90^o (Fig. 3.31(b)). The 90^o phase difference between the subwaves is introduced by choosing the offset $d = \Gamma/4$, so that $\Psi = k_o d\text{Sin}(\theta_t) = 2\pi d/\Gamma = 90^o$. As a result of these properties, the two subwaves coherently interfere, producing a circularly polarized extraordinary beam (Fig. 3.29(b)). Note that once β_2 - $\beta_1 = 45^o$, the two subwaves will always have perpendicular polarization, which is independent of the orientation angle α of the linearly polarized incident light.

Our optical antenna arrays can provide phase coverage from 0^o to 360^o with an increment of approximately 45^o over a wide range of wavelengths (Fig. 3.16(b)). Therefore, the metasurface quarter-wave plates can generate well-defined extraordinary beams over a broad spectral range. Figure 3.31(c) shows experimental far-field scans at excitation wavelengths from 5.2 to 9.9 μm. Samples with Γ = 13, 15, and 17 μm have been tested. For all samples and excitation wavelengths, we observe the ordinary and extraordinary beams and negligible optical background. The observed angular positions of the extraordinary beams agree very well with the generalized law of refraction in the presence of the interfacial phase gradient, θ_t = arcSin(λ/Γ) (Fig. 3.31(c)). At 8 μm, close to the optimal operation wavelength, our metasurfaces scatter approximately 10% of the incident light into the extraordinary beam and the efficiency can in principle be increased by using denser antenna arrays or by exploiting antenna designs with higher scattering amplitude (e.g., antennas with a metallic back plane operating in reflection mode). Figure 3.31(d)

shows the phase difference Ψ and amplitude ratio R between the two subwaves scattered from the sub-units, calculated via FDTD simulations. It is observed that Ψ and R are in the close vicinity of 90^o and 1, respectively, over the λ =5 to 12 μm wavelength range; correspondingly, a high degree of circular polarization (DOCP) close to unity can be maintained over the wavelength range (Fig. 3.31(e)). Here DOCP is defined as $|I_{RCP}\text{-}I_{LCP}|/|I_{RCP}+I_{LCP}|$, where I_{RCP} and I_{RCP} stand for the intensities of the right and left circularly polarized components in the extraordinary beam, respectively. This result confirms our experimental findings that the circularly polarized beam has high purity (Fig. 3.31(f)). We have verified that the circular polarization of the extraordinary beam is independent of the orientation of the incident linear polarization. The extraordinary beam reaches its peak intensity at $\lambda \approx 7$ μm (Fig. 3.31(e)). The intensity decreases towards longer and shorter wavelengths because the **S** - **A** components of the scattered light from the antenna arrays start to have mismatched amplitudes and a nonlinear phase distribution.

We define the bandwidth of a quarter-wave plate $\Delta\lambda_{qw}$ as the wavelength range over which DOCP is sufficiently close to 1 (e.g., >0.95) and an output with high intensity can be maintained (e.g., intensity larger than half of the peak value). According to this definition, the bandwidth of our metasurface quarter-wave plates is about 4 μm (i.e., from $\lambda \approx 6$ to 10μm; see Fig. 3.31(e)), which is about 50% of the central operating wavelength $\lambda_{central}$. For comparison, the bandwidth of quarter-wave plates based on anisotropic rod or aperture antennas is typically $\Delta\lambda_{qw} \approx 0.05\text{-}0.1\lambda_{central}$ [128][194][196].

The polarizations of the subwaves are controlled by angles α, β_1, and β_2 and their amplitudes are controlled by the scattering amplitudes, **S** and **A**, of the antenna eigenmodes (Eq. (3.23)). This decoupling between polarization and amplitude allows us to synthesize beams with arbitrary polarization states. In addition to circularly polarized

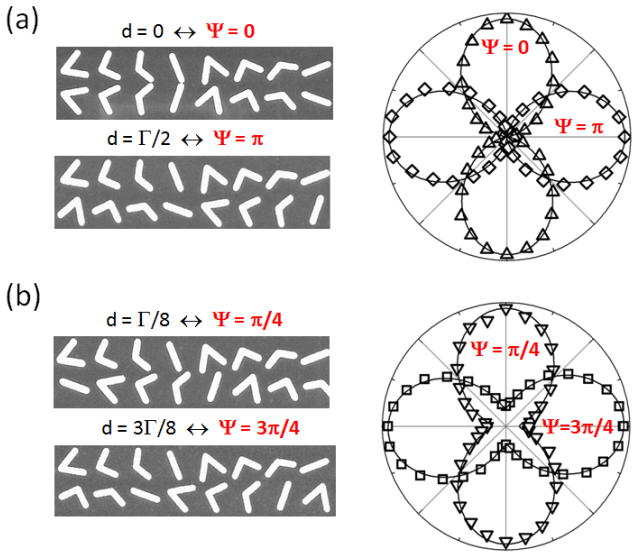

FIGURE 3.32: The offset between the sub-units, d, controls the phase difference between the two scattered subwaves and therefore the polarization of the extraordinary beam. The phase difference is $\Psi = k_o d\mathrm{Sin}(\theta_t) = 2\pi d/\Gamma$. Therefore, $d = 0$ or $\Gamma/2$ will lead to linear polarization, shown in (a);$d = \Gamma/4$ will lead to circular polarization, shown in Fig. 3.31; other choices will lead to elliptical polarization states; these shown in (b) are for $\Psi = \pi/4$ and $3\pi/4$. The left panels are SEM images of the unit cells and the right panels are the results of the state-of-polarization analyses. The symbols are measurements, and the curves are analytical calculations assuming that the two subwaves have equal amplitude and a phase difference equal to the value of Ψ indicated in the figures.

beams (Fig. 3.31), we were able to generate linearly polarized and elliptically polarized extraordinary beams by simply changing the sub-unit offset d (Fig. 3.32).

Wave plates are some of the most ubiquitous components in optics. Most commonly-used designs are based on bulk birefringent crystals with optical anisotropy. This conventional approach has several limitations: it is relatively narrow band and it relies on the availability of birefringent materials in the desired frequency range. Approaches exist to overcome the latter limitation, which utilize form birefringence of anisotropic structures such as plasmonic antennas. These come with their own limitations; in particular, they exhibit relatively low purity of polarization and often superimpose an optical background onto the desired signal. In addition, the bandwidth of these devices is also relatively small. Our approach, which involves spatially inhomogeneous arrays of anisotropic optical antennas, overcomes many of these limitations. We experimentally demonstrated

quarter- and half-wave plates, which are broadband and have high polarization purity (e.g., output of quarter-wave plate with DOCP larger than 0.97 over $\lambda = 5$ to 12 μm, and with intensity larger than half-maximum over $\lambda = 6$ to 10 μm). This approach requires only a single step of conventional lithography and is generalizable from the visible to the radio-frequency regimes.

3.9 Flat lenses and axicons

The fabrication of refractive lenses with aberration correction is difficult and low-weight small-volume lenses based on diffraction are highly desirable. At optical frequencies, planar focusing devices have been demonstrated using arrays of nanoholes [202], optical masks [203][204][120], nanoslits [205], and loop antennas [206]. In addition flat metamaterial-based lenses such as hyperlenses and superlenses have been used to demonstrate optical imaging with resolution finer than the diffraction limit [162][207][208][209]. We designed and demonstrated planar lenses and axicons based on metasurfaces at telecom wavelength of $\lambda = 1.55$ μm. Planar lenses can mold incident planar wavefronts into spherical ones and therefore achieve focusing without monochromatic aberrations; axicons are conical shaped lenses that can convert Gaussian beams into non-diffracting Bessel beams and can create hollow beams [107][210].

The design of flat lenses is obtained by imposing a hyperboloidal phase profile on the metasurface. In this way, secondary waves emerging from the latter constructively interfere at the focal point similar to the waves that emerge from conventional lenses [1]. For a given focal length f, the phase shift ϕ_{L} imposed on every point $\mathrm{P_L(x,y)}$ on the

flat lens (Fig. 3.33(a)) must satisfy

$$\varphi_L(x,y) = \frac{2\pi}{\lambda}\overline{P_L S_L} = \frac{2\pi}{\lambda}\left(\sqrt{x^2+y^2+f^2} - f\right) \tag{3.24}$$

For an axicon with angle ξ, the phase delay has to increase linearly with the distance from the center. The phase shift ϕ_{A} at every point $\mathrm{P_A(x,y)}$ has to satisfy

$$\varphi_A(x,y) = \frac{2\pi}{\lambda}\overline{P_A S_A} = \frac{2\pi}{\lambda}\sqrt{x^2+y^2}\sin\xi \tag{3.25}$$

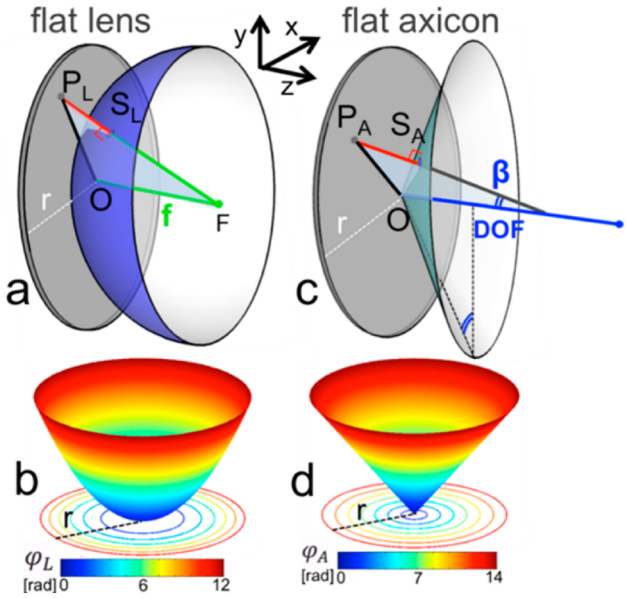

FIGURE 3.33: Schematics showing the design of flat lenses and axicons. To focus a plane wave to a single point at distance f from the metasurface, a hyperboloidal phase profile must be imparted onto the incident wavefront. (a) The phase shift at a point $\mathrm{P_L}$ on the flat lens is designed to be proportional to the distance between $\mathrm{P_L}$ and its corresponding point $\mathrm{S_L}$ on the spherical surface of radius f and is given by Eq. (3.24). (b) The axicon images a point source onto a line segment along the optical axis; the length of the segment is the depth of focus (DOF). The phase (Eq. (3.25)) in point $\mathrm{P_A}$ on the flat axicon is proportional to the distance between $\mathrm{P_A}$ and its corresponding point $\mathrm{S_A}$ on the surface of a cone with base angle ξ =arctan(r/DOF), where r is the radius of the flat axicon.

The design of these lenses and axicons can be made to be free from monochromatic aberrations typically present in conventional refractive optics. A spherical lens focuses light to a single point only in the limit of paraxial approximation; a deviation from this

condition introduces monochromatic aberrations such as spherical aberrations, coma, and astigmatism [1]. To circumvent this problem, aspheric lenses or multi-lens designs are implemented [1]. In our case, the hyperboloidal phase distribution imposed at the metasurfaces produces a wavefront that remains spherical under non-paraxial conditions, which can enable high numerical-aperture (NA) focusing without aberrations.

To demonstrate this new flat lens we designed eight different plasmonic V-antennas that scatter light in cross-polarization with relatively constant amplitudes and incremental phases of $\pi/4$ in the near-infrared (Fig. 13.34(a)). These antennas are used to form arrays according to the phase distributions specified in Eqs. (3.24) and (3.25) to create two flat lenses (r=0.45 mm, f =3 cm, corresponding to NA=0.015; r=0.45 mm, f =6 cm, corresponding to NA=0.075), and an axicon (r=0.45 mm, ξ =0.5^{o}). These flat optical components are fabricated by patterning double-side-polished undoped silicon wafers with gold nano-antennas using electron beam lithography. A schematic experimental setup is shown in Fig. 3.34(b).

The measured far-field for the metasurface lens with 3 cm focal distance and the corresponding analytical calculations are presented in Figs. 3.35(a)-(c). The results for the metasurface axicon and for an ideal axicon are presented in Figs. 3.35(d)-(f). We found good agreement between experiments and calculations. In the calculations, the metasurfaces are modeled as an ensemble of dipolar emitters with identical scattering amplitudes and phase distributions given by Eqs. 3.24 and 3.25. Note that the actual non-diffracting distance of the metasurface axicon is slightly shorter than the ideal DOF because the device is illuminated with a collimated Gaussian beam instead of a plane wave [211]. The efficiency in focusing light of the flat lens in Fig. 3.34(c) is about 1% because of the relatively large antenna spacing of 750 nm, which is limited by the

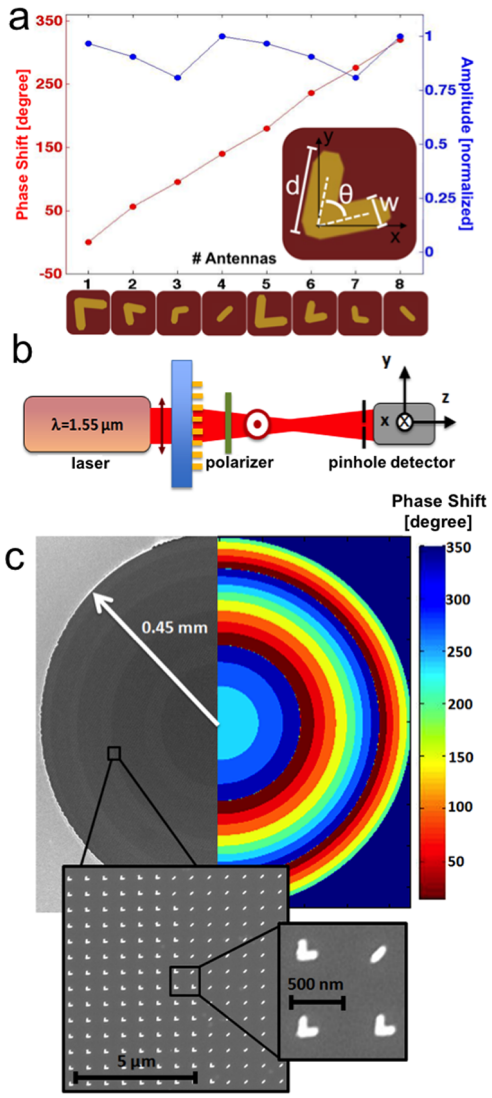

FIGURE 3.34: (a) FDTD simulations of the phase shifts and scattering amplitudes in cross-polarization for the eight V-antennas designed to operate at λ =1.55μm. The parameters characterizing the elements from 1 to 4 are: h = 180 nm, 140 nm, 130 nm, 85 nm and Δ = 79°, 68°, 104°, 175°. Elements #5 - #8 are obtained by rotating #1-#4 by an angle of 90°counter-clockwise. The antenna width is fixed at 50 nm. (b) Experimental setup: a diode laser beam at λ =1.55 μm is incident onto the sample with y-polarization. The light scattered by the metasurface in x-polarization is isolated with a polarizer. A detector mounted on a 3-axis motorized translational stage detects the light passing through a pinhole, attached to the detector, with an aperture of 50 μm. The lenses and axicon also work for x-polarized illumination because of symmetry in our design: the antennas have their symmetry axis along the 45°-direction; therefore x-polarized illumination will lead to y-polarized focused light. In general, our flat optical components can focus light with any arbitrary polarization because the latter can always be decomposed into two independent components polarized in the x- and y-directions. (c) Left panel: SEM image of the fabricated lens with 3 cm focal length. Right panel: Phase profile calculated from Eq. 14 and discretized according to the phase responses of the eight antennas. Insets: zoom-ins of fabricated antennas. The antenna array has a square lattice with a lattice constant of 750 nm.

fabrication time of EBL; it can be improved to about 10% by using a higher antenna packing density with an antenna spacing of 220 nm according to our calculations.

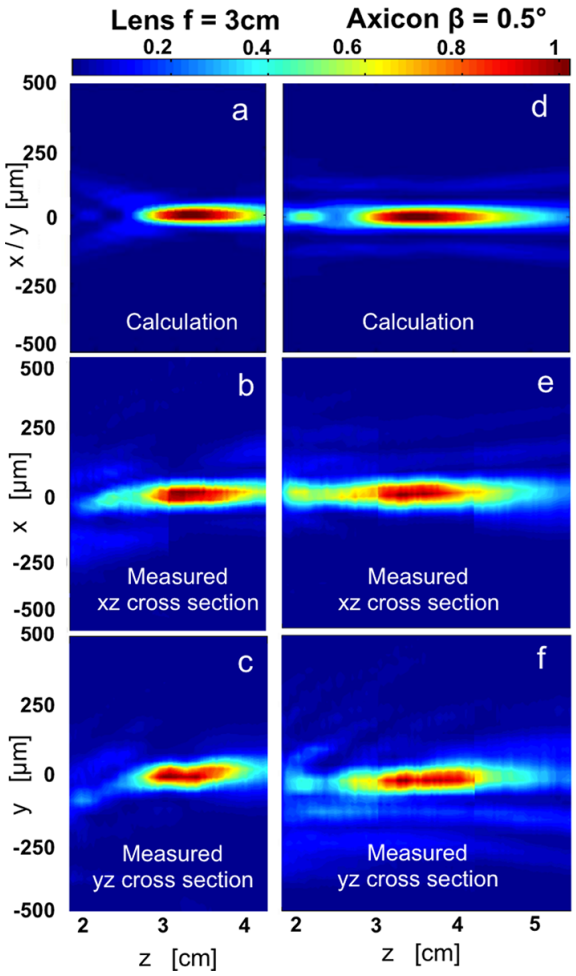

FIGURE 3.35: (a)-(c) Calculations and experimental results of the intensity distribution in the focal region for the flat lens with f =3 cm. (a) is calculated using the dipolar model. (b) and (c) are the experimental results showing the xz- and yz-cross sections of the 3D intensity distribution, respectively. (d)-(f) Calculations and experimental results of the intensity distribution for the planar axicon with ξ =0.5°.

The ability to design phase shifts on a flat surface over a 0-to-2π range with a subwavelength spatial resolution is significant. For example, it is possible to produce large phase gradients, which are necessary to create high NA planar lenses. FDTD simulations of a high-NA cylindrical lens are shown in Fig. 3.36. Although the present design is diffraction limited, focusing below the diffraction limit in the far field is possible using plates patterned with structures that provide subwavelength spatial resolution of phase and

amplitude [204]. Planar lenses and axicons can be designed for other range of frequencies and may become particularly interesting in the mid-infrared and terahertz regimes where the choice of suitable refractive materials is limited compared to the near-infrared and the visible.

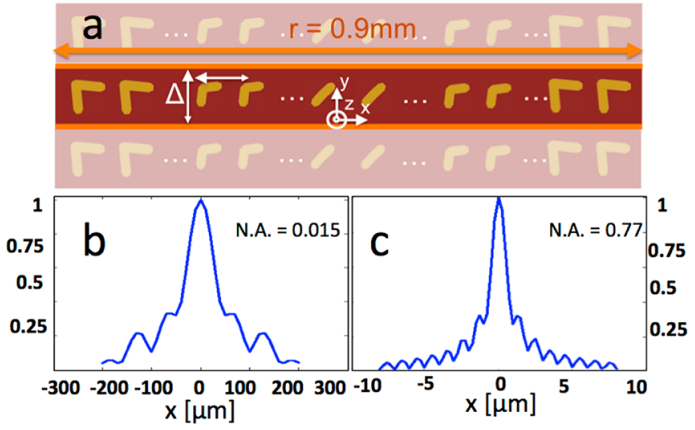

FIGURE 3.36: (a) Schematic unit cell of a high numerical aperture (NA=0.77) cylindrical lens. The dimensions of the unit cell are 0.9 mm by 300 nm and its phase distribution in the lateral direction is determined by Eqn. 3.24. In the y-direction, periodic boundary conditions are used in simulations. (b) Line scan of intensity at the focal plane for the lens with $f = 371$ μm. The beam waist is 1 μm.

3.10 Dynamically tunable optical antennas

As we showed in the previous sections, the near- and far-field response of optical antennas can be tailored by engineering the geometrical parameters. However, dynamic control of these optical properties is particularly appealing. The integration of metasurfaces comprising optical phase discontinuities with active materials such as graphene, vanadium oxide, and tungsten oxide will enable large-scale dynamically tunable phased antenna arrays at visible, infrared and terahertz which will augment or replace existing spatial light modulators and displays which use liquid crystal technology.

In this section, we briefly discuss two tuning mechanisms based on VO_2 and graphene. Compared to liquid crystals, our active materials will enable designs that are much faster,

more lightweight, and potentially easier to implement. Graphene and VO_2 both show potential switching performance on picosecond time scales, orders of magnitude faster that than the fastest liquid crystal devices; this switching speed is of critical importance to applications such as beam steering, all-optical switching and processing, and adaptive optical devices.

3.10.1 Insulator-metal transition in vanadium oxide as a tuning mechanism

In this section we demonstrate that resonances of mid-IR plasmonic antennas can be tuned and switched on/off by thermal control of phase co-existence in a vanadium dioxide (VO_2) substrate. A similar approach has been previously explored for the tuning of the effective refractive index of metamaterials in the terahertz (THz) [51][212][213] and near-IR [58], tuning nanoparticle scattering spectra in the visible [214][215][216], and control of transmission through apertures in the THz [59]. We utilized a normalization procedure that helps isolate the antenna resonances from the optical response of the unpatterned underlying substrate in proximity to the VO_2 phase transition. To validate our results, we incorporated the literature complex refractive indices of VO_2 throughout its phase transition into full-wave numerical simulations and observed qualitative agreement between the simulated and experimental reflectivity spectra.

In general, a plasmonic antenna can be made tunable by incorporating a material such as VO_2 into its design; here, we focus on Y-shaped antennas such as the ones shown in section 3.6. We fabricated a square array of gold (Au) Y-shaped antennas with a period of 3 μm on a thick, single-side-polished c-plane sapphire substrate coated with approximately 180 nm of single-crystalline VO_2. The antenna spacing is large to minimize

near-field coupling between neighboring antennas. The VO_2 film was deposited using magnetron sputtering from a V_2O_5 target at 550° C under 10 mTorr pressure with 100 sccm Ar gas flow at a power of 120 W to obtain phase pure VO_2. The antennas were defined using electron-beam lithography and deposition of 5 nm of Ti and 40 nm of Au, and lift-off. A scanning electron microscope (SEM) image of the structures is shown in Fig. 3.37(a); the vertical and horizontal arms are approximately 1.05 μm long and the diagonal arm is approximately 0.75 μm long, all with a width of approximately 160 nm. The roughness of the VO_2 film is visible in the SEM image, and was transferred to the metallic antennas.

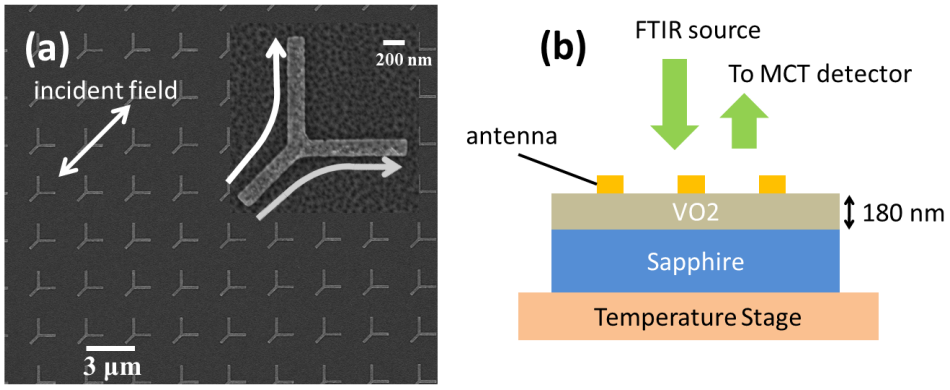

FIGURE 3.37: (a) Scanning electron microscope image of the fabricated sample comprising an array of gold antennas on a approximately 180 nm VO_2 film deposited on a sapphire wafer. Inset: zoomed-in image of a single Y-shaped antenna with arrows indicating the flow of the current. (b) Schematic of the reflectivity measurement. Light from an FTIR is incident on the temperature-controlled sample, and the reflection is sent to a detector.

An antenna array situated on a dielectric substrate can be viewed as a frequency selective surface, and is expected to have a peak in its reflectivity spectrum when on resonance [217]. We collected temperature-dependent reflectivity spectra by using a Fourier transform infrared (FTIR) spectrometer (Bruker Vertex 70), connected to a mid-IR microscope (Bruker Hyperion 2000) equipped with a temperature-controlled stage (Bruker A599). A schematic of the setup is shown in Fig. 3.37(b). A Cassegrain objective (15X, NA = 0.4) was used to focus a polarized beam from a Globar source onto the

sample, with the reflected light collected by the same objective and sent to a cooled mercury-cadmium-telluride (MCT) detector. Nearly all of the light that is not reflected is absorbed within the antennas, the VO_2 film, and the underlying sapphire as it is not transparent for $\lambda > 5$ μ m. At each temperature, the reflectivity spectra were normalized to (i. e. divided by) the reflectivity of the bare VO_2/sapphire substrate at that same temperature. Such normalization helps isolate the reflectivity feature due to the antennas at each temperature from the nontrivial reflectivity of the underlying VO_2 film on sapphire.

The normalized reflectivity is shown in Fig. 3.38(a), with the incident polarization along the symmetry axis of the antennas as indicated with the double-sided arrow in Fig. 3.37(a); this ensures that no polarization conversion takes place at the antenna array. When the VO_2 is in the dielectric state (e.g. T = 28 °C), the resonances of the antennas in the array lead to a peak in reflectivity at around $\lambda = 9.3$ μ m. As the temperature increases to T = 69 °C, this peak is red-shifted to $\lambda = 10.5$ μ m, corresponding to a greater than 10% shift in the resonance frequency. This shift coincides with a decrease in the peak reflectivity and increase in the linewidth. The wavelength of the reflectivity peak and its value are plotted in Fig. 3.38(b) as a function of temperature when heating (solid lines), and then cooling back down (dotted lines). There is hysteresis in this plot which is inherent to the VO_2 phase transition, though the full hysteresis loop is not visible in Fig. 3.38(b) because we truncated the temperatures at 69 °C for heating, and 63 °C for cooling, respectively; beyond these temperatures the reflectivity peak disappears.

The key features of Fig. 3.38(a) are reproduced by FDTD simulations in 3.39(a). Periodic boundary conditions were used to capture the effect of the array. The IR complex refractive index data for sapphire, Ti, and Au was interpolated from literature data [64],

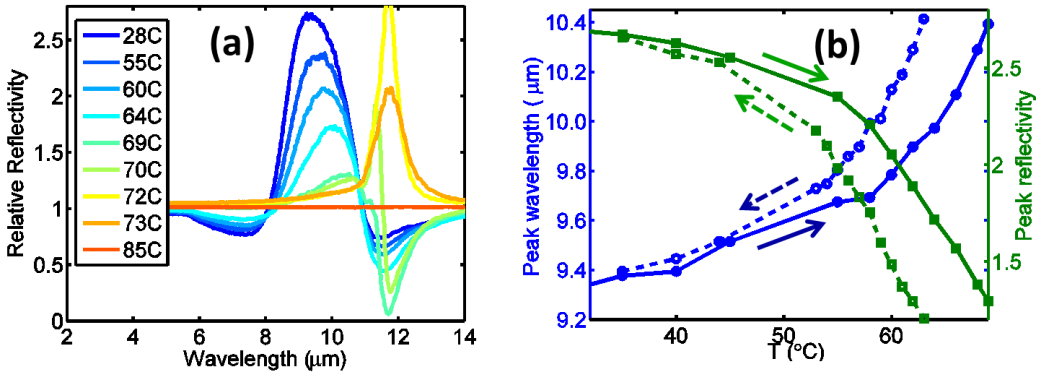

FIGURE 3.38: (a) Reflectivity spectra of the antenna array for increasing temperatures, showing the evolution of the antenna resonance through the VO_2 phase transition. At each temperature, the spectrum was normalized to reflectivity of the substrate without the antennas. (b) The wavelength at which the reflectivity peaks (blue) and the normalized peak reflectivity value (green) as a function of temperature during heating (solid lines) and cooling (dashed lines).

while the VO_2 refractive indices throughout its phase transition were taken from ellipsometry measurements in ref. [52]. The differences between the experimental results of Fig. 3.38(a) and the calculations of Fig. 3.39(a) are primarily due to the differing growth conditions and thicknesses between our VO_2 sample and the one measured in ref. [52], which lead to a different temperature-dependent complex refractive index, as well as the surface roughness which is not accounted for in the simulations.

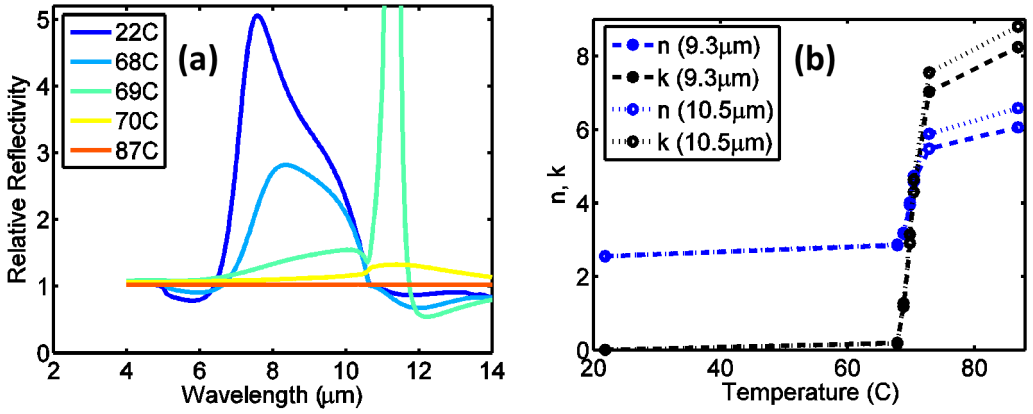

FIGURE 3.39: (a) Calculated normalized reflectivity spectra corresponding to the experimental data in Fig. 3.38(a) using FDTD, incorporating literature values for the complex refractive indices of gold, VO_2, and sapphire. (b) Real (n) and imaginary (k) parts of the refractive index of VO_2 at wavelengths of 9.3 μm and 10.5 μm.

This shift in the resonance occurs because the refractive index of the underlying VO_2

changes as a function of temperature. At the onset of the transition, the real part of the complex refractive index n increases at mid-IR wavelengths (curves for 9.3 μm and 10.5 μm are shown in blue in Fig. 3.39(b)). This increase in the substrate index is strongly felt by the antenna, which acts as a dispersive Fabry-Perot resonator for surface plasmons with the effective index of the mode dependent on the index of the substrate [153][218]. In the present demonstration, we are exciting one of the two plasmonic eigenmodes of the Y-shaped antenna; the other eigenmode feels the index change of the substrate in the same way. Through the course of the VO_2 phase transition the antenna resonance is also impacted by the increase of losses (the values of the imaginary part k of the complex refractive index of VO_2 are shown in black in Fig. 3.39(b)), which increase as the fraction of the metallic-phase VO_2 increases, resulting in a lower-amplitude reflectivity maximum. As the VO_2 film transitions into its high-temperature metallic state (where $k > n$), the antennas become "shorted" and can no longer be viewed as isolated resonant elements, so the reflectivity maximum disappears (orange curves in Fig. 3.38(a) and Fig. 3.39(a)). The peak in normalized reflectivity in Fig. 3.38(a) and Fig. 3.39(a) at 11-12 μm that appears at temperatures close to the critical IMT temperature is a result of a "division by zero": at this wavelength and temperature the reflectivity of the underlying VO_2/sapphire substrate is approximately 0 as a result of critical coupling to an ultra-thin cavity resonance as described in section 2.4, causing a divergence in the normalized curves. The dip at this same wavelength but at a slightly lower temperature (Fig. 3.38(a)) is an indication that the critical coupling condition is reached for a lower temperature in the presence of antennas due to enhanced absorption in the VO_2.

While we presently demonstrated thermal tuning of an entire antenna array, DC and AC fields can be applied to individual antennas or even individual sections of antennas on isolated patches of VO_2, creating a tunable inhomogeneous distribution of amplitude and

phase responses within an array of antennas. Such a demonstration would be of interest to realizing antenna-based spatial light modulators capable of addressing amplitude and phase of infrared and terahertz light, active and passive thermal labels and emitters, displays, and related dynamically-reconfigurable devices.

3.10.2 Electrostatic doping in graphene as a tuning mechanism

While VO_2 is a potential candidate for tuning the response of optical antennas, the additional optical losses induced by the transition tend to lead to a broadening and eventual disappearance of the antenna resonance (Figs. 3.38 and 3.39), and therefore it is uncertain if it can be used to obtain wide dynamic control of phased antenna metasurfaces.

In this section we briefly discuss an alternative tuning mechanism based on electrostatic doping of graphene. A more full discussion of this tuning technique and its application to optical antennas can be found in ref. [219]. Graphene is a well-studied material, comprising a monolayer of hexagonally-arranged carbon atoms [220], exhibits gate-voltage dependent optical conductivity and can be used as an electrically tunable plasmonic material [221] [222]. In particular, we show that graphene can be integrated into the nano-gaps of coupled optical antennas to achieve broad tuning of an antenna resonance. The origin of gate-voltage dependent optical properties in graphene lies in the fact that its carrier density and Fermi level can be controlled by the gate voltage, or in other words, electrostatic doping.

The graphene sheet optical conductivity used in our calculations and simulations is derived within the random-phase approximation (RPA) in the local limit [223].

$$\sigma_s(\omega) = \frac{i2e^2 k_B T}{\pi\hbar^2(\omega + i\tau^{-1})} \ln[2\cosh(\frac{E_F}{2k_B T})] \tag{3.26}$$
$$+\frac{e^2}{4\hbar}\left[\frac{1}{2} + \frac{1}{\pi}\arctan\left(\frac{\hbar\omega - 2E_F}{2k_B T}\right) - \frac{i}{2\pi}\ln\frac{(\hbar\omega + 2E_F)^2}{(\hbar\omega - 2E_F)^2 + 4(k_B T)^2}\right]$$

Where k_B is the Boltzman constant, T is the temperature, ω is the frequency, τ is the carrier relaxation lifetime, and E_F is the Fermi level, which is dependent on the graphene doping. The first term of Eqn. 3.26 is attributed to intraband transitions and the second term to interband transitions. When the Fermi level is below half of the photon energy ($E_{ph} = \hbar\omega$), the contribution from the interband transition dominates the optical conductivity. Once the Fermi level is increased above half of the photon energy, interband transitions are diminished due to Pauli blocking and intraband transitions play an important role. In this region, the real part of graphene permittivity ϵ_r becomes dominant over the imaginary part ϵ_i. As the doping density increases, the real part of the permittivity decreases; we utilized this doping-dependent permittivity to tune the resonances of optical antennas.

Just as with the VO_2 in the last section, when a tunable material such as graphene is introduced in the vicinity of an optical antenna, the antenna resonance is shifted. As the graphene doping density increases, the real part of the permittivity of the graphene becomes smaller ($\Delta\epsilon < 0$); therefore, the antenna resonance will be blue-shifted ($\Delta\omega > 0$). Without going into the experimental data or semi-analytical models which can be found in ref. [219], we present the simulation data for optical antennas sitting on a sheet of graphene, on a silicon substrate with a thin layer of thermal native oxide. Instead of simple linear antennas or V-shaped antennas such as the ones used in earlier sections, we used antennas with small gaps (either pairs, quadruplets, or 1D arrays (Fig. 3.40(c))).

We use the enhanced fields in the antenna gaps [224] to increase the interaction between the tunable graphene region and light (Fig. 3.40(a)). In fact, by using a structure with a 20 nm gap, a 300% increase in the wavelength tuning range can be achieved compared to the tuning of isolated rod antennas (Fig. 3.40(b)).

The antenna tuning that can be expected to be achieved with these gaps corresponds to a resonant shift between approximately 7 μm and 8 μm in the antenna resonant wavelength. While this shift is not much larger than what we achieved with VO_2 in the previous section, it does not lead to the same degradation of the antenna quality factor. This, in our opinion, this technique is more promising than tuning techniques based on VO_2, at least in the mid-infrared spectral range.

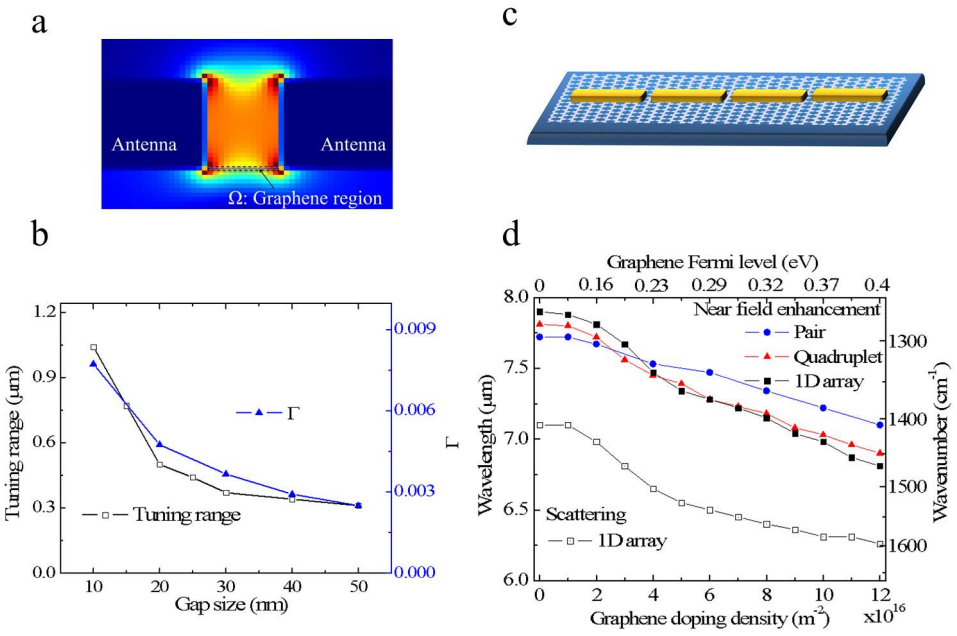

FIGURE 3.40: a) Field distribution in the gap between antennas. b) Calculated tuning ranges and confinement factors as functions of the gap size g. c) Schematic of end-to-end coupled antenna array. d) Near field enhancement (in the center of the gap) peak wavelength of an antenna pair, antenna quadruplet, and 1D antenna array (gap size 20 nm) as well as scattering resonance peak wavelength of 1D antenna array obtained by FDTD simulations (the substrate is 30 nm silicon oxide on silicon). All simulations and calculations are performed for 240 nm wide, 1.8 m long, 40 nm thick gold antennas.

3.11 Conclusion

In summary, this chapter discusses the phase response of plasmonic antennas and a new class of planar optical components, "metasurfaces", which are based on phased optical antenna arrays. The control of phase response is achieved by choosing antenna geometry so it operates at different positions on the antenna resonance curve, corresponding to different phase shifts between the scattered and incident light. The metasurface design features subwavelength control of phase, amplitude, and polarization of optical wavefront without relying on the propagation effect. This is very different from conventional optical components such as lenses, diffractive optics, and wave plates. The subwavelength resolution of metasurface will enable not only far-field engineering but also near-field and meso-field engineering of optical wavefronts. Eventually, dynamically tunable optical antennas will serve as components for active metasurfaces which will enable applications such as beam steering and ultra-fast displays and spatial light modulators between the visible and the far-infrared.

Chapter 4

Conclusion

The focus of this thesis has been on the manipulation of light using functional surfaces that are significantly thinner than a single wavelength of light. In *Chapter 2* we described a new special case of thin film interference which utilizes highly-lossy materials. This concept arises when optical loss is treated as an important design component rather than as a perturbation or as something undesirable, and this can only be done when structures are very thin such that not all light is absorbed through a single pass. These may find their way into many intriguing applications from printing, labeling, and visual design to optoelectronic devices with enhanced efficiencies. The possibility of creating ultra-thin photovoltaics, photoconductors, and other types of light harvesters and detectors is particularly appealing as it may reduce the cost of devices while increasing speed and efficiency. In *Chapter 3* we described quasi-two dimensional structures consisting of arrays of subwavelength resonators for direct control of the amplitude, phase, and polarization of light as it traverses an interface. While our experimental demonstrations have shown several interesting optical phenomena such as anomalous reflection and refraction and applications such as arbitrary wavefront generation, additional development is

necessary before these structures find their way into devices. In particular higher conversion efficiencies must be achieved before these ultra-flat lenses, wave-plates, etc. will be able to compete against conventional refractive and diffractive optical components. Given the state of the literature it seems that this is now within reach, at least for longer wavelengths. Combining these wavefront-manipulating structures with tunable optical materials may ultimately lead to new reconfigurable optical devices.

Bibliography

[1] E Hecht. Optics, 4th ed. 2002.

[2] H. Angus Macleod. *Thin-Film Optical Filters, Fourth Edition*. CRC Press, 2010. ISBN 1420073028.

[3] Guinnog. Diesel rainbow, 2007. URL `http://en.wikipedia.org/wiki/File:Dieselrainbow.jpg`.

[4] Iman Sadeghi. Having fun with Soap Bubbles, 2007. URL `http://graphics.ucsd.edu/~iman/SoapBubbles/`.

[5] Greg Gbur. The Secret Molecular Life of Soap Films. *Optics and Photonics News*, July/Augus, 2013.

[6] Emily Gaul. Coloring titanium and related metals by electrochemical oxidation. *Journal of Chemical Education*, 70(3):176, March 1993.

[7] Mikhail A. Kats, Deepika Sharma, Jiao Lin, Patrice Genevet, Romain Blanchard, Zheng Yang, M. Mumtaz Qazilbash, D. N. Basov, Shriram Ramanathan, and Federico Capasso. Ultra-thin perfect absorber employing a tunable phase change material. *Applied Physics Letters*, 101(22):221101, November 2012.

[8] Mikhail A Kats, Romain Blanchard, Patrice Genevet, and Federico Capasso. Nanometre optical coatings based on strong interference effects in highly absorbing media. *Nature materials*, 12(1):20–4, 2013.

[9] Mikhail A. Kats, Steven J. Byrnes, Romain Blanchard, Mathias Kolle, Patrice Genevet, Joanna Aizenberg, and Federico Capasso. Enhancement of absorption and color contrast in ultra-thin highly absorbing optical coatings. *Applied Physics Letters*, 103(10):101104, September 2013.

[10] Mikhail A. Kats, Romain Blanchard, Shuyan Zhang, Patrice Genevet, Changhyun Ko, Shriram Ramanathan, and Federico Capasso. Vanadium dioxide as a natural disordered metamaterial: perfect thermal emission and large broadband negative differential thermal emittance. April 2013.

[11] F Gires and P Tournois. Interferometre utilisable pour la compression d'impulsions lumineuses modulees en frequence. *CR Acad. Sci. Paris*, 1964.

[12] R.H. Yan, R.J. Simes, and L.A. Coldren. Electroabsorptive Fabry-Perot reflection modulators with asymmetric mirrors. *IEEE Photonics Technology Letters*, 1(9): 273–275, September 1989.

[13] K. Kishino, M.S. Unlu, J.-I. Chyi, J. Reed, L. Arsenault, and H. Morkoc. Resonant cavity-enhanced (RCE) photodetectors. *IEEE Journal of Quantum Electronics*, 27 (8):2025–2034, 1991.

[14] M. Selim Unlu and Samuel Strite. Resonant cavity enhanced photonic devices. *Journal of Applied Physics*, 78(2):607, July 1995.

[15] V T Bly and J T Cox. Infrared absorber for ferroelectric detectors. *Applied optics*, 33(1):26–30, January 1994.

[16] M Born and E Wolf. *Principles of optics: electromagnetic theory of propagation, interference and diffraction of light*. 1999.

[17] P. F. Robusto and R. Braunstein. Optical Measurements of the Surface Plasmon of Indium-Tin Oxide. *physica status solidi (a)*, 119(1):155–168, May 1990.

[18] F Gervais and B Piriou. Anharmonicity in several-polar-mode crystals: adjusting phonon self-energy of LO and TO modes in Al 2 O 3 and TiO 2 to fit infrared reflectivity. *Journal of Physics C: Solid State Physics*, 7(13):2374–2386, July 1974.

[19] Manuel Cardona and Gunther Harbeke. Absorption Spectrum of Germanium and Zinc-Blende-Type Materials at Energies Higher than the Fundamental Absorption Edge. *Journal of Applied Physics*, 34(4):813, April 1963.

[20] James N. Hilfiker, Neha Singh, Tom Tiwald, Diana Convey, Steven M. Smith, Jeffrey H. Baker, and Harland G. Tompkins. Survey of methods to characterize thin absorbing films with Spectroscopic Ellipsometry. *Thin Solid Films*, 516(22): 7979–7989, 2008.

[21] Jianfa Zhang, Jun-Yu Ou, Nikitas Papasimakis, Yifang Chen, Kevin F Macdonald, and Nikolay I Zheludev. Continuous metal plasmonic frequency selective surfaces. *Optics express*, 19(23):23279–85, November 2011.

[22] A. Vorobyev and Chunlei Guo. Enhanced absorptance of gold following multipulse femtosecond laser ablation. *Physical Review B*, 72(19):195422, November 2005.

[23] A. Y. Vorobyev and Chunlei Guo. Colorizing metals with femtosecond laser pulses. *Applied Physics Letters*, 92(4):041914, January 2008.

[24] Xulongqi Wang, Dongxian Zhang, Haijun Zhang, Yi Ma, and J Z Jiang. Tuning color by pore depth of metal-coated porous alumina. *Nanotechnology*, 22(30): 305306, July 2011.

[25] S. Chattopadhyay, Y.F. Huang, Y.J. Jen, A. Ganguly, K.H. Chen, and L.C. Chen. Anti-reflecting and photonic nanostructures. *Materials Science and Engineering: R: Reports*, 69(1):1–35, 2010.

[26] Hermann A. Haus. *Waves and Fields in Optoelectronics (Prentice-Hall series in solid state physical electronics)*. Prentice Hall, 1983. ISBN 0139460535.

[27] R.-H. Yan, R.J. Simes, and L.A. Coldren. Surface-normal electroabsorption reflection modulators using asymmetric Fabry-Perot structures. *IEEE Journal of Quantum Electronics*, 27(7):1922–1931, July 1991.

[28] Paul W Loscutoff and Stacey F Bent. Reactivity of the germanium surface: Chemical passivation and functionalization. *Annual review of physical chemistry*, 57: 467–95, January 2006.

[29] W. L. Hansen, E. E. Haller, and G. S. Hubbard. Protective Surface Coatings on Semiconductor Nuclear Radiation Detectors. *IEEE Transactions on Nuclear Science*, 27(1):247–251, 1980.

[30] Tydex. Hard Carbon Coating (DLC: "Diamond-Like Coating"), 2013. URL `http://www.tydexoptics.com/materials1/coatings/dlccoatings/`.

[31] M. Alaluf, J. Appelbaum, L. Klibanov, D. Brinker, D. Scheiman, and N. Croitoru. Amorphous diamond-like carbon filmsa hard anti-reflecting coating for silicon solar cells. *Thin Solid Films*, 256(1):1–3, 1995.

[32] R. M. A. Azzam. Maximum minimum reflectance of parallel-polarized light at interfaces between transparent and absorbing media. *Journal of the Optical Society of America*, 73(7):959, July 1983.

[33] Woollam. Ellipsometry FAQ, 2013.

[34] Vivian E Ferry, Jeremy N Munday, and Harry A Atwater. Design considerations for plasmonic photovoltaics. *Advanced materials (Deerfield Beach, Fla.)*, 22(43): 4794–808, November 2010.

[35] Nathan S Lewis. Toward cost-effective solar energy use. *Science (New York, N.Y.)*, 315(5813):798–801, February 2007.

[36] Hen Dotan, Ofer Kfir, Elad Sharlin, Oshri Blank, Moran Gross, Irina Dumchin, Guy Ankonina, and Avner Rothschild. Resonant light trapping in ultrathin films for water splitting. *Nature materials*, 12(2):158–64, February 2013.

[37] J A Dobrowolski. Versatile computer program for absorbing optical thin film systems. *Applied optics*, 20(1):74–81, January 1981.

[38] Pochi Yeh. *Optical Waves in Layered Media (Wiley Series in Pure and Applied Optics)*. Wiley-Interscience, 2005. ISBN 0471731927.

[39] Mark Kness. ColorPy - A Python package for handling physical descriptions of color and light spectra, 2008. URL `http://markkness.net/colorpy/ColorPy.html`.

[40] Noboru Ohta and Alan R. Robertson. *Colorimetry*. John Wiley & Sons, Ltd, Chichester, UK, November 2005. ISBN 9780470094747. doi: 10.1002/0470094745.

[41] Albert Chin. Multilayer reflectors by molecular-beam epitaxy for resonance enhanced absorption in thin high-speed detectors. *Journal of Vacuum Science & Technology B: Microelectronics and Nanometer Structures*, 8(2):339, March 1990.

[42] K-K. Law, R. H. Yan, L. A. Coldren, and J. L. Merz. Self-electro-optic device based on a superlattice asymmetric FabryPerot modulator with an on/off ratio 100:1. *Applied Physics Letters*, 57(13):1345, September 1990.

[43] Jonathan R. Tischler, M. Scott Bradley, and Vladimir Bulovi? Critically coupled resonators in vertical geometry using a planar mirror and a 5 nm thick absorbing film. *Optics Letters*, 31(13):2045, 2006.

[44] Y. D. Chong, Li Ge, Hui Cao, and A. D. Stone. Coherent Perfect Absorbers: Time-Reversed Lasers. *Physical Review Letters*, 105(5):053901, July 2010.

[45] Wenjie Wan, Yidong Chong, Li Ge, Heeso Noh, A Douglas Stone, and Hui Cao. Time-reversed lasing and interferometric control of absorption. *Science (New York, N.Y.)*, 331(6019):889–92, February 2011.

[46] Heeso Noh, Yidong Chong, A. Douglas Stone, and Hui Cao. Perfect coupling of light to surface plasmons by coherent absorption. *Physical Review Letters*, 108 (18):186805, May 2012.

[47] N. Landy, S. Sajuyigbe, J. Mock, D. Smith, and W. Padilla. Perfect Metamaterial Absorber. *Physical Review Letters*, 100(20):207402, May 2008.

[48] Hu Tao, C. Bingham, A. Strikwerda, D. Pilon, D. Shrekenhamer, N. Landy, K. Fan, X. Zhang, W. Padilla, and R. Averitt. Highly flexible wide angle of incidence terahertz metamaterial absorber: Design, fabrication, and characterization. *Physical Review B*, 78(24):241103, December 2008.

[49] Jiaming Hao, Jing Wang, Xianliang Liu, Willie J. Padilla, Lei Zhou, and Min Qiu. High performance optical absorber based on a plasmonic metamaterial. *Applied Physics Letters*, 96(25):251104, June 2010.

[50] Chihhui Wu, Burton Neuner, Gennady Shvets, Jeremy John, Andrew Milder, Byron Zollars, and Steve Savoy. Large-area wide-angle spectrally selective plasmonic absorber. *Physical Review B*, 84(7):075102, August 2011.

[51] Mengkun Liu, Harold Y Hwang, Hu Tao, Andrew C Strikwerda, Kebin Fan, George R Keiser, Aaron J Sternbach, Kevin G West, Salinporn Kittiwatanakul, Jiwei Lu, Stuart A Wolf, Fiorenzo G Omenetto, Xin Zhang, Keith A Nelson, and Richard D Averitt. Terahertz-field-induced insulator-to-metal transition in vanadium dioxide metamaterial. *Nature*, 487(7407):345–8, July 2012.

[52] M M Qazilbash, M Brehm, Byung-Gyu Chae, P-C Ho, G O Andreev, Bong-Jun Kim, Sun Jin Yun, A V Balatsky, M B Maple, F Keilmann, Hyun-Tak Kim, and D N Basov. Mott transition in VO2 revealed by infrared spectroscopy and nano-imaging. *Science (New York, N.Y.)*, 318(5857):1750–3, December 2007.

[53] H. Choi, J. Ahn, J. Jung, T. Noh, and D. Kim. Mid-infrared properties of a VO2 film near the metal-insulator transition. *Physical Review B*, 54(7):4621–4628, August 1996.

[54] Zheng Yang, Changhyun Ko, and Shriram Ramanathan. Oxide Electronics Utilizing Ultrafast Metal-Insulator Transitions. *Annual Review of Materials Research*, 41(1):337–367, August 2011.

[55] W.R. Roach and I. Balberg. Optical induction and detection of fast phase transition in VO2. *Solid State Communications*, 9(9):551–555, 1971.

[56] Dmitry Ruzmetov, Kevin T Zawilski, Sanjaya D Senanayake, Venkatesh Narayanamurti, and Shriram Ramanathan. Infrared reflectance and photoemission spectroscopy studies across the phase transition boundary in thin film vanadium dioxide. *Journal of physics. Condensed matter : an Institute of Physics journal*, 20 (46):465204, November 2008.

[57] T Driscoll, Hyun-Tak Kim, Byung-Gyu Chae, Bong-Jun Kim, Yong-Wook Lee, N Marie Jokerst, S Palit, D R Smith, M Di Ventra, and D N Basov. Memory metamaterials. *Science (New York, N.Y.)*, 325(5947):1518–21, September 2009.

[58] Matthew J Dicken, Koray Aydin, Imogen M Pryce, Luke A Sweatlock, Elizabeth M Boyd, Sameer Walavalkar, James Ma, and Harry A Atwater. Frequency tunable near-infrared metamaterials based on VO2 phase transition. *Optics express*, 17 (20):18330–9, September 2009.

[59] Minah Seo, Jisoo Kyoung, Hyeongryeol Park, Sukmo Koo, Hyun-sun Kim, Hannes Bernien, Bong Jun Kim, Jong Ho Choe, Yeong Hwan Ahn, Hyun-Tak Kim, Namkyoo Park, Q-Han Park, Kwangjun Ahn, and Dai-sik Kim. Active terahertz nanoantennas based on VO2 phase transition. *Nano letters*, 10(6):2064–8, June 2010.

[60] Tomokuni Mitsuishi. On the Phase Transformation of VO 2. *Japanese Journal of Applied Physics*, 6(9):1060–1071, September 1967.

[61] Kazuki Nagashima, Takeshi Yanagida, Hidekazu Tanaka, and Tomoji Kawai. Stress relaxation effect on transport properties of strained vanadium dioxide epitaxial thin films. *Physical Review B*, 74(17):172106, November 2006.

[62] Changhyun Ko and Shriram Ramanathan. Stability of electrical switching properties in vanadium dioxide thin films under multiple thermal cycles across the phase transition boundary. *Journal of Applied Physics*, 104(8):086105, 2008.

[63] N Engheta and RW Ziolkowski. *Metamaterials: physics and engineering explorations*. 2006.

[64] ED Palik. *Handbook of Optical Constants of Solids: Index*. 1998.

[65] Joyeeta Nag and R F Haglund Jr. Synthesis of vanadium dioxide thin films and nanoparticles. *Journal of Physics: Condensed Matter*, 20(26):264016, July 2008.

[66] Herman Bosman, Y. Y. Lau, and R. M. Gilgenbach. Microwave absorption on a thin film. *Applied Physics Letters*, 82(9):1353, March 2003.

[67] Carl Hägglund, S Peter Apell, and Bengt Kasemo. Maximized optical absorption in ultrathin films and its application to plasmon-based two-dimensional photovoltaics. *Nano letters*, 10(8):3135–41, August 2010.

[68] Mingbo Pu, Qin Feng, Min Wang, Chenggang Hu, Cheng Huang, Xiaoliang Ma, Zeyu Zhao, Changtao Wang, and Xiangang Luo. Ultrathin broadband nearly perfect absorber with symmetrical coherent illumination. *Optics express*, 20(3): 2246–54, January 2012.

[69] Frank Niklaus, Christian Vieider, and Henrik Jakobsen. ¡title¿MEMS-based uncooled infrared bolometer arrays: a review¡/title¿. In Jung-Chih Chiao, Xuyuan Chen, Zhaoying Zhou, and Xinxin Li, editors, *Photonics Asia 2007*, pages 68360D–68360D–15. International Society for Optics and Photonics, November 2007. doi: 10.1117/12.755128. URL `http://proceedings.spiedigitallibrary.org/proceeding.aspx?articleid=816159`.

[70] R.S. Scott and G.E. Fredericks. Model for infrared detection by a metal-semiconductor phase transition. *Infrared Physics*, 16(6):619–626, 1976.

[71] M. Gurvitch, S. Luryi, A. Polyakov, and A. Shabalov. Nonhysteretic behavior inside the hysteresis loop of VO[sub 2] and its possible application in infrared imaging. *Journal of Applied Physics*, 106(10):104504, November 2009.

[72] Changhong Chen, Xinjian Yi, Xingrong Zhao, and Bifeng Xiong. Characterizations of VO2-based uncooled microbolometer linear array. *Sensors and Actuators A: Physical*, 90(3):212–214, 2001.

[73] HT Miyazaki and Y Kurokawa. Controlled plasmon resonance in closed metal/insulator/metal nanocavities. *Applied physics letters*, 2006.

[74] Matthias Wuttig and Noboru Yamada. Phase-change materials for rewriteable data storage. *Nature materials*, 6(11):824–32, November 2007.

[75] J. Mink. *Handbook of Vibrational Spectroscopy*. John Wiley & Sons, Ltd, Chichester, UK, June 2006. ISBN 0471988472.

[76] A. Vorobyev, V. Makin, and Chunlei Guo. Brighter Light Sources from Black Metal: Significant Increase in Emission Efficiency of Incandescent Light Sources. *Physical Review Letters*, 102(23):234301, June 2009.

[77] Jeffrey S. Hale, Michael DeVries, Brad Dworak, and John A. Woollam. Visible and infrared optical constants of electrochromic materials for emissivity modulation applications. *Thin Solid Films*, 313:205–209, 1998.

[78] E. B. Franke, C. L. Trimble, M. Schubert, J. A. Woollam, and J. S. Hale. All-solid-state electrochromic reflectance device for emittance modulation in the far-infrared spectral region. *Applied Physics Letters*, 77(7):930, 2000.

[79] M. Benkahoul, M. Chaker, J. Margot, E. Haddad, R. Kruzelecky, B. Wong, W. Jamroz, and P. Poinas. Thermochromic VO2 film deposited on Al with tunable thermal emissivity for space applications. *Solar Energy Materials and Solar Cells*, 95(12):3504–3508, 2011.

[80] John K. Coulter, Christopher F. Klein, and James C. Jafolla. ¡title¿Two optical methods for vehicle tagging¡/title¿. In Edward M. Carapezza, editor, *AeroSense 2002*, pages 354–365. International Society for Optics and Photonics, August 2002. doi: 10.1117/12.479327. URL `http://proceedings.spiedigitallibrary.org/proceeding.aspx?articleid=884706`.

[81] Donald L. Chubb, AnnaMaria T. Pal, Martin O. Patton, and Phillip P. Jenkins. Rare earth doped high temperature ceramic selective emitters. *Journal of the European Ceramic Society*, 19(13):2551–2562, 1999.

[82] Jean-Jacques Greffet, Rémi Carminati, Karl Joulain, Jean-Philippe Mulet, Stéphane Mainguy, and Yong Chen. Coherent emission of light by thermal sources. *Nature*, 416(6876):61–4, March 2002.

[83] M. U. Pralle, N. Moelders, M. P. McNeal, I. Puscasu, A. C. Greenwald, J. T. Daly, E. A. Johnson, T. George, D. S. Choi, I. El-Kady, and R. Biswas. Photonic crystal enhanced narrow-band infrared emitters. *Applied Physics Letters*, 81(25): 4685, 2002.

[84] N J Harrick and A F Turner. A thin film optical cavity to induce absorption or thermal emission. *Applied optics*, 9(9):2111–4, September 1970.

[85] Ivan Celanovic, David Perreault, and John Kassakian. Resonant-cavity enhanced thermal emission. *Physical Review B*, 72(7):075127, August 2005.

[86] Jon A. Schuller, Thomas Taubner, and Mark L. Brongersma. Optical antenna thermal emitters. *Nature Photonics*, 3(11):658–661, October 2009.

[87] Xianliang Liu, Talmage Tyler, Tatiana Starr, Anthony F. Starr, Nan Marie Jokerst, and Willie J. Padilla. Taming the Blackbody with Infrared Metamaterials as Selective Thermal Emitters. *Physical Review Letters*, 107(4):045901, July 2011.

[88] F Guinneton, L Sauques, J.C Valmalette, F Cros, and J.R Gavarri. Comparative study between nanocrystalline powder and thin film of vanadium dioxide VO2: electrical and infrared properties. *Journal of Physics and Chemistry of Solids*, 62 (7):1229–1238, 2001.

[89] Frédéric Guinneton, Laurent Sauques, Jean-Christophe Valmalette, Frédéric Cros, and Jean-Raymond Gavarri. Optimized infrared switching properties in thermochromic vanadium dioxide thin films: role of deposition process and microstructure. *Thin Solid Films*, 446(2):287–295, 2004.

[90] R. Li Voti, M. C. Larciprete, G. Leahu, C. Sibilia, and M. Bertolotti. Optimization of thermochromic VO2 based structures with tunable thermal emissivity. *Journal of Applied Physics*, 112(3):034305, 2012.

[91] John Topping, Alexander. STRUCTURE WITH VARIABLE EMITTANCE, October 2002. URL `http://patentscope.wipo.int/search/en/WO2002082172`.

[92] R.J. Lauf, C. Hamby, M. A. Akerman, and A. W. Trivelpiece. Blackbody material, 1994.

[93] N Gao, H Sun, and D Ewing. Heat transfer to impinging round jets with triangular tabs. *International Journal of Heat and Mass Transfer*, 46(14):2557–2569, 2003.

[94] M. H. Friedman. Patent US5734495 - Passive control of emissivity, color and camouflage, 1998. URL `http://www.google.com/patents?hl=en&lr=&vid=USPAT5734495&id=8Y8kAAAAEBAJ&oi=fnd&dq=Passive+control+of+emissivity,+color+and+camouflage&printsec=abstract#v=onepage&q=Passivecontrolofemissivity,colorandcamouflage&f=false`.

[95] Sergey Shilov. Emission measurements (unpublished). 2012.

[96] J. Narayan and V. M. Bhosle. Phase transition and critical issues in structure-property correlations of vanadium oxide. *Journal of Applied Physics*, 100(10): 103524, 2006.

[97] Y Muraoka, Y Ueda, and Z Hiroi. Large modification of the metalinsulator transition temperature in strained VO2 films grown on TiO2 substrates. *Journal of Physics and Chemistry of Solids*, 63(6):965–967, 2002.

[98] Hisao Futaki and Minoru Aoki. Effects of Various Doping Elements on the Transition Temperature of Vanadium Oxide Semiconductors. *Japanese Journal of Applied Physics*, 8(8):1008–1013, August 1969.

[99] Masami Nishikawa, Tomohiko Nakajima, Toshiya Kumagai, Takeshi Okutani, and Tetsuo Tsuchiya. Adjustment of thermal hysteresis in epitaxial VO2 films by doping metal ions. *Journal of the Ceramic Society of Japan*, 119(1391):577–580, 2011.

[100] Stephanie Law, Viktor Podolskiy, and Daniel Wasserman. Towards nano-scale photonics with micro-scale photons: the opportunities and challenges of mid-infrared plasmonics. *Nanophotonics*, 2(2):103–130, April 2013.

[101] Mikhail A Kats, Romain Blanchard, Patrice Genevet, Zheng Yang, M Mumtaz Qazilbash, D N Basov, Shriram Ramanathan, and Federico Capasso. Thermal tuning of mid-infrared plasmonic antenna arrays using a phase change material. *Optics Letters*, 38(3):368–370, 2013.

[102] V. G. Golubev, V. Yu. Davydov, N. F. Kartenko, D. A. Kurdyukov, A. V. Medvedev, A. B. Pevtsov, A. V. Scherbakov, and E. B. Shadrin. Phase transition-governed opalVO2 photonic crystal. *Applied Physics Letters*, 79(14):2127, 2001.

[103] Wikipedia. Resonance, 2013. URL `http://en.wikipedia.org/wiki/Resonance`.

[104] Amnon Yariv and Pochi Yeh. *Photonics: Optical Electronics in Modern Communications (The Oxford Series in Electrical and Computer Engineering)*. Oxford University Press, USA, 2006. ISBN 0195179463.

[105] AE Siegman. Lasers University Science Books. *Mill Valley, CA*, 1986.

[106] Takeshi Watanabe, Masaaki Fujii, Yoshi Watanabe, Nobuhito Toyama, and Yoshinori Iketaki. Generation of a doughnut-shaped beam using a spiral phase plate. *Review of Scientific Instruments*, 75(12):5131, 2004.

[107] JH McLeod. The axicon: a new type of optical element. *JOSA*, 1954.

[108] D Casasent. Spatial light modulators. *Proceedings of the IEEE*, 1977.

[109] JW Goodman. *Introduction to Fourier optics*. 2005.

[110] JB Pendry, D Schurig, and DR Smith. Controlling electromagnetic fields. *Science*, 2006.

[111] U Leonhardt. Optical conformal mapping. *Science*, 2006.

[112] W Cai and VM Šalaev. *Optical metamaterials: fundamentals and applications*. 2010.

[113] Nanfang Yu, Patrice Genevet, Mikhail A Kats, Francesco Aieta, Jean-Philippe Tetienne, Federico Capasso, and Zeno Gaburro. Light Propagation with Phase Discontinuities: Generalized Laws of Reflection and Refraction. *Science*, 334(6054): 333–337, 2011.

[114] Mikhail A Kats, Nanfang Yu, Patrice Genevet, Zeno Gaburro, and Federico Capasso. Effect of radiation damping on the spectral response of plasmonic components. *Optics Express*, 19(22):21748–53, 2011.

[115] Mikhail A Kats, Patrice Genevet, Guillaume Aoust, Nanfang Yu, Romain Blanchard, Francesco Aieta, Zeno Gaburro, and Federico Capasso. Giant birefringence in optical antenna arrays with widely tailorable optical anisotropy. *PNAS*, 109 (31):12364–8, 2012.

[116] Patrice Genevet, Nanfang Yu, Francesco Aieta, Jiao Lin, Mikhail A Kats, Romain Blanchard, Marlan O Scully, Zeno Gaburro, and Federico Capasso. Ultra-thin plasmonic optical vortex plate based on phase discontinuities. *Applied Physics Letters*, 100(1):013101, 2012.

[117] Francesco Aieta, Patrice Genevet, Mikhail A Kats, Nanfang Yu, Romain Blanchard, Zeno Gaburro, and Federico Capasso. Aberration-Free Ultrathin Flat Lenses and Axicons at Telecom Wavelengths Based on Plasmonic Metasurfaces. *Nano Letters*, 2012.

[118] Francesco Aieta, Patrice Genevet, Nanfang Yu, Mikhail A Kats, Zeno Gaburro, and Federico Capasso. Out-of-plane reflection and refraction of light by anisotropic optical antenna metasurfaces with phase discontinuities. *Nano Letters*, 12(3):1702–6, 2012.

[119] Romain Blanchard, Guillaume Aoust, Patrice Genevet, Mikhail A Kats, Zeno Gaburro, and Federico Capasso. Modeling nanoscale V-shaped antennas for the design of optical phased arrays. *Physical Review B*, 85, 2012.

[120] David Fattal, Jingjing Li, Zhen Peng, Marco Fiorentino, and RG Raymond G. Beausoleil. Flat dielectric grating reflectors with focusing abilities. *Nature Photonics*, 4(7):466–470, May 2010.

[121] JA Fan, C Wu, K Bao, J Bao, and R Bardhan. Self-assembled plasmonic nanoparticle clusters. *science*, 2010.

[122] Lukas Novotny and Niek van Hulst. Antennas for light. *Nature Photonics*, 5(2): 83–90, February 2011.

[123] X Hu, CT Chan, KM Ho, and J Zi. Negative effective gravity in water waves by periodic resonator arrays. *Physical review letters*, 2011.

[124] Z Liu, X Zhang, Y Mao, YY Zhu, and Z Yang. Locally resonant sonic materials. *Science*, 2000.

[125] Robert D. Grober, Robert J. Schoelkopf, and Daniel E. Prober. Optical antenna: Towards a unity efficiency near-field optical probe. *Applied Physics Letters*, 70 (11):1354, 1997.

[126] Qiaobing Xu, Jiming Bao, Robert M Rioux, Raquel Perez-Castillejos, Federico Capasso, and George M Whitesides. Fabrication of large-area patterned nanostructures for optical applications by nanoskiving. *Nano Letters*, 7:2800–2805, 2007.

[127] Maxim Sukharev, Jiha Sung, Kenneth Spears, and Tamar Seideman. Optical properties of metal nanoparticles with no center of inversion symmetry: Observation of volume plasmons. *Physical Review B*, 76(18):184302, November 2007.

[128] P. Biagioni, J. Huang, L. Duò, M. Finazzi, and B. Hecht. Cross Resonant Optical Antenna. *Physical Review Letters*, 102(25):256801, June 2009.

[129] J Ginn, D Shelton, P Krenz, B Lail, and G Boreman. Polarized infrared emission using frequency selective surfaces. 2010.

[130] K Kneipp, Y Wang, H Kneipp, and LT Perelman. Single molecule detection using surface-enhanced Raman scattering (SERS). *Physical review ...*, 1997.

[131] BK Canfield, H Husu, and J Laukkanen. Local field asymmetry drives second-harmonic generation in noncentrosymmetric nanodimers. *Nano ...*, 2007.

[132] Patrice Genevet, Jean-Philippe Tetienne, Evangelos Gatzogiannis, Romain Blanchard, Mikhail A Kats, Marlan O Scully, and Federico Capasso. Large Enhancement of Nonlinear Optical Phenomena by Plasmonic Nanocavity Gratings. *Nano Letters*, 10(12):4880–4883, 2010.

[133] Palash Bharadwaj, Bradley Deutsch, and Lukas Novotny. Optical Antennas. *Advances in Optics and Photonics*, 1:438, 2009.

[134] Matthew N.O. Sadiku. *Numerical Techniques in Electromagnetics, Second Edition (Google eBook)*. CRC Press, 2010. ISBN 1420058274.

[135] JD Jackson and RF Fox. Classical electrodynamics. *American Journal of Physics*, 1999.

[136] DJ Griffiths and Reed College. *Introduction to electrodynamics*. 1999.

[137] RWP King. The theory of linear antennas. 1956.

[138] SA Maier. *Plasmonics: fundamentals and applications*. 2007.

[139] J Zuloaga and P Nordlander. On the energy shift between near-field and far-field peak intensities in localized plasmon systems. *Nano letters*, 2011.

[140] Shuang Zhang, Dentcho A. DA Genov, Yuan Wang, Ming Liu, and Xiang Zhang. Plasmon-Induced Transparency in Metamaterials. *Physical Review Letters*, 101 (4):047401, July 2008.

[141] N Liu, L Langguth, T Weiss, and J Kästel. Plasmonic analogue of electromagnetically induced transparency at the Drude damping limit. *Nature materials*, 2009.

[142] W Heitler. *The quantum theory of radiation*. 1954.

[143] KL Kelly and E Coronado. The optical properties of metal nanoparticles: the influence of size, shape, and dielectric environment. *The Journal of Physical ...*, 2003.

[144] NK Grady, NJ Halas, and P Nordlander. Influence of dielectric function properties on the optical response of plasmon resonant metallic nanoparticles. *Chemical Physics Letters*, 2004.

[145] S Bruzzone and M Malvaldi. Light scattering by gold nanoparticles: role of simple dielectric models. *The Journal of Physical ...*, 2004.

[146] A.-S. Grimault, A. Vial, and M. Lamy de la Chapelle. Modeling of regular gold nanostructures arrays for SERS applications using a 3D FDTD method. *Applied Physics B*, 84(1-2):111–115, April 2006.

[147] GW Bryant, FJ García de Abajo, and J Aizpurua. Mapping the plasmon resonances of metallic nanoantennas. *Nano letters*, 2008.

[148] BM Ross and LP Lee. Comparison of near-and far-field measures for plasmon resonance of metallic nanoparticles. *Optics letters*, 2009.

[149] WL Stutzman and GA Thiele. *Antenna theory and design*. 1981. URL `http://scholar.google.com/scholar?q=Antenna+Theory+and+Design+thiele&btnG=&hl=en&as_sdt=0,22#1`.

[150] CA Balanis. *Antenna theory: analysis and design*. 2012.

[151] SJ Orfanidis. *Electromagnetic waves and antennas*. 2002.

[152] N Engheta, CH Papas, and C Elachi. Radiation patterns of interfacial dipole antennas. *Radio Science*, 1982.

[153] Ertugrul Cubukcu and Federico Capasso. Optical nanorod antennas as dispersive one-dimensional FabryPerot resonators for surface plasmons. *Applied Physics Letters*, 95(20):201101, November 2009.

[154] JS Huang, J Kern, P Geisler, and P Weinmann. Mode imaging and selection in strongly coupled nanoantennas. *Nano ...*, 2010.

[155] SD Brorson and HA Haus. Diffraction gratings and geometrical optics. *JOSA B*, 1988.

[156] RP Feynman and AR Hibbs. *Quantum mechanics and path integrals: Emended edition*. 2012.

[157] D.M. Pozar, S.D. Targonski, and H.D. Syrigos. Design of millimeter wave microstrip reflectarrays. *IEEE Transactions on Antennas and Propagation*, 45(2): 287–296, 1997.

[158] J.A. Encinar. Design of two-layer printed reflectarrays using patches of variable size. *IEEE Transactions on Antennas and Propagation*, 49(10):1403–1410, 2001.

[159] Colan G M Ryan, Mohammad Reza Chaharmir, J Shaker, Joey R Bray, Yahia M M Antar, and A Ittipiboon. A Wideband Transmitarray Using Dual-Resonant Double Square Rings. *IEEE Transactions on Antennas and Propagation*, 58(5): 1486–1493, May 2010.

[160] Pablo Padilla, Alfonso Muñoz Acevedo, Manuel Sierra-Castañer, and Manuel Sierra-Perez. Electronically Reconfigurable Transmitarray at Ku Band for Microwave Applications. *IEEE Transactions on Antennas and Propagation*, 58(8): 2571–2579, August 2010.

[161] VG Veselago. THE ELECTRODYNAMICS OF SUBSTANCES WITH SIMULTANEOUSLY NEGATIVE VALUES OF IMG align= ABSMIDDLE alt= eps/IMG AND μ. *Physics-Uspekhi*, 1968.

[162] JB Pendry. Negative refraction makes a perfect lens. *Physical review letters*, 2000.

[163] RA Shelby, DR Smith, and S Schultz. Experimental verification of a negative index of refraction. *Science*, 2001.

[164] CG Parazzoli, RB Greegor, and K Li. Experimental verification and simulation of negative index of refraction using Snell's law. *Physical Review Letters*, 2003.

[165] AA Houck, JB Brock, and IL Chuang. Experimental observations of a left-handed material that obeys Snell's law. *Physical Review Letters*, 2003.

[166] Stephen M. Barnett. Resolution of the Abraham-Minkowski Dilemma. *Physical Review Letters*, 104(7):070401, February 2010.

[167] PP Ewald. Introduction to the dynamical theory of X-ray diffraction. *... Section A: Crystal Physics, Diffraction, Theoretical and ...*, 1969.

[168] H Kikuta, Y Ohira, and K Iwata. Achromatic quarter-wave plates using the dispersion of form birefringence. *Applied optics*, 1997.

[169] J Sung and M Sukharev. Nanoparticle spectroscopy: Birefringence in two-dimensional arrays of L-shaped silver nanoparticles. *The Journal of ...*, 2008.

[170] L Feng, A Mizrahi, S Zamek, and Z Liu. Metamaterials for enhanced polarization conversion in plasmonic excitation. *ACS ...*, 2011.

[171] MR Shcherbakov, MI Dobynde, and TV Dolgova. Full Poincaré sphere coverage with plasmonic nanoslit metamaterials at Fano resonance. *Physical Review B*, 2010.

[172] JF Nye and MV Berry. Dislocations in wave trains. *... of the Royal Society of London. ...*, 1974.

[173] Miles Padgett, Johannes Courtial, and Les Allen. Light's Orbital Angular Momentum. *Physics Today*, 57(5):35, May 2004.

[174] L. Allen, MW Beijersbergen, R. Spreeuw, and J. Woerdman. Orbital angular momentum of light and the transformation of Laguerre-Gaussian laser modes. *Physical Review A*, 45(11):8185–8189, June 1992.

[175] MW Beijersbergen and RPC Coerwinkel. Helical-wavefront laser beams produced with a spiral phaseplate. *Optics ...*, 1994.

[176] N. R. NR Heckenberg, R. McDuff, C. P. CP Smith, and A. G. AG White. Generation of optical phase singularities by computer-generated holograms. *Opt. Lett*, 17(3):221, February 1992.

[177] VY Bazhenov, MV Vasnetsov, and MS Soskin. Laser beams with screw dislocations in their wavefronts. *Jetp Lett*, 1990.

[178] A.G. AG White, CP C.P. Smith, N.R. Heckenberg, H. Rubinsztein-Dunlop, R. McDuff, C.O. Weiss, and Chr. Tamm. Interferometric measurements of phase singularities in the output of a visible laser. *Journal of Modern ...*, 38(12):2531–2541, December 1991.

[179] Stefan W Hell. Far-field optical nanoscopy. *Science (New York, N.Y.)*, 316(5828): 1153–8, May 2007.

[180] H He and MEJ Friese. Direct observation of transfer of angular momentum to absorptive particles from a laser beam with a phase singularity. *Physical Review Letters*, 1995.

[181] Miles Padgett and Richard Bowman. Tweezers with a twist. *Nature Photonics*, 5 (6):343–348, June 2011.

[182] Jonathan Leach, Miles MJ Padgett, Stephen Barnett, Sonja Franke-Arnold, and Johannes Courtial. Measuring the Orbital Angular Momentum of a Single Photon. *Physical Review Letters*, 88(25):257901, June 2002.

[183] G Gibson, J Courtial, and MJ Padgett. Free-space information transfer using light beams carrying orbital angular momentum. *Opt. . . .*, 2004.

[184] A. Papakostas, A. Potts, D. Bagnall, S. Prosvirnin, H. Coles, and N. Zheludev. Optical Manifestations of Planar Chirality. *Physical Review Letters*, 90(10):107404, March 2003.

[185] S. Prosvirnin and N. Zheludev. Polarization effects in the diffraction of light by a planar chiral structure. *Physical Review E*, 71(3):037603, March 2005.

[186] E. Plum, J. Zhou, J. Dong, V. Fedotov, T. Koschny, C. Soukoulis, and N. Zheludev. Metamaterial with negative index due to chirality. *Physical Review B*, 79(3): 035407, January 2009.

[187] Shuang Zhang, Yong-Shik Park, Jensen Li, Xinchao Lu, Weili Zhang, and Xiang Zhang. Negative Refractive Index in Chiral Metamaterials. *Physical Review Letters*, 102(2):023901, January 2009.

[188] Xiang Xiong, Wei-Hua Sun, Yong-Jun Bao, Mu Wang, Ru-Wen Peng, Cheng Sun, Xiang Lu, Jun Shao, Zhi-Feng Li, and Nai-Ben Ming. Construction of a chiral metamaterial with a U-shaped resonator assembly. *Physical Review B*, 81(7): 075119, February 2010.

[189] M Decker, R Zhao, C M Soukoulis, S Linden, and M Wegener. Twisted split-ring-resonator photonic metamaterial with huge optical activity. *Optics letters*, 35(10): 1593–5, May 2010.

[190] Justyna K Gansel, Michael Thiel, Michael S Rill, Manuel Decker, Klaus Bade, Volker Saile, Georg von Freymann, Stefan Linden, and Martin Wegener. Gold helix photonic metamaterial as broadband circular polarizer. *Science (New York, N.Y.)*, 325(5947):1513–5, September 2009.

[191] Y Zhao, M A Belkin, and A Alù. Twisted optical metamaterials for planarized ultrathin broadband circular polarizers. *Nature communications*, 3:870, January 2012.

[192] Ming Kang, Tianhua Feng, Hui-Tian Wang, and Jensen Li. Wave front engineering from an array of thin aperture antennas. *Optics express*, 20(14):15882–90, July 2012.

[193] R. Gordon, A. Brolo, A. McKinnon, A. Rajora, B. Leathem, and K. Kavanagh. Strong Polarization in the Optical Transmission through Elliptical Nanohole Arrays. *Physical Review Letters*, 92(3):037401, January 2004.

[194] Anders Pors, Michael G Nielsen, Giuseppe Della Valle, Morten Willatzen, Ole Albrektsen, and Sergey I Bozhevolnyi. Plasmonic metamaterial wave retarders in reflection by orthogonally oriented detuned electrical dipoles. *Optics letters*, 36 (9):1626–8, May 2011.

[195] Eng Huat Khoo, Er Ping Li, and Kenneth B Crozier. Plasmonic wave plate based on subwavelength nanoslits. *Optics letters*, 36(13):2498–500, July 2011.

[196] Yang Zhao and Andrea Alù. Manipulating light polarization with ultrathin plasmonic metasurfaces. *Physical Review B*, 84(20):205428, November 2011.

[197] L. Young, L. Robinson, and C. Hacking. Meander-line polarizer. *IEEE Transactions on Antennas and Propagation*, 21(3):376–378, May 1973.

[198] Samuel L. Wadsworth, Paul G. Clem, Eric D. Branson, and Glenn D. Boreman. Broadband circularly-polarized infrared emission from multilayer metamaterials. *Optical Materials Express*, 1(3):466, June 2011.

[199] W. Heller. Light scattering of spheroids. III. Depolarization of the scattered light. *The Journal of Chemical Physics*, 61(9):3619, November 1974.

[200] Nikolai G Khlebtsov, Andrei G Melnikov, Vladimir A Bogatyrev, Lev A Dykman, Anna V Alekseeva, Lyubov A Trachuk, and Boris N Khlebtsov. Can the light scattering depolarization ratio of small particles be greater than 1/3? *The journal of physical chemistry. B*, 109(28):13578–84, July 2005.

[201] Zygmunt Gryczynski, Joanna Lukomska, Joseph R. Lakowicz, Evgenia G. Matveeva, and Ignacy Gryczynski. Depolarized light scattering from silver nanoparticles. *Chemical Physics Letters*, 421(1):189–192, 2006.

[202] Fu Min Huang, Tsung Sheng Kao, Vassili A Fedotov, Yifang Chen, and Nikolay I Zheludev. Nanohole array as a lens. *Nano letters*, 8(8):2469–72, August 2008.

[203] Fu Min Huang and Nikolay I Zheludev. Super-resolution without evanescent waves. *Nano letters*, 9(3):1249–54, March 2009.

[204] Edward T F Rogers, Jari Lindberg, Tapashree Roy, Salvatore Savo, John E Chad, Mark R Dennis, and Nikolay I Zheludev. A super-oscillatory lens optical microscope for subwavelength imaging. *Nature materials*, 11(5):432–5, May 2012.

[205] Lieven Verslegers, Peter B Catrysse, Zongfu Yu, Justin S White, Edward S Barnard, Mark L Brongersma, and Shanhui Fan. Planar lenses based on nanoscale slit arrays in a metallic film. *Nano letters*, 9(1):235–8, January 2009.

[206] Babak Memarzadeh and Hossein Mosallaei. Array of planar plasmonic scatterers functioning as light concentrator. *Optics letters*, 36(13):2569–71, July 2011.

[207] Nicholas Fang, Hyesog Lee, Cheng Sun, and Xiang Zhang. Sub-diffraction-limited optical imaging with a silver superlens. *Science (New York, N.Y.)*, 308(5721): 534–7, April 2005.

[208] Alessandro Salandrino and Nader Engheta. Far-field subdiffraction optical microscopy using metamaterial crystals: Theory and simulations. *Physical Review B*, 74(7):075103, August 2006.

[209] Zhaowei Liu, Hyesog Lee, Yi Xiong, Cheng Sun, and Xiang Zhang. Far-field optical hyperlens magnifying sub-diffraction-limited objects. *Science (New York, N.Y.)*, 315(5819):1686, March 2007.

[210] I Manek, Yu.B Ovchinnikov, and R Grimm. Generation of a hollow laser beam for atom trapping using an axicon. *Optics Communications*, 147(1):67–70, 1998.

[211] V. Jarutis, R. Paškauskas, and A. Stabinis. Focusing of LaguerreGaussian beams by axicon. 2000. URL `http://www.sciencedirect.com/science/article/pii/S0030401800009615`.

[212] T. Driscoll, S. Palit, M. M. Qazilbash, M. Brehm, F. Keilmann, Byung-Gyu Chae, Sun-Jin Yun, Hyun-Tak Kim, S. Y. Cho, N. Marie Jokerst, D. R. Smith, and D. N. Basov. Dynamic tuning of an infrared hybrid-metamaterial resonance using vanadium dioxide. *Applied Physics Letters*, 93(2):024101, 2008.

[213] M. D. Goldflam, T. Driscoll, B. Chapler, O. Khatib, N. Marie Jokerst, S. Palit, D. R. Smith, Bong-Jun Kim, Giwan Seo, Hyun-Tak Kim, M. Di Ventra, and D. N. Basov. Reconfigurable gradient index using VO2 memory metamaterials. *Applied Physics Letters*, 99(4):044103, July 2011.

[214] J Y Suh, E U Donev, D W Ferrara, K A Tetz, L C Feldman, and R F Haglund Jr. Modulation of the gold particleplasmon resonance by the metalsemiconductor transition of vanadium dioxide. *Journal of Optics A: Pure and Applied Optics*, 10 (5):055202, May 2008.

[215] Dang Yuan Lei, Kannatassen Appavoo, Yannick Sonnefraud, Richard F Haglund, and Stefan A Maier. Single-particle plasmon resonance spectroscopy of phase transition in vanadium dioxide. *Optics letters*, 35(23):3988–90, December 2010.

[216] D. W. Ferrara, E. R. MacQuarrie, J. Nag, A. B. Kaye, and R. F. Haglund. Plasmon-enhanced low-intensity laser switching of gold::vanadium dioxide nanocomposites. *Applied Physics Letters*, 98(24):241112, June 2011.

[217] Ben A. Munk. *Frequency Selective Surfaces: Theory and Design.* Wiley-Interscience, 2000. ISBN 0471370479.

[218] Irina Puscasu, David Spencer, and Glenn D. Boreman. Refractive-index and element-spacing effects on the spectral behavior of infrared frequency-selective surfaces. *Applied Optics*, 39(10):1570, April 2000.

[219] Yu Yao, Mikhail A Kats, Patrice Genevet, Nanfang Yu, Yi Song, Jing Kong, and Federico Capasso. Broad electrical tuning of graphene-loaded plasmonic antennas. *Nano letters*, 13(3):1257–64, March 2013.

[220] K S Novoselov, A K Geim, S V Morozov, D Jiang, M I Katsnelson, I V Grigorieva, S V Dubonos, and A A Firsov. Two-dimensional gas of massless Dirac fermions in graphene. *Nature*, 438(7065):197–200, November 2005.

[221] Z Fei, A S Rodin, G O Andreev, W Bao, A S McLeod, M Wagner, L M Zhang, Z Zhao, M Thiemens, G Dominguez, M M Fogler, A H Castro Neto, C N Lau, F Keilmann, and D N Basov. Gate-tuning of graphene plasmons revealed by infrared nano-imaging. *Nature*, 487(7405):82–5, July 2012.

[222] Long Ju, Baisong Geng, Jason Horng, Caglar Girit, Michael Martin, Zhao Hao, Hans A Bechtel, Xiaogan Liang, Alex Zettl, Y Ron Shen, and Feng Wang. Graphene plasmonics for tunable terahertz metamaterials. *Nature nanotechnology*, 6(10):630–4, October 2011.

[223] L. Falkovsky and S. Pershoguba. Optical far-infrared properties of a graphene monolayer and multilayer. *Physical Review B*, 76(15):153410, October 2007.

[224] P Mühlschlegel, H-J Eisler, O J F Martin, B Hecht, and D W Pohl. Resonant optical antennas. *Science (New York, N.Y.)*, 308(5728):1607–9, June 2005.